PFC/RR-82-24

DOE/ET-51013-53
UC20

HESTER

A Hot Electron Superconducting Tokamak Experimental Reactor at M.I.T.

by
Joel H. Schultz and D. Bruce Montgomery
Massachusetts Institute of Technology
Plasma Fusion Center
Cambridge, MA 02139

April 1983

HESTER

A Hot Electron Superconducting Tokamak Experimental Reactor at M.I.T.

by Joel H. Schultz and D. Bruce Montgomery

M.I.T. Plasma Fusion Center

Plasma Fusion Center Research Report PFC-RR-82-24

April 4, 1983

Contributors

E.S. Bobrov
P. Brindza
L. Bromberg
N. Diatchenko
P. Gierszewski
M.O. Hoenig
T. Morizio
D. Sliski
R.J. Thome

HESTER

A Hot Electron Superconducting Tokamak Experimental Reactor at M.I.T.

by Joel H. Schultz and D. Bruce Montgomery
M.I.T. Plasma Fusion Center

Plasma Fusion Center Research Report PFC-RR/82-24
April 4, 1983

Supported by U.S. D.O.E. Contract DOE/ET-51013-53

Table of Contents

Foreword

HESTER is the result of an experiment planning exercise in 1982 by the authors, and as such is the forerunner of the next-step tokamak experiment being proposed by the M.I.T. Plasma Fusion Center in 1983. However, while strong similarities are readily evident between the machine and mission of HESTER and the proposed tokamak experiment, the two machines are not identical. At this writing, the final parameters of the proposed machine have not been selected and at least two options are being studied. The present document serves two purposes, as a final report on the abovementioned experiment design study and as a background to the possible missions and constraints for a machine of the HESTER class at M.I.T.

Probably the most important difference between HESTER and the machine being proposed at M.I.T. is that HESTER was designed to be long pulse or high power, but not both simultaneously. The motivation was to optimize the use of existing equipment and minimize the machine cost, while retaining a number of other primary missions described in the introduction. However, program priorities dictate the early introduction of a machine which can also serve as an engineering test facility for screening the internal vacuum vessel components (limiters, rails, vacuum vessel, waveguides and antennas) and rf components, which are believed to be the limiting components of reactor reliability, until successful experimental screening has been accomplished. A small, superconducting machine, heated by high power density rf heating, can achieve high wall loadings and energy densities with a small wall area that limits wasteful recirculating power and system operating costs. Since the original design thought for HESTER was inadequate for this enhanced mission, detailed discussion of the first wall and limiter will be discussed in a separate design document.

A key motivation for the HESTER concept was the ability to effectively utilize the resources at M.I.T. Although the cost advantages for a machine using large equipment credits and low additional power requirements were a major factor in the machine's motivation, cost will be discussed in a separate document, as is typically done.

Prologue

The Physics Mission of HESTER

She was offered to the world as the living hieroglyphic, in which was revealed the secret so darkly hidden - all written in this symbol, all plainly manifest, had there been a prophet or magician skilled to read the character of flame.!

- N. Hawthorne, *The Scarlet Letter*

HESTER

A Hot Electron Superconducting Tokamak Experimental Reactor at M.I.T.

1. Introduction

HESTER is an experimental tokamak, designed to resolve many of the central questions in the tokamak development program in the 1980's. It combines several unique features with new perspectives on the other major tokamak experiments scheduled for the next decade. The overall objectives of HESTER , in rough order of their presently perceived importance, are the achievement of reactor-like wall-loadings and plasma parameters for long pulse periods, determination of a good, reactor-relevant method of steady-state or very long pulse tokamak current drive, duplication of the planned very high temperature neutral injection experiments using only radio frequency heating, a demonstration of true steady-state tokamak operation, integration of a high-performance superconducting magnet system into a tokamak experiment, determination of the best methods of long term impurity control, and studies of transport and pressure limits in high field, high aspect ratio tokamak plasmas. These objectives are described below.

1.1 High Q Current Drive

HESTER has the ability to determine the best of several methods of steady-state tokamak current drive by testing the efficiencies of attractive candidates at high density, low safety factor and at both low and high electron temperatures. Current drive experiments have been planned for lower hybrid, transit time magnetic pumping and compressional Alfven waves, considered to be among the three most promising technologies for reactor applications. Because of its combined superconducting magnets and low plasma cross-section, HESTER can test current drive theories at full performance and high temperature with much less power than other major tokamak experiments. Because of the need for high electron temperatures and correspondingly high magnetic diffusion times in order to evaluate adequately most current drive candidates, a very long pulse machine without magnet derating is required for definitive tests.

1.2 Ion Cyclotron Resonance Frequency Heating

ICRF sources currently in place at M.I.T. should be adequate to supply 12 MW of short pulse power and 9 MW at up to 10 s. Since high field allows increasing plasma current and confinement, without increasing the total number of particles, presently used scaling laws imply that the HESTER plasma might achieve central ion temperatures of 20 keV at low density and close to 10 keV at electron densities of 10^{20}, thus providing early confirmation that ICRF can be used in tokamak reactors at thermonuclear temperatures and pressures.

1.3 Steady-state tokamak operation

The demonstration of true steady-state operation would remove the most serious reservation about the tokamak as a reactor concept. This can be done without straining the limited steady-state power available at M.I.T. by the use of superconducting magnets, requiring under 1 MW of recirculating power, and current drive of a low cross-section, moderate density plasma.

1.3.a Quasi-steady-state tokamak operation

A possibly desirable mode of operation for commercial tokamaks is that of quasi-steady-state operation. In this mode, a small dc electric field is combined with an external current drive mechanism. For example, if the electric field were sufficiently small that the plasma could be run for several hours before resetting the ohmic transformers and if the addition of a small accelerating field to the tail electrons allowed one to halve the necessary wave power, the overall economics of a fusion reactor might be significantly enhanced.

HESTER benefits from having superconducting magnets which allow long pulses at full performance, a high aspect ratio plasma which limits the necessary auxiliary current drive power, and a high aspect ratio solenoid bore which allows a high flux ohmic transformer at low field. The present HESTER ohmic transformer design has a capability of 35 V-s , allowing ample time for magnetic diffusion and tail-bulk equilibria to be reached in an enhanced current drive experiment. Because of the very high ratio of poloidal to toroidal flux, HESTER is the only planned tokamak with a flat-top time several times larger than the classical magnetic diffusion time with full plasma current.

1.4 High Energy Flux to First Wall Components

First wall components, including limiters, rails, vacuum vessels, waveguides and antennas may be the most life-limited components in fusion reactors. Current analysis techniques are inadequate to predict the lifetime of these components. A long-pulse machine with a high wall-launching power density can simulate the loading conditions of a fusion reactor. For example, for a proposed heating source of 9 MW of ICRF and 7 MW of LH, involving no entirely new rf systems at M.I.T., the average thermal wall loading would be 500 kW/m^2, corresponding to neutron wall loading of 2 MW/m^2. Hopefully, this rf power will be primarily put to happier uses than destroying first wall components, but there is adequate power and energy density to rapidly screen most of the first wall component concepts that have been proposed for fusion reactors.

1.5 Superconducting Magnet System

The superconducting magnet system of HESTER has many attractive features and solves several problems. It demonstrates the ability of tokamaks to incorporate superconducting magnets in an integrated system. Unlike Tore Supra, all coils in the HESTER system are superconducting. The superconducting magnet system also permits a major new experiment to be built at M.I.T. without the requirement for new pulsed energy supplies. It incorporates the advanced design feature of energy margin design, first proposed at M.I.T. and demonstrated at Oak Ridge, which permits conservative design against disruption. It incorporates circular magnets, the least expensive shape, demonstrating along with Tore Supra that superconducting toroidal magnet systems can be built to any shape desired.

1.6 Long Term Impurity Control

Uncontrolled impurity build-up is not expected in a non-fusile tokamak plasma. However, the steady-state levels of wall impurites, after the very long time constants associated with plasma-wall interactions, are still not predictable. HESTER allows high performance discharges to be run longer than the characteristic times of magnetic diffusion, electron bulk-tail diffusion, and even wall desorption. Fusion ash removal can be simulated beyond D-T plasma characteristic fusion times. Unlike initially high performance copper magnets, the HESTER magnets can be run at the full plasma field of 7.0 T for discharges of arbitrary length. HESTER also provides the options of internal cryopumping, a poloidal separatrix, limiter pumping and external vacuum ducts to test the technical feasibility of different long term pumping concepts.

1.7 High Beta Experiments

Although HESTER, being a high aspect ratio device, cannot achieve world record values of toroidal beta, it should achieve competitive values of $\epsilon\beta_p$ and will also be able to distinguish between flux-conserving and non-flux-conserving limitations, because of its long pulse capability. Because it is heated by ion cyclotron resonance heating, it will not have to lower its high toroidal field in order to do high beta experiments, and thus may achieve higher pressure than previous high beta experiments, despite its higher aspect ratio. Specifically, a 1.5 % average beta discharge in the nominal 7 T toroidal flux density corresponds to an average pressure of 3 atmospheres. Similarly, since all heating will be due to radio frequency waves, it will help to distinguish between bulk plasma pressure limits and those specifically associated with energetic particle injection.

1.8 Transport Experiments

Along with the TFTR beam heating experiment, HESTER will extend the favorable aspect ratio dependence of global electron transport discovered on Alcator C and confirmed in retrospect by discharges in ST, Wendelstein VII and the statistical study of Pfeiffer and Waltz to a higher performance, more reactor-like regime. This will further open up the range of possibilities for tokamak reactors, as well as expanding the physics base elucidating the aspect ratio dependence of all plasma design parameters of interest. It should be noted, however, that the beam heating discharge on TFTR with an aspect ratio of 5.5 will somewhat diminish the physics interest of the transport scaling experiments in the ohmic regime, but will greatly diminish the physics risk of HESTER's primary goals.

1.8 Electron Heating

Electron heating is a by-product, although a major goal in its own right, of the primary mission of HESTER - current drive. Even if no separate electron heating equipment is proposed for HESTER , it arises naturally from the interaction between the electron tail and the bulk electrons in high density current drive, and the lower hybrid current drive system can be easily adjusted to heat electrons without net current. In fact, the current drive experiments at Princeton and M.I.T. were the first definitive demonstrations of the efficient coupling of large amounts of wave energy to electrons, below the electron cyclotron resonance. High electron temperature is a goal in itself, because electron temperatures above 4 keV have not yet been reached in the tokamak program, and because the interaction of the bulk plasma and any current drive mechanism is expected to be a function of electron temperature. Confirmation of favorable aspect ratio scaling of electron transport would allow HESTER to achieve high electron temperatures with considerably less auxiliary power than other machines.

1.9 RF Current Initiation

Although initiation of plasma current with radio frequency waves or electron beams, without ohmic drive, has frequently been postulated, no definitive experiment has yet been performed. The elimination of the expensive initiation "blip", in which an induced electric field in the range 2-20 V/m has been required to raise the plasma temperature to 50 eV, would greatly reduce the cost of power supplies and ease magnet protection from disruptions by allowing thick vacuum vessels. A demonstration of complete plasma control using no ohmic drive at all would lead to major economies in the tokamak as a reactor concept. HESTER is ideally suited for rf current initiation experiments, because its superconducting magnets allow arbitrarily slow current ramps, its high aspect ratio reduces the power requirements of auxiliary current control and it already contains several candidates for current initiation in the equipment necessary for its current maintenance experiments. In particular, the use of superconducting TF coils allows very long preheating, possibly allowing gas evolution to die down before "blip"-free initiation.

2.0 Overview

HESTER is a superconducting tokamak with a 2.0 m major radius, a nominal 0.35 m minor radius and a maximum flux density on axis of 7.00 T . Its major dimensions are shown in Table 2.1. These four facts define the unique place of HESTER in the tokamak program: it is capable of higher field and longer pulses than previous large tokamaks. It also operates routinely and heats at a higher aspect ratio. The HESTER vacuum vessel and ICRF antenna structure will accommodate a plasma discharge up to an elongation of 1.5 and a plasma current of 1.2 MA at $q_{lim} = 2.1$. The above parameters apply to the baseline design to which conservative magnet design principles have been applied. The possibility of an extended performance mode, in which the peak flux density at the toroidal feld magnets is increased from 9.1 T to 11 T and the flux density at the plasma is increased to 8.5 T will also be discussed.

The physics goals of the machine include current drive, using three different candidate methods, to a density-safety factor ratio of 5×10^{19} at electron temperatures near 1 keV and 10 keV, ion heating with ICRF to ion temperatures higher than 10 keV, and the capability of increasing the pressure at full field to an $\epsilon\beta_p$ of 0.5.

2.1 Physics Basis

The overall strategy of HESTER has been to identify the area in parameter space that will allow the achievement of the overall goals stated in Section 1 with the minimum amount of physics risk. The search of parameter space was done largely with the new tokamak system code TOKSYC, which is documented in a companion report [SC82]. After a search through several possible superconducting and cryoresistive Bitter plate machines, the quantitative logic behind a large major radius, high aspect ratio, superconducting tokamak became clear.

1 The selection of superconducting toroidal field coils has the clearest motivation. The superconducting toroidal coils in HESTER have less than 1/10 the overall recirculating power of normal copper coils, occupying the same coil envelope. They thus save operating costs as well as satisfying constraints on total available power at the M.I.T. Plasma Fusion Center. From the point of view of a long pulse, high performance discharge, they have the advantage over the other relatively high and moderate field domestic tokamaks, such as ALCATOR C, PLT and TFTR that the toroidal field does not have to be derated as

the pulse length is increased. In addition to the plasma physics motivation basis, the construction of the first superconducting tokamak in the United States, using an advanced magnet design, will be a major engineering advance in the program. A rationale is included for the selection and the perceived higher reactor relevance of Nb_3Sn vs. superfluid helium as the method of obtaining high performance in a superconducting tokamak.

2 The selection of overall machine size involves obvious trade-offs. From the point of view of both physics and reactor relevance, the size should be as large as that of a commercial tokamak reactor, i.e. as large as possible. A two meter major radius is selected for HESTER, because it is just about the smallest major radius that provides enough space for simultaneous full field, low safety factor current drive, high density, high temperature heating and a complete array of the necessary diagnostics. Two meters is also about the largest radius that allows significant economies due to the use of previously existing facilities at M.I.T.

3 High field has many well-known virtues, including the ability to increase current and thus ion confinement, without increasing volume, and the ability to increase density and thus electron confinement in ohmic discharges. Because of the high aspect ratio of HESTER, it can achieve a 7.0 T plasma using conventional, even scrap, NbTi superconductor. Using an advanced Nb_3Sn superconductor, it is possible to achieve 7.0 T with a high safety margin against disruptions and it is conceivable to achieve 8.5 T with subcooling. While all physics figures of merit scale well with high field, especially $n\tau$, HESTER abandons the traditional "alto campo" approach of M.I.T. of creating the highest achievable field in a compact magnet, in favor of the entirely new class of machine, defined by the HESTER acronym. A 7.0 T plasma is felt to be approximately the best compromise field, since it is at least as high as that of commercial tokamaks, eliminating the need for further scaling, while still being small enough to allow adequate port space to ensure the feasibility of a full range of heating and current drive experiments.

4 High aspect ratio has generally been seen as more appropriate to all toroidal confinement concepts other than a tokamak. However, in the past year, the success of current drive experiments, the establishment of aR^2 scaling for plasma ohmic confinement and the strong suggestion that the fundamental limits on beta are functions of $\epsilon\beta_p$ and pressure only can all be shown to scale favorably for high field, high aspect ratio experiments. High aspect ratio has several engineering benefits, as well, once it is perceived that physics performance is not harmed. It is easier and less expensive to achieve high flux from an ohmic transformer, in order to ensure start-up in the case of unproven current drive techniques, as well as to

investigate super long-pulse operation in the reactor relevant case of partial current drive, supplemented by a small electric field. High aspect ratio allows the addition of external structure or additional helium reservoirs for either eventual upgrade or as a conservative back-up to the original design specifications. If aR^2 continues to hold, as expected, fabrication with poloidal welds in an external vacuum vessel actually permits machine upgrade by the addition of more identical, rectangular cross-section TF coils, increasing the machine major radius.

2.2 Engineering Features

The most striking feature of the HESTER design is the use of circular, superconducting magnets, employing Nb_3Sn cable-in-conduit superconductors. The use of superconducting magnets has long been recognized as favorable for fusion reactor economics, while the benefits inherent in the use of circular magnets and Nb_3Sn stabilization are discussed in Section 8.

Simplified plan and elevation views of the overall layout of the HESTER tokamak are shown in Figures 2.1 and 2.2. The toroidal magnets and vacuum vessel have independent vacuum systems. The exterior vacuum vessel has two double sealed, differentially pumped vacuum seals. The vacuum seals run toroidally, allowing the simplest assembly and disassembly procedure. The top or bottom of the vacuum vessel is removed vertically, in order to remove a toroidal magnet or antenna.

An interior thick-walled vacuum vessel with an actively-cooled double bellows provides the high vacuum containment for the plasma, as well as mounting slots for internal components, such as limiters, rails, antennae and waveguides.

Figure 2.3 illustrates the horizontal port access for HESTER . The available port space is orders of magnitude greater than that of the Alcator devices, with maximum horizontal access at the equator of 18 cm and maximum vertical access of 74 cm, providing a maximum possibility of 18 horizontal ports. While the port space is still small in comparison with many tokamaks, a satisfactory compromise has been reached, allowing adequate access for simultaneous heating and current drive experiments, while retaining the toroidal stiffness necessary for a high field, superconducting magnet design. High aspect ratio is again very helpful in achieving this goal, allowing the many ports, reducing in-plane centering forces due to differential magnetic pressures on the magnets, reducing out-of-plane forces due to vertical fields reacting differential thermal and magnetic pressures on the plasma, and reducing the field attenuation from the magnet to the plasma.

The out-of-plane magnet support structure attempts to be as strong as can possibly be selected for a superconducting magnet system. All Lorentz forces, including the out-of-plane forces, are taken by cold structure. Solid wedges connect the rectangular toroidal field magnet bobbins at the inner leg. Only half of the magnets have ports, so that the outer leg of every second magnet can be connected by a thick, solid wedge. Solid wedges are also placed above and below each of the horizontal ports. Thus, the structural concept is as close to that of the monolithic construction typical of Bitter plate design as is possible using wound, superconducting magnets.

The equilibrium magnets are also superconducting, and are included in the outer toroidal vacuum vessel, sharing the liquid nitrogen radiation shields on the sidewalls with the toroidal field magnets.

The division of the inner vacuum vessel into thick toroidal rings and double walled bellows allows mounting of larger components, such as limiters and antennae, while limiting resistance and thermal stresses due to toroidal deflection. The double walled bellows allows both the thick and thin walled sections to be actively cooled. Under normal operation, the walls would be water cooled, but hot nitrogen would be used for bakeout. As insurance of clean long pulse operation, if the performance of more advanced forms of impurity control is not immediately adequate, the vacuum vessel walls are also manifolded to allow active cooling by subcooled liquid nitrogen.

Figures 2.4 through 2.6 illustrate the overall structural machine concepts for the alternative 24 coil machine. These drawings are historically later than 2.1 through 2.3 and hopefully represent more advanced and detailed concepts. With the notable exception that only the 24 coil design has human port hole access and can be sealed with internal welds, these newer structural concepts are the same as those for HESTER, but have not been drawn to scale for the 36 coil machine.

Figure 2.4 shows an elevation cross-section of the entire machine. An outer dewar surrounds the magnet system, while an inner vacuum can isolates the ohmic heating central solenoid. Each toroidal magnet is in a separate cold case, thermally isolated from warm structure by a superinsulating wrap. The walls of the outer cryostat are lined with liquid-nitrogen-cooled radiation shields. Cold mass support is from the top of the mid-vacuum section of the outer dewar, allowing removal of both covers.

Figure 2.5 shows a plan view of the toroidal magnets, vacuum vessel and vertical ports. A new concept illustrated in figure 2.5 is the addition of a vertical port between every coil, instead of every other coil, making cooling and other utility access easier, as well as improving the feasibility of global limiter pumping through vertical ports.

Figure 2.6 shows several aspects of the TF magnet intercoil structure. Overturning moments are supported by stiff top-to-bottom elements between every other coil, using fasteners and keys on all slip surfaces. Keyways in adjacent coil structures would be match drilled during fabrication of the cases. The toroidal continuity of the TF case/intercoil support is broken by insulated G-10 breaks in two toroidal locations.

Figure 2.7 shows the possibility of winding one of the superconducting magnets in a racetrack, in order to provide tangential viewing of all chords in the plasma. From the drawing, this option does not appear to affect coil size requirements significantly, but stresses and complications in the coil structural design have not yet been analyzed. The drawing does, however, illustrate that the racetrack coil does not have much impact on the vacuum vessel design, the protuberance being comparable in size to other flanges in the system. However, the racetrack winding would create a small amount of asymmetric ripple at the edge and 0.4 % ripple in the center, which could prevent successful ion cyclotron heating at low densities.

References

[SC82] Joel H. Schultz, "TOKSYC 82: A Tokamak System Design Code", M.I.T. Plasma Fusion Center Report PFC/82-27, Nov. 1982

Table 2.1

HESTER Major Machine Dimensions

Major radius	2.0	(m)
Minor radius	0.35	(m)
Maximum toroidal field	7.00	T
Maximum pulse length	24	hrs
Full heating pulse length	10	s
ICRF heating toroidal field	6	T
Maximum plasma current	1.2	MA
Minimum limiter q	1.7	
Maximum ICRF auxiliary heating (10 s)	9	MW
Maximum LH auxiliary heating or current drive	8	MW (cw)
Maximum thermal wall loading	500	kW/m^2

JHS-82482-1

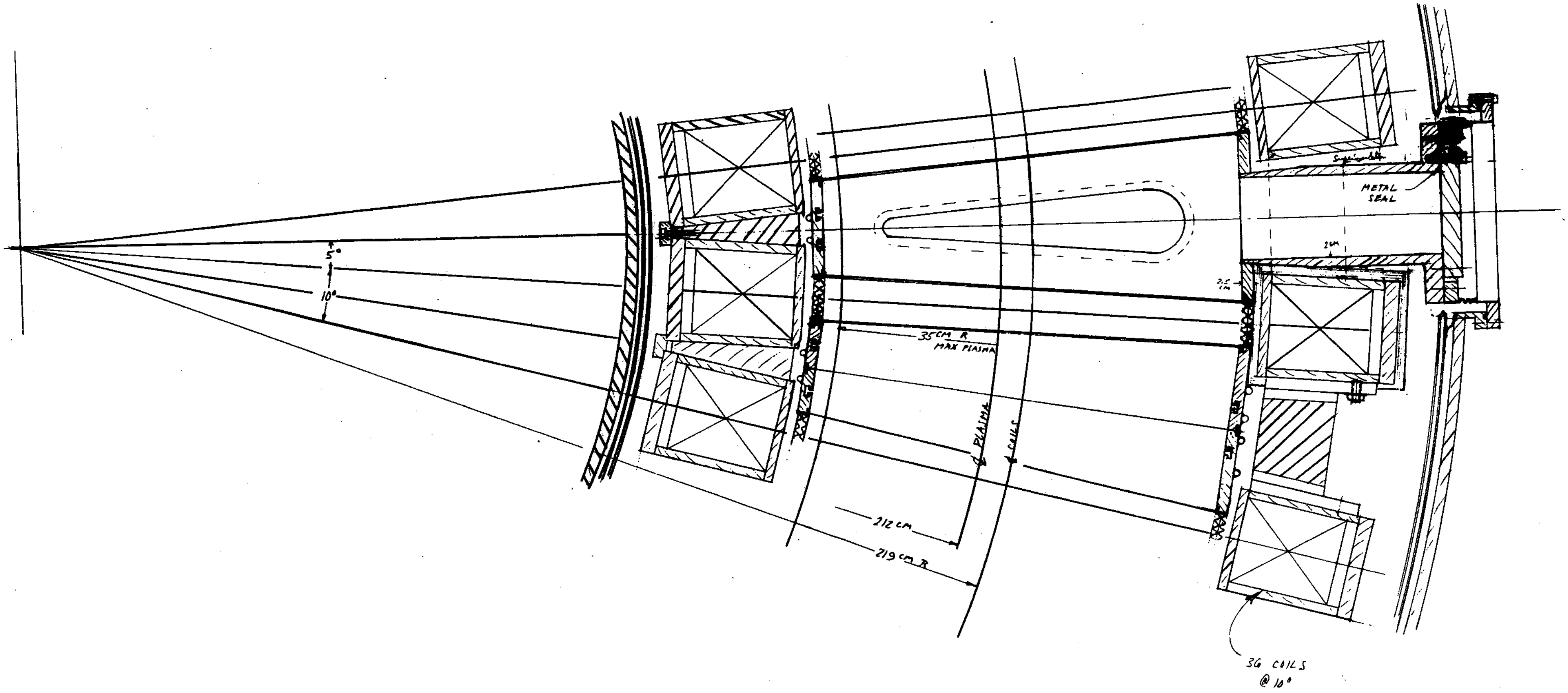

FIGURE 2.1 PLAN VIEW OF HESTER TF MAGNET AND VACUUM VESSEL SYSTEM

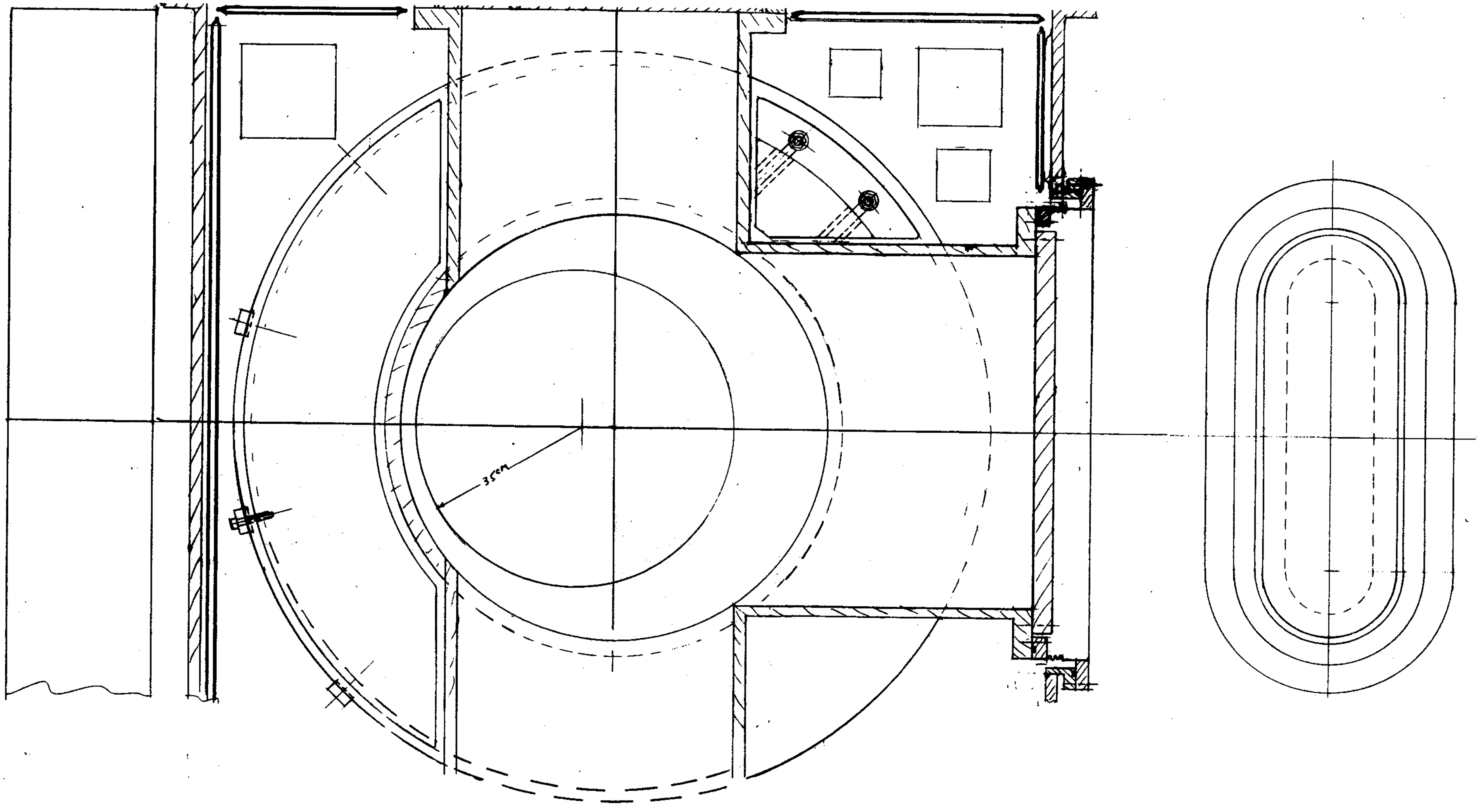

FIGURE 2.2 ELEVATION VIEWS OF HESTER TOROIDAL MAGNET, VACUUM VESSEL AND HORIZONTAL PORT.

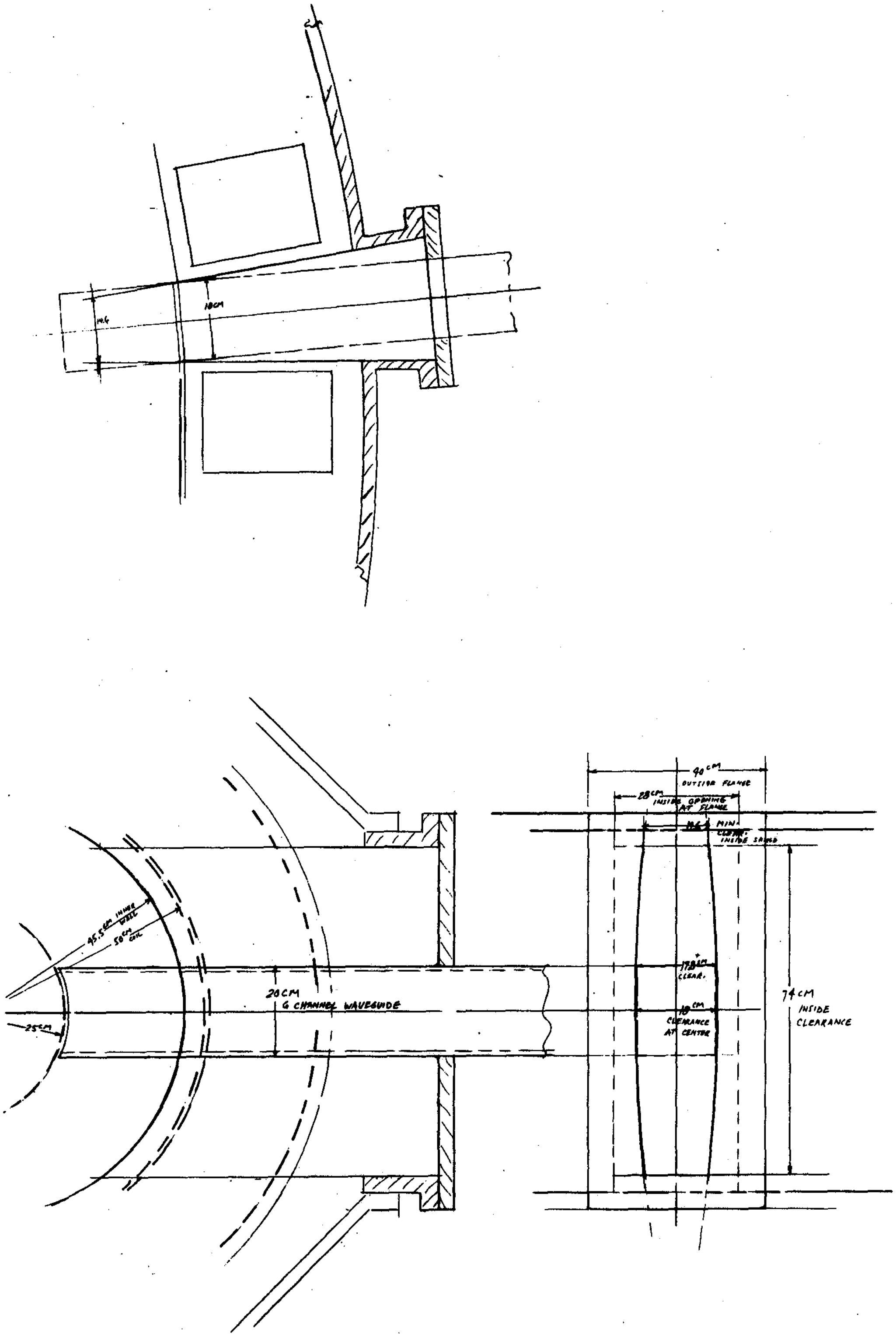

FIGURE 2.3

HORIZONTAL PORT ACCESS ON HESTER

JHS-83-3141

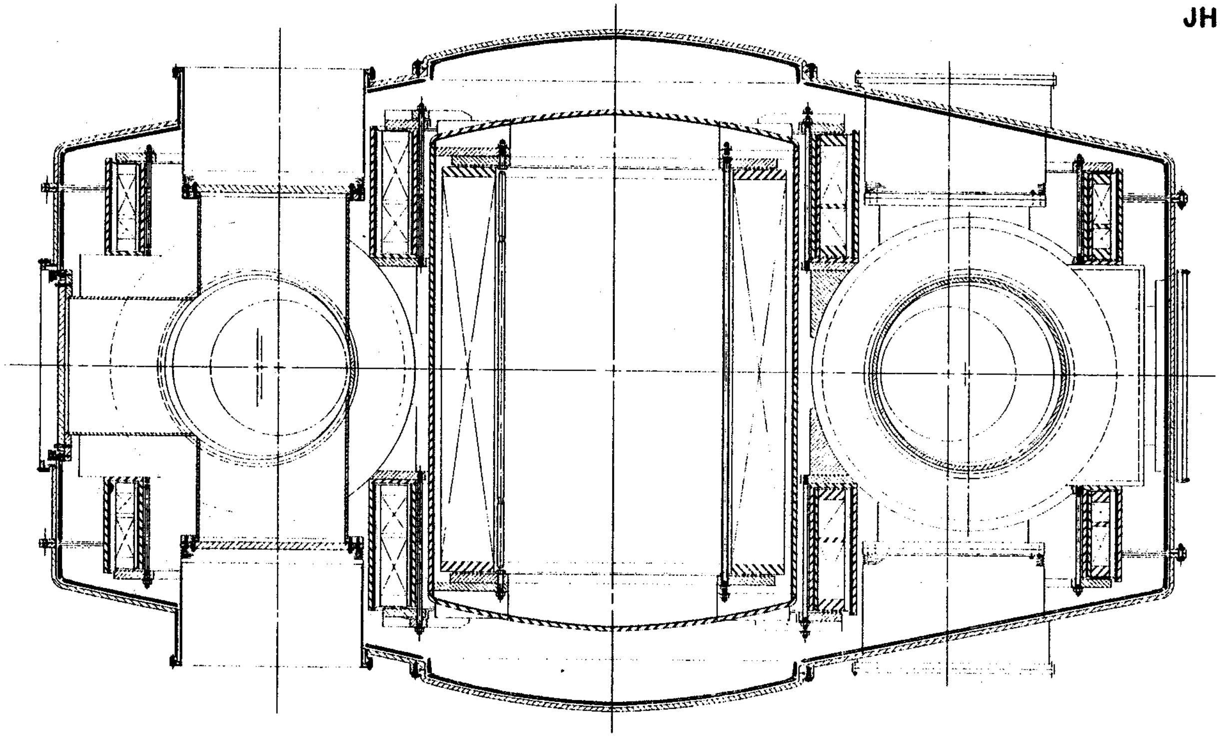

FIGURE 2.4

ELEVATION VIEW OF 24 COIL ALTERNATIVE DESIGN.

JHS-83-3142

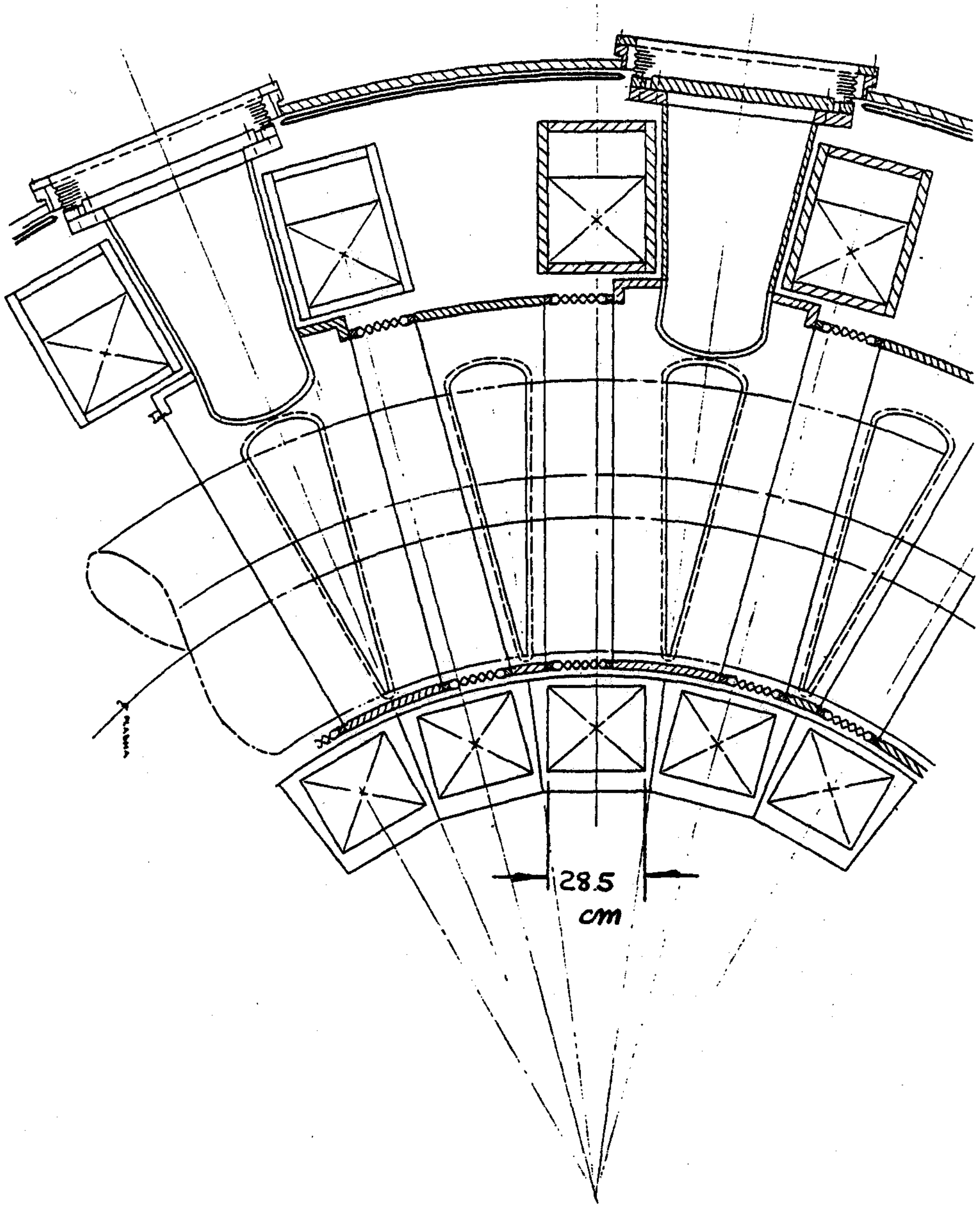

FIGURE 2.5

PLAN VIEW OF EQUATORIAL CROSS-SECTION OF 24 COIL ALTERNATIVE DESIGN.

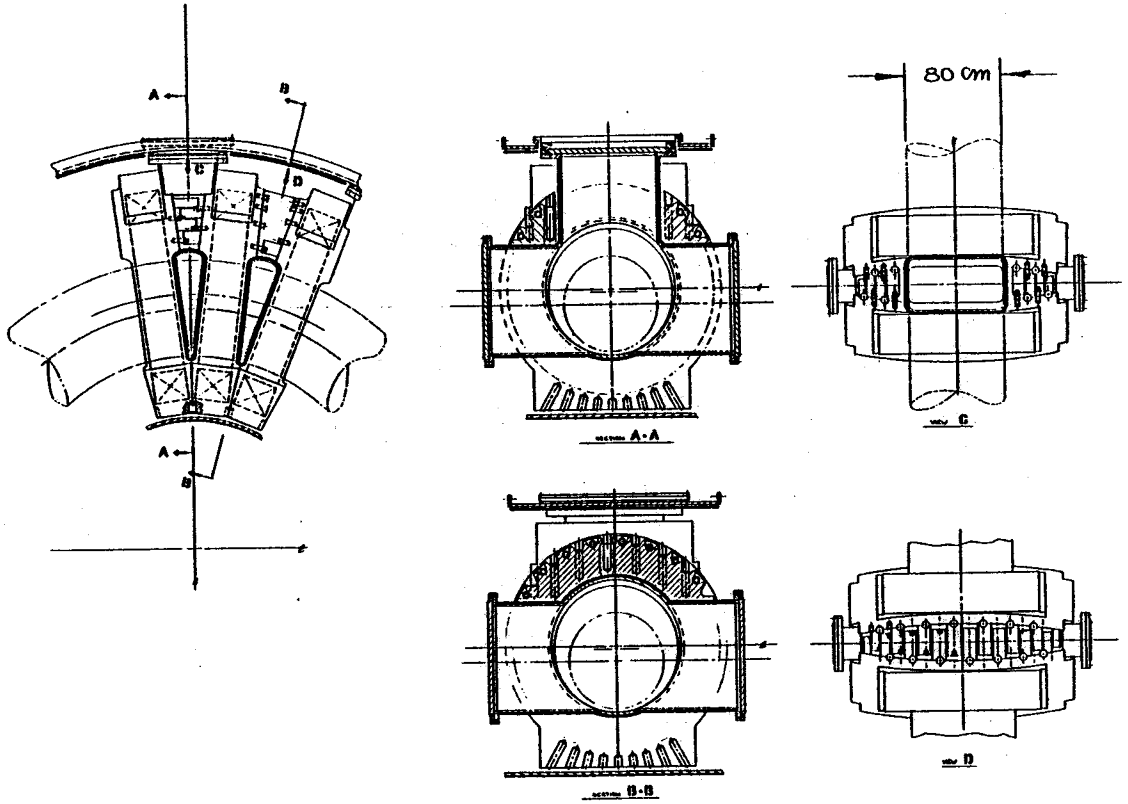

FIGURE 2.6

PARTS AND INTERCOIL SUPPORT STRUCTURE FOR 24 COIL ALTERNATIVE DESIGN.

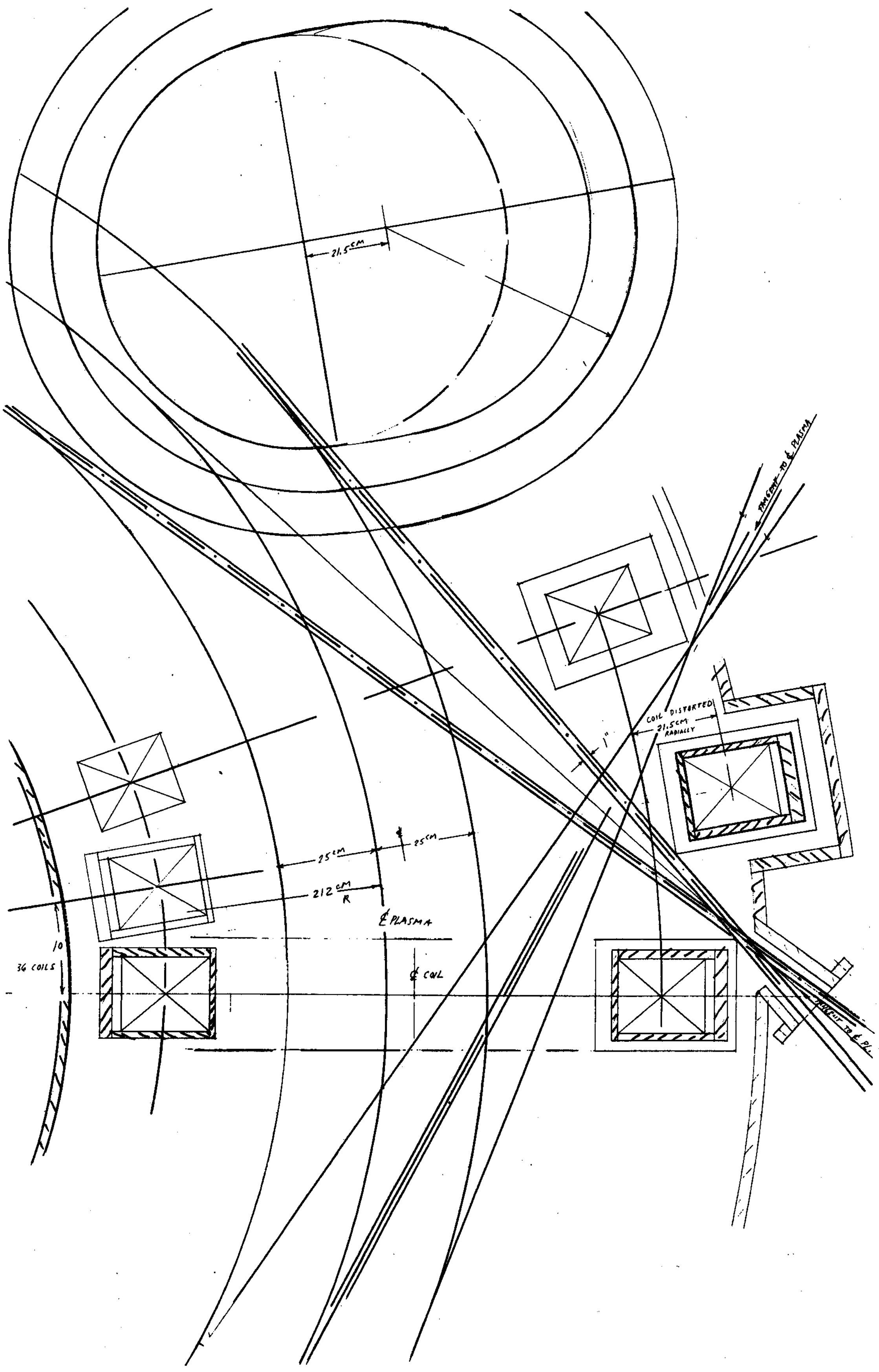

FIGURE 2.7 THE TANGENTIAL VIEWING OPTION ON HESTER WITH ONE EXPANDED TOROIDAL FIELD MAGNET.

3.0 The High $n\tau$ Experiment

Although HESTER is not primarily a high $n\tau$ demonstration device, it will undoubtedly explore the limits of confinement time in the ohmic regime as one of its key experiments. Since a common experience in high temperature and high pressure experiments is that, after an initial drop of a factor of 1.5-2.0, the electron energy confinement time does not change much, while the ion confinement time may also drop by a factor of 1-3, the confinement time achieved in the ohmic experiments is probably the base on which confinement in heating experiments is laid.

HESTER has a fair amount of flexibility in the selection of the plasma minor radius, since the toroidal field magnets within the vacuum chamber have a clear bore of 96 cm. The results shown in the appendix are for a plasma with a 35 cm minor radius. A key feature of the ohmic heating experiments on HESTER would be a systematic variation of the plasma minor radius, as was done on Alcator C [AL82], in order to gain insight both into the physics of transport scaling and to aid selection of the minor radii at which heating and current drive experiments should be done. Models for pressure enhanced transport and ripple transport were included in order to find a reasonable set of global paramaters. However, regimes in which the model predicts that these terms dominate have been generally avoided by selection, for example, of sufficiently low minor radii, because of the unestablished predictive value of these models.

A recent interpretation of the Murikami limit by Bickerton [BI79] gives an achievable n_{eav} of 1.99×10^{20} m^{-3} for a plasma with a major radius of 2.09, a toroidal flux density on axis of 6.9 T, and a safety factor of 2.1 . A more complicated formula by Reynolds [RE80] gives a lower estimate of only 1.12×10^{20} m^{-3} m^{20}. Since the Murikami limit is empirical and recent empirical results, since 1979, have reported some success in exceeding the Murikami limit, we adopt the more optimistic estimate of the density limit.

Global energy confinement was calculated using 3 times neoclassical conductivity for ions, according to Hinton [HI76], and Wolfe's interpretation of Alcator C scaling for electrons [WO82] [AL82].

$$\tau_{Ee} = 0.06 R_o^{2.3} a^{0.8} n_{e20,lineav}$$

where τ_{Ee} is the electron global energy confinement time (s), R_o and a are in meters, and n_{e20} is the line-average electron density (10^{20} m^{-3})

Either Pfeiffer-Waltz or Alcator C scaling appear to be acceptable for predicting global electron energy confinement in high aspect ratio experiments, while the other correlations, used here as checks, fail to predict results in the other high aspect ratio tokamaks, Wendelstein and ST. The various global confinement scalings being compared are listed in equations 50-57 in the documentation of profile_plasma in the accompanying document on the TOKSYC system code [SC82]. The scaling of energy confinement time by Wolfe from Alcator C [WO82] [AL82] agrees well with the statistical study by Pfeiffer-Waltz [PF79]. For the highest $n\tau$ discharge, described by the table in Appendix 3-1, the Pfeiffer-Waltz equation predicts an electron energy confinement time of 182 ms, while the Wolfe formula predicts 184 ms . By contrast, Alcator A scaling predicts 75 ms, Mereshkin scaling predicts 293 ms and Coppi-Mazzucatto scaling predicts 83 ms.

Pfeiffer-Waltz or the similar Alcator C scaling are adopted because they appear to be the only empirical relations which correctly predict the energy confinement time in high aspect ratio tokamak plasmas. In the case of the highest aspect ratio tokamak plasma ever, that of Wendelstein VII with low external ι [US81], Pfeiffer-Waltz predicted the electron energy confinement time within 10 % (although that degree of accuracy is undoubtedly a coincidence), while other scaling laws were wrong by an order of magnitude. For example, a discharge with $n_{eav} = 1.6 \times 10^{19}$, $R_o = 2.0$, $a_{minor} = 0.12$ and $Z_{eff} = 2.3$ [WV76] had an electron energy confinement time of 4.0 ms. The Wolfe scaling gives an electron energy confinement time of 4.1 ms, while Pfeiffer-Waltz scaling gives an electron energy confinement time of 8.2 ms. By contrast the Alcator A scaling gives 1.15 ms while Mereshkin scaling gives 38 ms. For the Wendelstein discharge with the best confinement time at 1.1×10^{20} and ι-bar = 0.55, the reported value of τ_E was $\leq$ 14 ms, while the Pfeiffer-Waltz equation predicts 13.5 ms, Mereshkin predicts 43 ms, Alcator A predicts 2.1 ms and Coppi-Mazzucatto predicts 0.4 ms. The implication is that all scaling laws except for aR^2 break down at very high aspect ratio. Similarly, 23 discharges from ST, which had an aspect ratio of eight, were included as part of the statistical basis of the Pfeiffer-Waltz equations. The best of these discharges (ST-7 in [PF79]) had an electron energy confinement of 10.1 ms. The Pfeiffer-Waltz equation we are using predicts 8.17 ms, while the Alcator A scaling we are using predicts only 3.2 ms. Although some such discharges may exist, we know of no ohmic discharge of any sort that is not predicted correctly within a factor of two by the best unconstrained Pfeiffer-Waltz equation, while the other published correlations we have checked are not correct to within a factor of two for high aspect ratio tokamak discharges. Therefore, "aR^2" scaling is adopted here for the HESTER design because of the moderately large body of empirical circumstantial evidence. Further use of Alcator A scaling in planning studies is justified only by the observation that it is hard to break a bad habit, but it has been incorrect by a factor of two or greater in so many famous cases that its use weakens the meaning of the word "empirical".

Although naR^2 scaling is entirely empirical in its origin, it has appeared at least once previously in an unheralded form, as a theoretical prediction by Kadomtsev [KA78], calibrated against experiment in a global interpretation by Equipe TFR [EQ80]. Kadomtsev's relation for electron conductivity is based on saturating drift-waves, accounting for the effects of trapped-electron effects and toroidal coupling of modes. The TFR equation in which naR^2 scaling appeared is:

$$\tau_{Ee} = n_e\sqrt{q_a}a^2R\left[q_a^{2/3}R^{19/24}B_t^{-1/3}a^{-23/24}\right]$$

Equipe TFR dismisses the term in brackets as "practically constant," since it only varies from 0.167 in a typical Alcator discharge to 0.11 in a typical PLT discharge, and emerges with na^2R scaling, used in the remainder of the abovementioned work. The scaling with $B_t^{-1/3}$ and $q_a^{7/6}$ which remains after naR^2 is extracted looks curious and has not yet been either confirmed or denied as part of the HESTER design justification effort.

A theoretical basis for aR^2 scaling appears again in hidden form in a paper by Minardi [MI81], based on the electrostatic drift instability arising from the ratio of shear damping, due to toroidal effects. In Minardi's formulation, nongeometric terms can be removed from a complex expression for global transport, which reduces to an $R_o^{8/3}a^{2/3}$ dependence, which is extremely close to Wolfe's empirical formula.

With the above assumptions, the maximum $n\tau$ achievable in HESTER is 2.6×10^{19} , where n is the central electron density (m^{-3}) and τ is the global energy confinement time. It is unlikely that this will break any records, since TFTR operation will begin before HESTER operation, but the achievement of a 184 ms electron energy confinement time would establish a very strong base for the heating experiments to follow.

References

[AL82] Alcator C Group, "Energy and impurity transport in the Alcator C Tokamak," IAEA-CN-41, 9th Internatl Conf on Plasma Phys and Controlled Nuclear Fusion Research, Baltimore, MD, Sept 1982

[CO79] B. Coppi and E. Mazzucato, "Transport of electron thermal energy in high temperature plasmas, " Phys Letters Vol 71A, 4, 337, May 1979

[EQ80] Equipe TFR, "Tokamak scaling laws, with special emphasis on TFR experimental results," Nuc Fus, Vol. 20, No. 10, 1980

[HI76] F.L. Hinton and R.D. Hazeltine, "Theory of plasma transport", Rev. Mod. Phys., Vol.48, No.2, Part 1, April 1976

[KA78] B.B. Kadomtsev and O.P. Pogutse, Plas Phys and Cont Nuc Fus Resc (Proc. 7th Int Conf. Innsbruck), Vol. 1, IAEA, 415, 1978

[MI81] E. Minardi, "Theoretical scaling law for ohmically heated tokamaks," Max-Planck Institut fur Plasmaphysik Report IPP 1/183, June 1981

[PF79] W. Pfeiffer and R.E. Waltz, "Empirical scaling laws for energy confinement in ohmically heated tokamaks, " Nuc Fus, Vol 19, No 1, 1979

[US81] Joint US-Euratom Report, "Stellarators: Status and future directions," Max - Planck Institut für Plasma_physik Report IPP-2/254, July 1981

[SC82] J.H. Schultz,"TOKSYC 82: A Tokamak System Design Code," M.I.T. Plasma Fusion Center Report PFC/RR-82-27, Sept 1982

[WO82] S. Wolfe, private communication

[WV76] W VII A Team, "Ohmic heating in the W VII-A stellarator," 6th Conf Proc Plas Phys and Cont Nuc Fus Res, Berchtesgaden, 81, IAEA-CN-35/D2, 1976

Appendix 3-A: Plasma Parameter Tables: Ohmic Experiment

HIGH NTAU EXPERIMENT DESCRIPTION

n_{eavMur}	Murikami limit on average electron density	$1.986 \times 10^{20}\mathrm{m}^{-3}$
n_{eavRe}	Reynolds limit on average electron density	$1.123 \times 10^{20}\mathrm{m}^{-3}$
f_z	particle fraction of the dominant impurity	0.0200
Z_{imp}	atomic number of the dominant impurity	6

CENTRAL PLASMA PROPERTIES - HIGH NTAU EXPERIMENT

T_i	ion temperature	1.134 keV
T_e	electron temperature	1.265 keV
B_t	field on axis	6.695 T
n_i	ion density	$2.021 \times 10^{20}\mathrm{m}^{-3}$
f_{He}	helium particle fraction	0.0
f_z	particle fraction of the dominant impurity	0.0200
f_D	deuterium fraction of the hydrogen	0.0
f_T	tritium fraction of the hydrogen	0.0
Z_{imp}	atomic number of the dominant impurity	6
J_p	plasma current density	5.955 $\mathrm{MA/m^2}$
n_e	electron density	$2.223 \times 10^{20}\mathrm{m}^{-3}$
n_z	density of the dominant impurity	$4.042 \times 10^{18}\mathrm{m}^{-3}$
Z_{av}	average Z of the plasma	1.100
Z_{eff}	effective Z of the plasma	1.564
η_{cl}	classical plasma resistivity	27.01 nOhm-m
η_{ORNL}	plasma resistivity (FEDC design code)	52.35 nOhm-m
η_{Parker}	plasma resistivity (Parker)	23.45 nOhm-m
η_{Hirsh}	plasma resistivity (Hirshman),	19.08 nOhm-m
Q_{ei}	electron-ion energy exchange power density	619.6 $\mathrm{kW/m^3}$
Q_{eiBrag}	electron-ion energy exchange power density (Bragiinski)	619.6 $\mathrm{kW/m^3}$
$Q_{eiKaplan}$	electron-ion energy exchange power density (Kaplan)	757.3 $\mathrm{kW/m^3}$
P_{brem}	Bremsstrahlung power loss density	46.46 $\mathrm{kW/m^3}$

CENTRAL PLASMA PROPERTIES - HIGH NTAU EXPERIMENT (continued)

P_{ohm}	classical ohmic power density	958.0 kW/m^3
P_{synch}	synchrotron power loss density	27.16 W/m^3
$P_{synchatten}$	synchrotron power loss density (Attenberger)	31.72 W/m^3
P_{line}	dominant impurity line radiation loss density	52.73 kW/m^3
P_{alpha}	alpha power genertion density	0.0 W/m^3
$P_{dIdrive}$	power density required by current drive	0.0 W/m^3
a_{mueff}	effective atomic mass of the fuel	1
Λ_D	Debye length of the plasma	17.73 μm
r_{Le}	Larmor radius of the electrons	17.93 μm
v_{Ti}	thermal velocity of the ions	466.1 km/s
v_{Te}	thermal velocity of the electrons	21.08 Mm/s
v_A	Alfven speed of the plasma	9.878 Mm/s
σ_{vdt}	reactivity of a D-T plasma	1.346×10^{-26}m^3/s
ω_{uh}	upper hybrid frequency	1.445 Tradians/s
Ω_{ce}	cyclotron frequency ofthe electrons	1.176 Tradians/s
ω_{pe}	electron plasma frequency	840.6 Gradians/s
Ω_{ci}	ion cyclotron frequency	639.4 Mradians/s
ω_{lh}	cold plasma lower hybrid frequency	24.10 Gradians/s
ω_{pi}	ion plasma frequency	19.60 Gradians/s
β_t	toroidal beta	0.00479
p_{mag}	magnetic pressure	17.84 MPa
τ_e	electron-ion momentum exchange time (Duchs)	5.117 μs
τ_{eHH}	electron-ion momentum exchange time (Hinton)	2.093 μs
τ_i	ion-ion momentum exchange time (Duchs)	384.7 μs
τ_{iHH}	ion-ion momentum exchange time (Hinton)	111.3 μs

CENTRAL PLASMA PROPERTIES - HIGH NTAU EXPERIMENT (continued)

ν_{estar}	electron collisionality parameter (Duchs)	21.18
$\nu_{estarPf}$	electron collisionality parameter (Pfeiffer)	16.52
ν_{istar}	ion collisionality parameter (Duchs)	15.54
$\nu_{istarPf}$	ion collisionality parameter (Pfeiffer)	9.937
χ_{iBP}	banana-plateau ion thermal diffusivity (Duchs)	146.7 mm^2/s
$\chi_{iPS,Duchs}$	Pfirsch-Schluter ion thermal diffusivity (Duchs)	6.301 mm^2/s
$\chi_{i,Duchs}$	total ion thermal diffusivity (Duchs)	0.153 (m^2/s)
χ_{iHH}	ion thermal diffusivity (Hinton)	60.88 mm^2/s
R_{neo}	assumed ratio of real to theoretical ion thermal diffusivity	3
χ_i	ion thermal diffusivity	459.1 mm^2/s
χ_{iRT}	ripple trapping ion thermal diffusivity	20.39 mm^2/s
χ_{iRP}	ripple plateau ion thermal diffusivity	9.539 mm^2/s
$\chi_{iripple}$	total ripple ion thermal diffusivity	9.559 mm^2/s

GLOBAL PLASMA PARAMETERS - HIGH NTAU EXPERIMENT

V_r	resistive voltage drop	1.835 V
J_o	central current density	6.045 MA/m^2
q_o	central safety factor	0.800
p_{av}	average plasma pressure	42.11 kJ/m^3
p_{av}	average plasma pressure in atmospheres,	0.42 atm
W_e	total electron energy stored in the plasma	112.1 kJ
$T_{ioohmGill}$	central ion temperature for ohmic heating (Gill)	3.655 keV
$T_{eoTioTFR}$	sum of the central electron and ion temperature (TFR)	3.230 keV
I_p	total plasma current	913.9 kA
L_p	total plasma inductance	9.272 μH
ψ_p	inductive volt-seconds required by the plasma	8.474 V-s
I_{pJET}	total plasma current (JET)	1.064 MA
I_{pbrom}	total plasma current (Bromberg)	692.0 kA
q_{lim}	safety factor at the limiter	2.100
B_v	Shafranov vertical field on axis	141.3 mT
ϵ_{betap}	epsilon - beta poloidal product	0.0353
β_{av}	average toroidal beta	0.00174

GLOBAL POWER BALANCE - HIGH NTAU EXPERIMENT

τ_E	global energy confinement time	115.0 ms
$\tau_{Enoripple}$	global energy confinement time, exclusive of ripple	116.2 ms
τ_{Eineo}	ion energy confinement time, related to neoclassical transport	74.52 ms
τ_{EiGill}	ion energy confinement time (Gill)	393.0 ms
τ_{Ei}	total ion energy confinement time, including ripple	73.48 ms
τ_{EePW}	Pfeiffer-Waltz electron energy confinement time	120.6 ms
$\tau_{EeWolfe}$	electron energy confinement time (Wolfe)	184.4 ms
τ_{EeAlc}	electron energy confinement time, Alcator scaling	55.85 ms
τ_{EeMer}	electron energy confinement time, Mereshkin scaling	168.3 ms
τ_{EeCM}	Coppi-Mazzucatto scaling of energy replacement time	56.25 ms
τ_{Ee}	empirical electron energy confinement time	213.2 ms
R_{chiep}	electron conductivity enhancement factor, due to pressure driven modes	1.021
P_{eemp}	empirical electron energy transport loss	525.7 kW
P_{ineo}	ion energy transport loss, scaled from neoclassical,	1.243 MW
P_{bremt}	total Bremsstrahlung loss the plasma	66.49 kW
P_{alphat}	total alpha power generation in the plasma	0.0 W
P_{ohmt}	total neoclassical ohmic loss of the plasma	1.879 MW
P_{syncht}	total synchrotron radiation loss of the plasma	25.45 W
$P_{lineradt}$	total line radiation loss of the plasma	106.3 kW
P_{ei}	total power flow from the electrons to the ions	1.215 MW
$P_{dIdrive}$	total rf power dissipated, due to current drive	0.0 W
$P_{lhIdrivePLTbest}$	best case PLT scaling for lower hybrid current drive power	27.65 MW
$P_{rfIdriveAlcCbest}$	best case Alcator C scaling for rf current drive power	34.56 MW
$A_{lcCbest10}$	best case Alcator C scaling for rf current drive power at 10 T Prfldrive	23.65 MW
P_{auxeq}	total auxiliary heating or cooling power required for global energy balance	63.02 kW

GLOBAL POWER BALANCE - HIGH NTAU EXPERIMENT (continued)

P_{bremav}	average Bremsstrahlung loss of the plasma	13.76 kW/m^3
$P_{synchav}$	average synchrotron power generation of the plasma	5.269 W/m^3
$P_{lineradav}$	average line radiation loss of the plasma	22 kW/m^3
$P_{alphaav}$	average alpha power generation of the plasma	0.0 W/m^3
P_{drfav}	average rf power dissipated, due to current drive	0.0 W/m^3
P_{eiav}	average power flow from electrons to ions	251.5 kW/m^3
P_{ohmav}	average neoclassical ohmic loss of the plasma	388.9 kW/m^3
P_{loss}	total power loss from the plasma	1.942 MW
P_{wsurf}	average power loss through the plasma surface	68.47 kW/m^2

4.0 The ICRF Heating Experiment

The ICRF heating experiment on HESTER will be the first domestic tokamak experiment with the possibility of duplicating the neutral beam heating results expected on large tokamaks, such as TFTR, JET, JT-60 and Big Dee. The fundamental uncertainties of present day physics scaling in the rf heated regime prevent a definitive statement of the expected plasma performance, but the implications of different assumptions will be discussed below, the more optimistic of which predict the attainment of thermonuclear fusion regime pressures. ICRF heating will also be used as a supplement to current drive experiments, providing the high temperatures that may be an important limitation to lower hybrid current penetration and which are an absolute necessity to efficient current drive with alternative rf current drive mechanisms. Ultimately, the ICRF and lower hybrid electron heating supplies will be run simultaneously in order to test plasma pressure limits, as described in the second half of this chapter. As rf power supplies are upgraded, the final mission of the ICRF current drive equipment will be as the source of thermal wall loading for the engineering testing of all first wall components, including the ICRF equipment itself.

The ICRF heating experiment is performed using the VHF transmitter circuits obtained by M.I.T. for use in the Alcator C experiment. Because HESTER has over treble the major radius of Alcator C, as well as considerably more access for each port, she will be able to deploy the entire 9 MW of available rf power, while still permitting adequate current drive and plasma diagnostics. A system of 10 antennae will be installed, each one similar to the antenna design being tested in Alcator C, which will heat the HESTER plasma at double the proton cyclotron resonance frequency at 6.0 T. The present ICRF system can also heat central ions up to the nominal machine field on axis of 7 T, without modification.

4.1 ICRF Heating Experiment: Physics Basis

The principal purpose of the ICRF heating experiments on HESTER is to couple 9 MW of ICRF power into a tokamak plasma and possibly to duplicate the temperatures and pressures of the large neutral injection experiments, using ICRF only. This obvious goal of the world tokamak program has not been definitively planned, although the planned addition of 15 MW of ICRF to 10 MW of neutral injection in JET [RE82] may achieve these same results, if the global energy scaling for ion heating favors low aspect ratio plasmas. TORE SUPRA plans to include 6 MW of ICRF heating and 6 MW of lower hybrid heating [AY82]. JT-60 plans to deposit 10 MW of lower hybrid power and 2-3 MW of ICRH vs. 20 MW of neutral beam injection [SH82]. Thus, the HESTER experiment will deploy about the same total rf power as much larger experiments into a plasma with higher magnetic field. To the best of our knowledge, the HESTER experiment will be the only tokamak with the planned capability of making a definitive test of the ability of second harmonic majority species heating to reach thermonuclear plasma regimes. This heating method was identified in the INTOR interim report [IN82] as a particularly reactor relevant method of ICRF heating, because of its compatibility with waveguide launching. The planned ICRF launching frequencies of the JET and TORE SUPRA experiments correspond to minority ^{3}He heating near full field, while the JT-60 90 MHz capability corresponds to second harmonic hydrogen heating at 3.0 T (2/3 full field), but less than 3 MW of injection at 90 MHz is planned.

4.1 Background

Ion cyclotron frequency heating has recently come to be the favored method of heating tokamak reactors [IN82], [FL81], because of the perceived higher efficiency, compactness, lower complexity and cost in comparison with neutral beams. While the technological advantages of ICRF heating have been known for some time, acceptance as a reactor concept was delayed because of the greater early successes of neutral beam heating and the inability to this day of achieving significant heating at the plasma majority species fundamental frequency. Within the past few years, successful ICRF coupling to tokamak plasmas, using either minority species heating or majority species harmonic heating, has been achieved on JFT-2 [JF82] [KI82], TFR [GI82], and, most significantly, on PLT [HO82], which achieved peak ion temperatures above 3 keV.

The only tokamak to achieve a significant rise in temperature using second harmonic proton heating, the dominant mechanism proposed for use in HESTER, is PLT [HO82], where an effective temperature of 2.3 keV was achieved for an rf power of 1.6 MW at 42 MHz and a line average electron density of $3.8 \times 10^{19}/m^3$. The fixed frequency of the available rf supplies necessitated reducing the toroidal field to 1.4 T. The best heating discharges were at a plasma current of 380 kA, somewhat smaller than the 450 kA discharges in which the best minority heating was achieved. Thus, if the best minority heating and second harmonic proton heating discharges are normalized to both density and current, the minority heating is more efficient by only 20 %, which can probably be explained by the greater charge exchange losses in a hydrogen plasma [HO82]. The comparison between the best discharges, using different ICRH mechanisms is shown in Table 4.1 [IN82].

4.2 Heating Efficiency

The efficiency of either ICRF or lower hybrid electron frequency is discussed in this section. As is well known, the geometry dependence of electron transport is somewhat controversial in the well studied ohmic transport regimes, lacks well tabulated results in the auxiliary heated regime and lacks any noncollisional discharges in the RF heated regimes. Thus, any predictions of heating efficiency on HESTER are for the purpose of intellectual curiosity as to what commonly used models might predict, as well as to discern whether there are any obvious flaws in the machine mission description. The high field on axis is beneficial to plasma heating efficiency, since it permits the increase of current without increasing plasma volume and allows higher densities in the ohmic regime where they are most useful. However, since HESTER has a higher aspect ratio than other high performance tokamaks, a breakdown in the "Alcator C" electron transport scaling discussed the favorable dependence on aspect ratio of electron transport discussed in chapter 3 would harm heating performance, but would not prevent a significant range of heating experiments. However, as discussed in chapters 6 and 7, the achievement of a broad range of current drive experiments would necessitate the purchase of additional current drive power beyond that described here, if confinement is disappointing. Hopefully, high aspect ratio discharges on TFTR, such as the 310 cm by 55 cm neutral beam heating discharges, will eliminate much of the uncertainty.

While the ability of a high aspect ratio machine, such as HESTER, to achieve effective heating appears to be highly dependent on the truth of Alcator C scaling for electrons, the high field allows a sufficiently high plasma current that the scaling for heating efficiency is favorable for several popular scaling relations. The relative heating efficiencies for the next generation of tokamaks according to these scaling relations are shown in Table 4.2.

For τ proportional to naR^2, the achievable temperature for a given auxiliary heating power scales as:

$$\frac{T_e}{P_{aux}} = A \tag{4.1}$$

For τ proportional to I_p at fixed q, the achievable pressure for a given auxiliary heating power scales as:

$$\frac{nT_e}{P_{aux}} = \frac{B_t}{R^2} \tag{4.2}$$

For τ proportional to $I_p a$ at fixed q,, suggested by neoclassical ion transport in the plateau regime, the achievable pressure for a given auxiliary heating power scales as:

$$\frac{nT_e}{P_{aux}} = \frac{B_t}{AR} \tag{4.3}$$

As Table 4.2 indicates, scaling with aspect ratio predicts that HESTER will have about the same efficiency as TFTR and up to double that of other machines (and that TFTR will have four times the efficiency it expects!). Scaling with current, the efficiency should be about double that of TFTR or Big Dee and considerably higher than other machines. The efficiency of heating in JET, using this relation, is astonishingly low. If global transport scaled as $I_p a$, the heating efficiency of HESTER would be the same as that of TFTR or Big Dee and less than a factor of two higher than that in Tore Supra or JT-60. Of course, HESTER is smaller than the other next generation of reactors, and it is only to be expected that its heating efficiency should be greater. Furthermore, it is not really to be expected that there should be a global transport law of any significance over the entire range of auxiliary heated plasmas, when there are obviously different geometry and density dependences of ion and electron transport and ion-electron energy interchange. The appearance of these popular formulae in planning exercises largely reflects the immaturity of our physical understanding. As a last caveat, one can't help noticing that all three methods predict that the best performance will come from American tokamaks and all three scaling relations were suggested by Americans, but this is undoubtedly a pure coincidence.

In spite of all caveats, the significant feature of this comparison is that two effects, high field and high aspect ratio seem to be cancelling, so that moderately high efficiency is predicted over a range of assumptions. A comparison between temperature and density using the TOKSYC system code simulation of HESTER vs. the two global relations used in the Big Dee design review show a surprising insensitivity of HESTER's performance during ion cyclotron heating, as a function of global transport assumptions, as shown in figure 4.1. The current and current-minor radius scalings used here are:

$$\tau_E = 0.06 I_p \tag{4.4}$$

and

$$\tau_E = 0.13 I_p a \sqrt{\kappa} \tag{4.5}$$

TOKSYC assumes separates ion and electron temperature, assuming three times ion neoclassical transport according to Hinton [HI76] and twice Alcator C electron transport according to Wolfe (Ch. 3), while the simple global transport equations give an average species-independent temperature. As seen in figure 4.1, the correlation most favorable to aspect ratio (Wolfe) predicts an ion temperature that is double that predicted by the least favorable correlation (I_pa) at low density. There is no significant difference between the predictions of the three assumptions at high density.

For smaller experiments, one might not be limited by available power so much as by power launching density W/m^2 over the available surface. For Alcator A scaling, the achievable temperature for a given power density would have scaled as:

$$\frac{T_e}{P_w} = a\,,$$

while for Alcator C scaling, the achievable temperature for a given power density scales as:

$$\frac{T_e}{P_w} = R^2\,.$$

It is this limitation that prevents Alcator C from achieving the highest machine temperatures. By almost any scaling law, it should achieve the best heating efficiency at any density, but it cannot launch more than approximately 4 MW into the plasma by either ICRF or lower hybrid before all four of its small horizontal ports are used up. If it were not for this horizontal port limitation, much of the HESTER mission could be achieved at less expense. Even with this limitation, it will be of great importance to both the lower hybrid and ICRF experiments on HESTER to complete both the lower hybrid and ICRF experiments on Alcator C at full power.

Perhaps further insight into expected scaling can be gained by examining the implications of global correlations which appear to have both a theoretical and empirical basis. Gill has derived a global empirical relation for the ion temperature in the regime in which ion-electron energy exchange is negligible [GI74], which appears to fit both low and high power heating experiments on many tokamaks [GI80]. Gill's scaling law for ion temperature as a function of heating power is:

$$T_i = 3.2 \times 10^8 \left[\frac{f_i P_{NI} B_\phi^2}{n_{eav} q_L \sqrt{A_i} f(\nu^*_{iav})} \right]^{0.4} \qquad eV$$

where f_i is the fraction of the injection power deposited in the ions and ν^*_{iav} is the line average ion collisonality. The function of collisionality is:

$$f(\nu^*_{iav}) = 1$$

for $\nu^*_{iav} > 1.26$, and

$$f(\nu^*_{iav}) = 0.88\nu^{*0.55}_{iav}$$

for $\nu^*_{iav} < 1.26$.

For HESTER , Gill's formula predicts a central ion temperature of 35 keV at a central ion density of 5×10^{19} for a total absorbed power of 9.6 MW (12 MW short pulse launched), while the TOKSYC system code predicts 29 keV, with no ripple. This "runaway" to thermonuclear grade plasmas is what is predicted above a certain ion heating level due to the favorable temperature dependence of ion transport dominated by neoclassical transport; it is predicted by almost any scaling model to be achievable at low density in any tokamak that can maintain adequate plasma purity.

It has been objected that a high aspect ratio tokamak will provide a poor target for an ion heating experiment, because previous intense neutral injection heating experiments have reported that the heating efficiency on PDX, defined as stored plasma energy divided by injection power (the global energy confinement time in an injection dominated discharge), increases as I_p [HA82], while on ISX-B, the global energy confinement time increases as $I_p^{3/2}$ [SW81]. Reasoning from the perceived benefits of plasma current, which scales as a^2/R or R/A^2, some planners have concluded that a good heating experiment should have a low aspect ratio. Gill's formula predicts that, for a fixed dimension machine, ΔT will improve as $I_p^{1.1}$, if current is increased by decreasing q_L, and as $I_p^{1.4}$, if current is increased by increasing toroidal field at constant q_L, which is, of course, compatible with the abovementioned experiments, since data from PDX and ISX-B were included in deriving Gill's formula. However, if one scales from this formula to a new machine with different dimensions, the dependence of temperature on power in Gill's formula scales as

$$\frac{T_i}{\sqrt{P_{NI}}} = \frac{B^{1.43}}{q_L^{1.1}A^{0.58}R^{0.39}}$$

Thus, the unfavorable dependence of temperature on aspect ratio is not nearly as high as that suggested by a simple scaling from plasma current, when the machine dimensions are also changed.

Another analytical approach which relates temperature limits to pressure limits through the mechanism of magnetic surface weakening by tearing modes at rational surfaces was suggested by the Equipe TFR [EQ80]:

$$n_e(0)\,[T_e(0) + T_i(0)] = \frac{9 \times 10^8}{\sqrt{A_i}} \epsilon q_a^{\frac{1}{4}} B_t^2 \sqrt{1 + \frac{P_{add}}{P_\Omega}}$$

This limit permits a central density ion plus electron temperature limit of 60 keV-10^{20}m^{-3} in HESTER, which is higher than that predicted by transport models. This formula also predicts a slower than linear degradation of ion heating effectiveness with aspect ratio, because of the decreased ohmic power for a fixed safety factor in a high aspect ratio plasma.

Although there is certainly an unfavorable aspect ratio dependence for ion heating, and perhaps a favorable dependence for electron heating, this dependence is balanced by the beneficial effects of higher field on ion containment. The machine dependent effects such as the ability to generate higher field with a given field at the coils and the ability to place more heating elements around the plasma give the HESTER plasma much higher performance than might have been initially believed for a high aspect ratio plasma.

References

[AD74] J. Adam et al, "Wave generation and heating in the ST-tokamak at the fundamental and harmonic ion cyclotron frequencies," IAEA-CN-33/A 3-2, p.65, 1974

[AY82] R. Aymar, "Supplementary heating in Tore Supra", Proc 3rd Joint Varenna-Grenoble Internatl Symp on heating in toroidal plasmas, EUR 7979 EN, March 1982

[EQ80] Equipe TFR, "Tokamak scaling laws, with special emphasis on TFR experimental results," Nuclear Fusion, Vol. 20, No. 10, 1980

[FL81] C.A. Flanagan et al, "Fusion Engineering Device Design Description", Oak Ridge National Laboratory Report ORNL/TM-7948, Dec. 1981

[GI80] R.D. Gill, "Ion containment in neutral injection heated tokamaks," Culham Laboratory Report CLM-P671, 36 p, Sept. 1981

[GI82] J.P. Girard, "Energy confinement in the TFR Tokamak during additional heating: A possible explanation," Proc 3rd Joint Varenna-Grenoble Internatl Symp on heating in toroidal plasmas, EUR 7979 EN, March 1982

[HA82] R.J. Hawryluk et al, "Heating efficiency of high power perpendicular neutral beam injection in PDX," Princeton Plasma Physics Laboratory Report PPPL-1882, March 1982

[HI76] F.L. Hinton and R.D. Hazeltine, "Theory of plasma transport", Rev. Mod. Phys., Vol.48, No.2, Part 1, April 1976

[HO82] J. Hosea, "High power ICRF heating on PLT and extrapolation to future devices," Proc 3rd Joint Varenna-Grenoble Internatl Symp on heating in toroidal plasmas, EUR 7979 EN, March 1982

[HW82] D.Q. Hwang et al, "High power ICRF and ICRF plus NB heating on PLT," 9th International Conf Plasma Phys and Cont Nuclear Fusion Research, IAEA-CN-41, Baltimore, MD, Sept 1982

[IN82] INTOR Phase One Report, International Atomic Energy Agency, Vienna, 1982

[JF82] JFT-2 Group, "ICRF heating experiment in JFT-2", Proc 3rd Joint Varenna-Grenoble Internatl Symp on heating in toroidal plasmas, EUR 7979 EN, March 1982

[KI82] H. Kimura, "ICRF heating experiment in JFT-2," 9th International Conference on Plasma Physics and Controlled Nuclear Fusion Research, IAEA-CN-41, Baltimore, MD, Sept 1982

[RE82] P.H. Rebut, "JET Joint Undertaking: March 1982" Proc 3rd Joint Varenna-Grenoble Internatl Symp on heating in toroidal plasmas, EUR 7979 EN, March 1982

[SH82] Y. Shimomura, "NBI and RF Heating of JT-60", Proc 3rd Joint Varenna-Grenoble Internatl Symp on heating in toroidal plasmas, EUR 7979 EN, March 1982

[SW81] D.W. Swain et al, Nuc Fus, 21, 1409, 1981

[WO82] S. Wolfe, private communication

Table 4.1

Best Experimental ICRF Results on PLT

Parameter	Minority ^{3}He, D	2nd Harmonic H	Minority H, D
I_p (kA)	500	350	500
P_{rf} (MW)	1.3	3.0	1.5
$< n_e > 10^{19}\ \mathrm{m}^{-3}$	3.2	3.8	4
ΔT_{io} (keV)	2.2	2.7	1.0
ΔT_{eo} (keV)	1.0	0.5	1.3
$n\Delta T_{io}/P_{rf}$	5.4	3.4	2.7
$n\Delta T_{io}/P_{rf}I_p$	1.08	1.13	0.68

Table 4.2

Heating Efficiencies of Large Tokamaks

Machine	R_o	a	B_t	I_p	$\frac{aR^2}{a^2R\kappa}$	$\frac{I_p}{a^2R\kappa}$	$\frac{I_pa}{a^2R\kappa}$
	(m)	(m)	(T)	(MA)	()	(MA/m^3)	(MA/m^2)
HESTER	2.0	0.37	7.0	1.2	5.4	4.38	1.62
TFTR(nom)	2.48	0.85	5.2	3.0	2.9	1.68	1.98
TFTR/NB	3.1	0.55	4.2	2.5	5.6	2.7	1.49
JET	3.0	0.95	4.5	2.7	2.0	0.62	0.78
JT-60	3.0	0.95	4.5	2.7	3.16	1.0	0.95
Big Dee	1.67	0.67	2.2	3.5	1.47	2.35	1.57
Tore Supra	2.25	0.7	4.5	1.7	3.2	1.54	1.08
PLT	1.43	0.42	2.8	0.5	3.4	1.98	0.85

4.2 A High $\epsilon\beta_p$ Experiment, using ICRF Heating

The high beta experiments on HESTER are similar in nature to the high temperature ion heating experiments and may be included in the same set of experiments. The possible high beta experiment described here is distinguished from the ion heating experiment by including both the ICRF heating power described above and the lower hybrid heating described below. The definition of a high beta experiment is still even less precise than that of a new current drive experiment, because of the lack of any generally agreed upon model of pressure enhanced transport. HESTER, being a high aspect ratio machine, should certainly not challenge the Doublet III world record for plasma beta, but it can theoretically achieve higher pressures than ISX-B, Doublet III or PDX, because of its higher field, as shown in Figure 4.3. However, HESTER is designed to enter the regime where $0.5 < \epsilon\beta_p < 1.0$, if pressure enhanced transport is not too severe. The high aspect ratio of HESTER further extends our knowledge of the aspect ratio dependence of enhanced transport. The dual presence of a strong ion heating source and a strong electron heating source (current drive) should also prove to be a powerful tool in the separation of electron temperature vs. density effects in pressure enhanced transport.

Although high pressure should certainly be achieved in HESTER, toroidal beta limits are not predicted to be achievable with the allocated auxiliary power supplies. The trade-off is a familiar one to high beta experimenters. Within any given machine, if confinement is a nearly linear function of current, doubling the toroidal field halves beta, but doubles the achievable pressure for a fixed external heating source. The ICRF heating experiments must be done at relatively high field (> 6 T), while the lower hybrid heating range, while much broader band, has only partial penetration to the plasma center below 7 T. Thus, because of the high field needed for heating with existing rf supplies, the ultimate machine pressure limits will not be reached unless transport is highly favorable. The silver lining is that other machine missions should not be endangered by pressure enhanced transport.

The poloidal field system is designed to permit low q ($q < 2$) operation at design toroidal field. This permits the plasma to reach the theoretical balloon-mode limits [TO79], based on relatively flat density profiles and a temperature profile, represented by,

$$T(r) = T_o(1 - r^2/a^2)^{3/2}$$

typical of observed temperature profiles in beam heated discharges. This limit has been expressed by the simple correlation,

$$\beta_{crit} = \frac{0.2a}{Rq_*}\frac{1+\kappa^2}{2}$$

which is also similar in form to the simple Shafranov equilibrium limit on beta. For a 40 cm by 210 cm circular plasma with $q_* = 2$, the critical beta would be limited to 1.9 %. If heating is done at 7 T, this corresponds to an average plasma pressure of about 3 $\frac{1}{2}$ atmospheres.

The parameters of the highest pressure discharges achievable in HESTER are shown in Figure 4.2. The central temperatures achievable with combined lower hybrid and ion cyclotron heating are superimposed upon those achievable with ion cyclotron heating only. Heating by combined mechanisms is hard to interpret and may be useful primarily to set performance benchmarks. However, it may also be necessary to include lower hybrid electron heating at low density to establish a sufficiently warm plasma to allow adequate absorption of second harmonic ion cyclotron resonance waves. The addition of 4.8 MW of lower hybrid electron heating raises the electron and ion densities by over 50 % at high densities, as expected. The effect on ion temperature is small at low densities, but nearly doubles the electron temperature at the lowest densities. The peak electron temperature is 7.5 keV at a central ion density of 10^{20}, which is marginally adequate to perform a broad range of current drive experiments, using alternative current drive mechanisms, as discussed in section 6. The ion temperature begins to saturate at low densities, because of the inclusion of INTOR ripple trapping and plateau scaling [IN82] in the TOKSYC transport models.

The achievable pressure does not vary strongly with temperature and the highest pressure discharge shown is at the high density end with a central ion density of 4.0×10^{20} (m^{-3}). The volume averaged toroidal beta of the plasma is 1.1 %, the central beta is 3.0 %, and the volume average of $\epsilon\beta_p$ is 0.28. This value is somewhat below the the highest values of 0.28 in the high beta experiments on ISX-B, PDX, and Doublet III [CO82] [GO82] [HA82] [SW81]. Thus, in order to test pressure limits of the HESTER plasmas at high field, it will be necessary to heat in a mode in which transport is not significantly degraded.

The value of 4.0×10^{20} (m^{-3}) in the highest beta discharge is nearly three times the empirical limit predicted for the ohmic experiment in Chapter 3. Neutral injection experiments have so far shown that the ohmic density limit no longer applies during intense auxiliary heating. Equipe TFR [EQ80] has suggested that the achievable central plasma pressure (eV-m^{-3}) scales as

$$p_o = 9 \times 10^{22} \epsilon q_{lim}^{1/4} B_t^2 \frac{\sqrt{1 + \frac{P_{heat} + P_{dIdrive}}{P_{ohm}}}}{\sqrt{A}}$$

where A is the effective atomic mass units of the fuel (). This relation predicts that the above experiment would have the sum of the central electron and ion temperatures limited to 37 keV, giving a safety margin of 5.0 over the design values of $T_{eo} =$ 3.8 keV and $T_{io} =$ 3.7 keV . The safety margin vs. a simple-minded Shafranov equilibrium limit is $1/\epsilon\beta_p = 3.5$. The purpose of calculating these simple global safety margins is not to imply that the actual high pressure transport is known. The high pressure experiments on HESTER are not intended to reach world record or reactor relevant values of either toroidal beta or thermal pressure, but to extend the understanding of pressure effects on energy transport in a tokamak at an extreme value of aspect ratio and magnetic field over a broad range of densities and temperatures. The calculation of simple global safety margins, then, is a check that there is not some obvious limiting mechanism that prevents an interesting experiment.

References

[CO82] A. Colleraine et al, "Preliminary neutral injection experiments on Doublet III," no reference

[EQ80] Equipe TFR, "Tokamak scaling laws, with special emphasis on TFR experimental results," Nuclear Fusion, Vol. 20, No. 10, 1980

[GO82] R. Goldston et al, "Confinement studies with neutral beam injection on PDX and PLT," Third Joint Varenna-Grenoble International Symposium on Heating in Toroidal Plasmas, 1982

[HA82] R.J. Hawryluk et al, "Heating efficiency of high power perpendicular neutral beam injection in PDX," Princeton Plasma Physics Laboratory Report PPPL-1982, March 1982

[SW81] D.W. Swain et al, "High-beta injection experiments on the ISX-B tokamak," Nuc Fus, Vol. 21, No. 11, 1981

[TO79] A.M. Todd et al, Nuc Fus, Vol. 19, p. 743, 1979

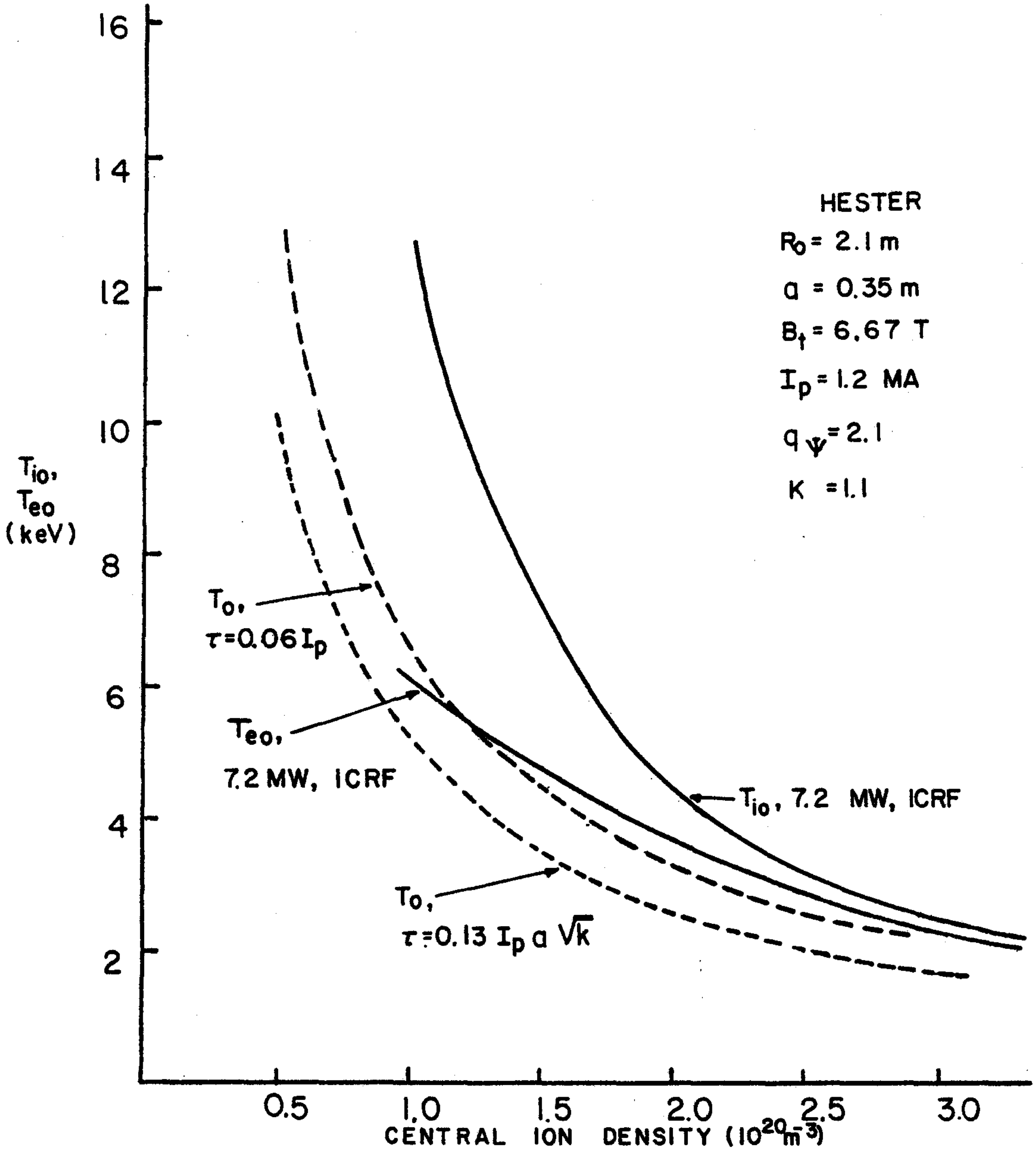

FIGURE 4.1

CENTRAL TEMPERATURES VS. POWER AND DENSITY, ACCORDING TO TOKSYC.

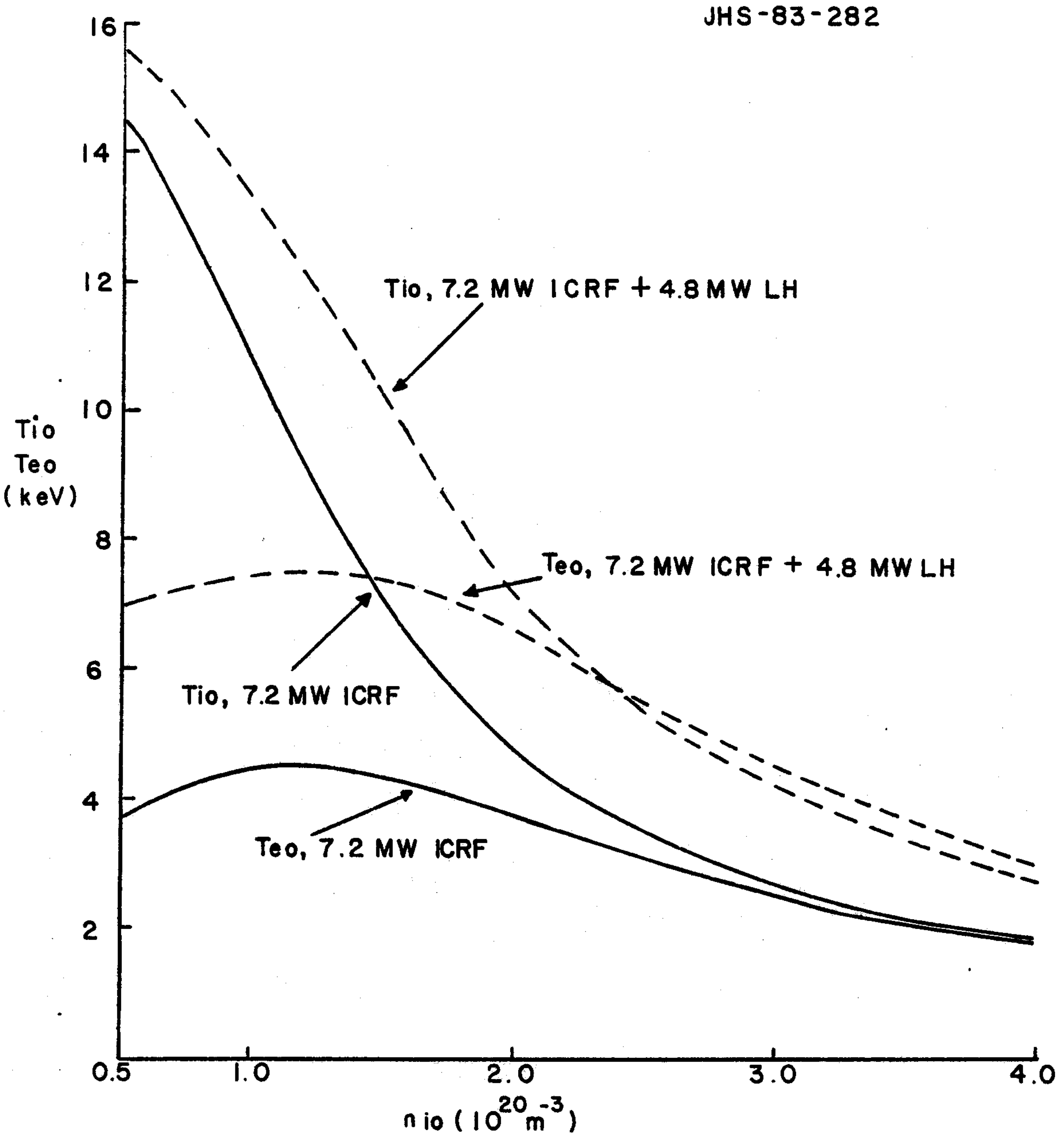

FIGURE 4.2

CENTRAL ION AND ELECTRON TEMPERATURE VS. CENTRAL ION DENSITY FOR 5.0 MW LOWER HYBRID AND 7.2 MW ICRF HEATING

JHS-83-2101

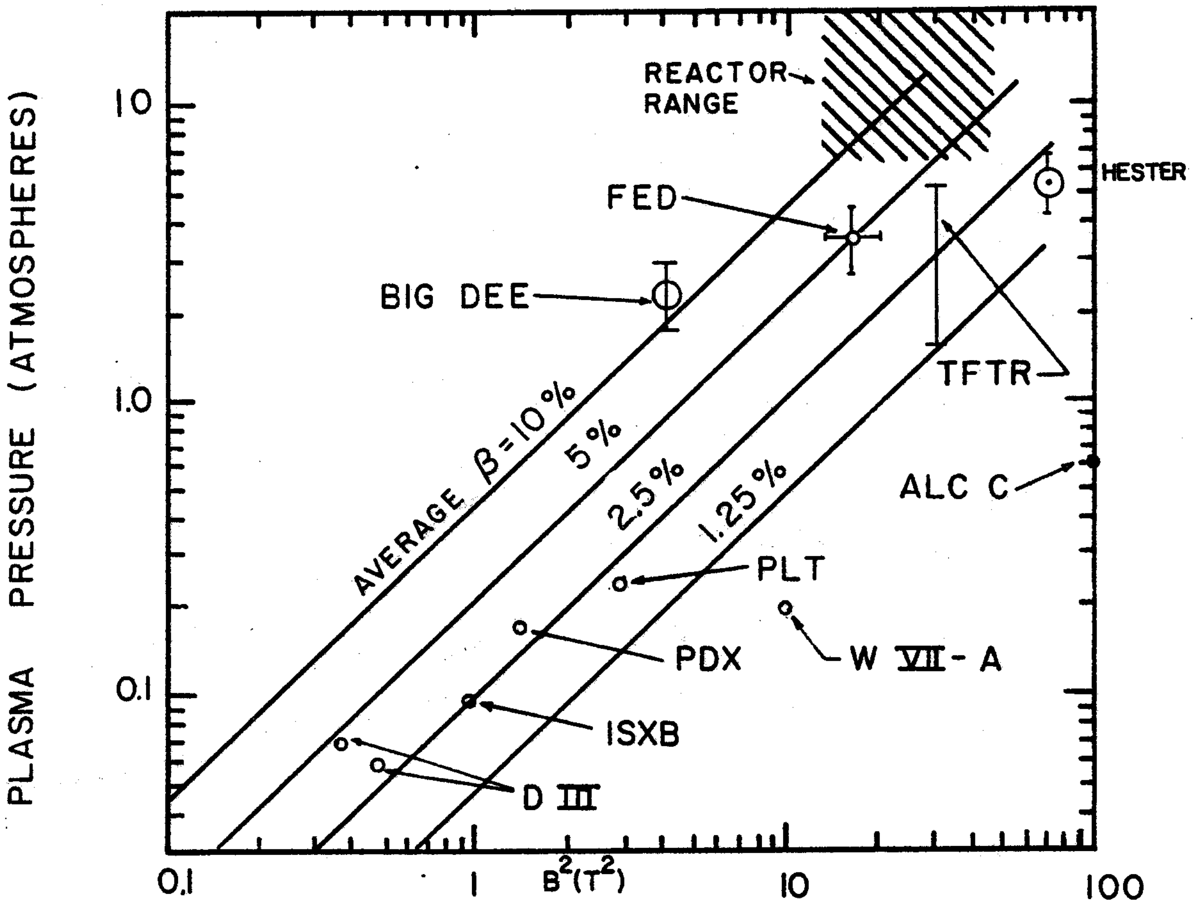

FIGURE 4.3

PRESSURE LIMITS OF MAJOR TOKAMAKS (CONRTESY OF PRINCETON PLASMA PHYSICS LABORATORY)

5.0 Lower Hybrid Electron Heating Experiments

The perception of the role of lower hybrid has changed dramatically in the past few years. The use of the lower hybrid resonance to heat ions has not met with dramatic success and is not now considered to be the best use of auxiliary power in this frequency range. By contrast, current drive and electron heating have been far more successful. In fact, the heating of bulk electrons by the tail electrons created by current drive may be the most efficient electron heating mechanism. This change in perception has led to what hopefully will be a short-lived historical anomaly, that the heating and current drive mechanisms are referred to as lower hybrid current drive and electron heating, although they are unrelated to the lower hybrid resonance. Thus, for want of any other term that can be recognized by the community, we will refer below to lower hybrid current drive and heating, fearing only that we will contribute further to the perpetuation of another term as meaningless as "Elmo."

5.1 The Lower Hybrid Electron Heating Experiment

Lower hybrid electron heating has never been the leading contender for plasma heating in tokamak reactors. High plasma temperatures have not yet been obtained using lower hybrid heating. ICRF and neutral beam heating have the ability to heat ions directly, which allows the possibility of putting less overall energy into the plasma for a given ion temperature requirement for controlled fusion. However, lower hybrid electron heating appears to have three important advantages, which are increasing interest in this mechanism. Unlike neutral beams, which are limited to a narrow range of densities for a given size plasma, and ICRF, which is limited to a narrow range of fields, lower hybrid electron heating through electron Landau damping can operate over a broad range of fields and densities. This is particularly important in an experimental device which may not achieve its predicted values of density or field. There is also preliminary evidence that electron heating does not degrade global energy confinement as ion heating does [UE82A], and that there may be fundamental reasons for this observation [UE82B]. Finally, electron Landau damping is also a current drive mechanism, allowing the same rf equipment to be used flexibly for current drive and heating. If different mechanisms are used, such as lower hybrid and compressional Alfven wave current drive, the higher electron temperatures due to lower hybrid heating directly increase the efficiency, and thus the reactor recirculating power, of the compressional Alfven heating.

An important motivation for the electron heating experiments on HESTER is to achieve temperatures in the range of 5-10 keV, so that the accessibility of the lower hybrid wave at higher temperatures can be tested, and so that a sufficiently hot plasma can be created to permit the testing of alternative current drive mechanisms, all of which are strongly dependent on electron temperature, as discussed in chapter 7.

5.1.1 Background

Lower hybrid electron heating has been achieved on PLT, Alcator C, WEGA, WT-2, JFT-2 and Versator, where current drive is counted as a form of electron heating. JFT-2 increased electron temperature by over 300 eV to 800 eV in a plasma with 200 kW of injected power with a frequency 1.7 times higher than the central lower hybrid frequency in a plasma with a line averaged electron density of 10^{19} m^{-3}. [UE82A]. Alcator C raised a 1.7 keV electron temperature to 2.0 keV at line average densities of 1-2 $\times 10^{20} m^{-3}$ with 100 kW of injection into a deuterium plasma [PO82]. To date, there are no published results of an experiment labeled "lower hybrid electron heating" which has a coupled rf power significantly larger than ohmic power into the plasma. This situation will hopefully change dramatically when the 2 MW (1.2 MW into the plasma) lower hybrid experiment on Alcator C is fully operational. However, the lower hybrid current drive experiments on Alcator C and PLT are the more definitive examples of the Landau damping heating mechanism, since the rf wave was the sole source of both electron energy and net momentum in both of these experiments.

5.1.2 Heating Effectiveness

General considerations of heating efficiency in HESTER were discussed in chapter 4. In this chapter we examine the implications of two assumptions: the first is the assumption that transport coefficients will be identical to those assumed for ion heating in chapter 4, in particular that electron confinement is degraded by a factor of two from its ohmic value, while the second assumes that electron heating is free from the degradation of confinement observed during ion heating. The results of these assumptions for 4.8 MW absorbed by the plasma, corresponding to 8 MW klystron output as explained in chapter 9, and 0.9 fractional power going to electrons, are shown in Figure 5.1. With the assumption that electron confinement is degraded by a factor of two during heating, our model predicts that a central electron temperature of 5 keV would be achieved at central ion densities lower than 7 $\times 10^{19}$ m^{-3}. This performance would be adequate for a definitive demonstration of bulk electron heating by electron Landau damping, would be marginal as a tool to study wave penetratation at high electron temperature, and would be marginally adequate to achieve flat-top using compressional Alfven heating, as discussed in the next chapter. If it is true that confinement is not degraded from ohmic during electron heating, the model predicts that an electron temperature of 5 keV can be achieved at a central ion density as high as 2×10^{20} m^{-3} and that 9 keV could be achieved at 7×10^{19} m^{-3}. At lower densities, the density scaling of the electron channel becomes totally dominant and electron temperature appears to saturate below 10 keV. With the improved scaling, accessibility and compressional Alfven heating could be studied, while fast wave transit time pumping current drive might possibly be studied. As stated previously, the backup method to achieve machine goals, if confinement is worse than expected is to acquire adequate high voltage power supplies to operate the ICRF and lower hybrid rf supplies simultaneously. This mode of operation is discussed in more detail in the section on pressure limit experiments.

References

[GO82] C. Gormezano et al, "Lower hybrid heating in the WEGA tokamak," Proc 3rd Joint Varenna-Grenoble Internatl Symp on heating in toroidal plasmas, EUR 7979 EN, March 1982

[PO82] M. Porkolab, J.J. Schuss et al, "Lower hybrid heating experiments on the Alcator C and the Versator II tokamaks," Proc 3rd Joint Varenna-Grenoble Internatl Symp on heating in toroidal plasmas, EUR 7979 EN, March 1982

[TA82] S. Tanaka, "Toroidal current drive and sustainment by lower hybrid waves in the WT-2 tokamak," Proc 3rd Joint Varenna-Grenoble Internatl Symp on heating in toroidal plasmas, EUR 7979 EN, March 1982

[TO82] G. Tonon et al, "Lower hybrid current drive with suprathermal electrons in the WEGA experiment," Proc 3rd Joint Varenna-Grenoble Internatl Symp on heating in toroidal plasmas, EUR 7979 EN, March 1982

[UE82A] K. Uehara and T. Nagashima, "Lower hybrid heating experiment in JFT-2 tokamak," Proc 3rd Joint Varenna-Grenoble Internatl Symp on heating in toroidal plasmas, EUR 7979 EN, March 1982

[UE82B] K. Uehara and K. Fujita, JAERI-M 82-023, 1982

JHS- 83-281

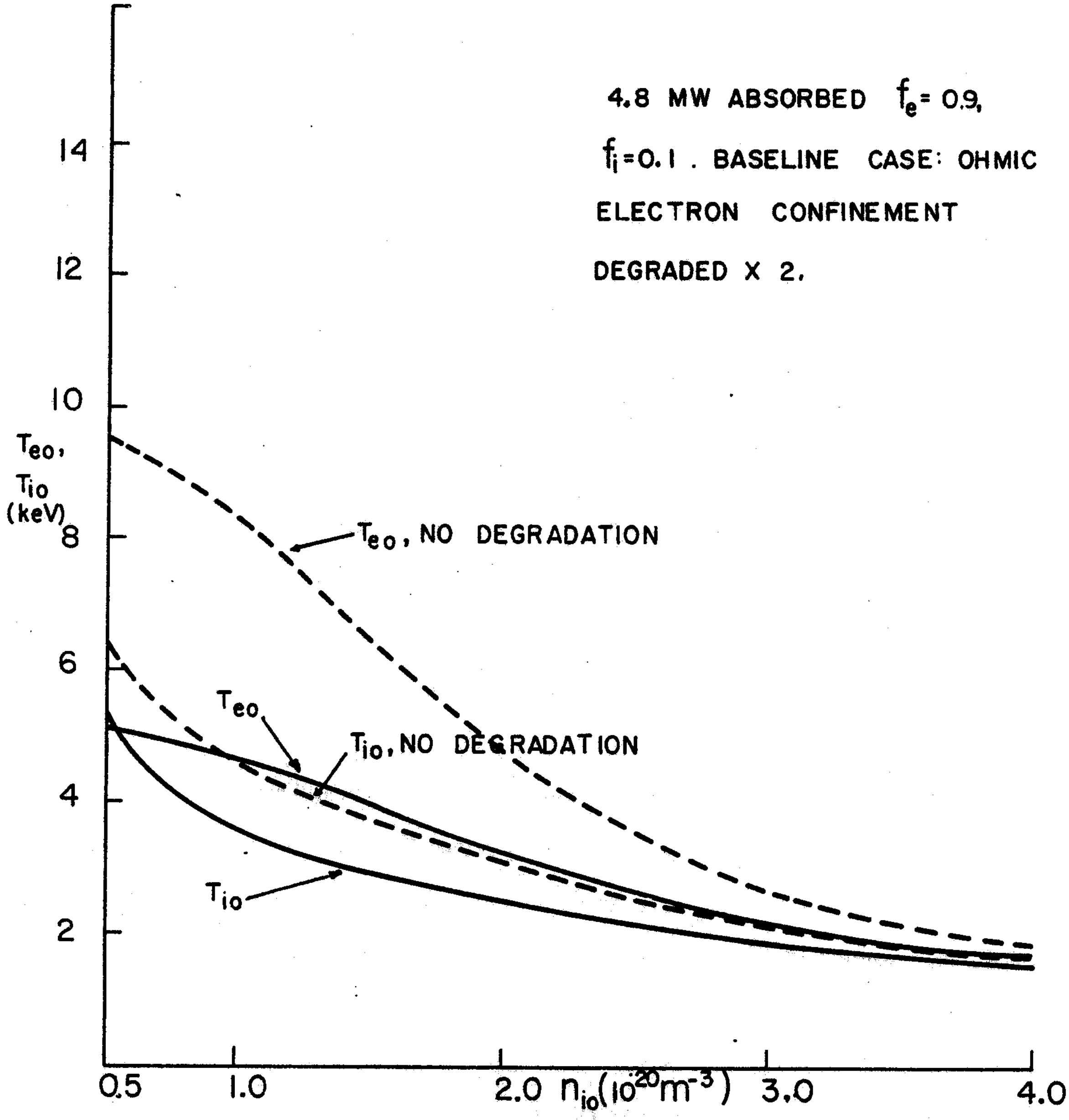

FIGURE 5.1

CENTRAL ION AND ELECTRON TEMPERATURE VS. CENTRAL ION DENSITY FOR 4.8 MW ELECTRON HEATING.

6.0 The Lower Hybrid Current Drive Experiments

The lower hybrid current drive experiments on HESTER extend the results on PLT and Alcator C to more reactor relevant regimes. The physics interest will be primarily in the regimes of achieving low safety factor at high electron density, with either an original or upgraded current drive capability to drive the plasma to a safety factor of < 2 at central electron densities of 10^{20}. Two experiments of interest, not expected to be duplicated on PLT or Alcator C, will be to drive current below a limiter safety factor of 2.0 at an electron density between 5.0×10^{19} and 10^{20}, and to drive current to low safety factor at electron temperatures above 5 keV. A possible upgrade of high voltage power supplies would allow an upgrade experiment with simultaneous current drive at the abovementioned density and safety factor and ion cyclotron resonance heating with ion and electron temperatures above 10 keV.

6.1 Background

Steady-state current drive has been long been recognized as a desirable technique for combining the good energy confinement of the tokamak with the steady-state capability of other magnetic confinement concepts [FI78] [PR79] [YU79] [BA80].

6.2 Description of a Possible Lower Hybrid Current Drive Discharge

A model of a possible lower hybrid current drive discharge is described below to illustrate HESTER's capability. 4.8 MW of microwave power is injected into a plasma with a line-average electron density of 1.05 $\times 10^{20}$, heating the plasma to a central electron temperature of 6.0 keV and a central ion temperature of 3.5 keV , assuming that all of the power coupled to the plasma goes directly to the electrons. The efficiency of coupling to the plasma is assumed to be 80 % , based on claimed coupling efficiencies on PLT [ST82].

One of the first things to notice is the predicted efficiency of lower hybrid current as an electron heater. The central electron temperature is higher than that of any heated tokamak plasmas to date. The high coupling bandwidth of travelling fast wave energy to electrons is undoubtedly the most attractive feature of lower hybrid current drive. Recent experiments at M.I.T. succeeded in coupling significant power into the plasma over a range of central flux densities from 4 to 11 T [PO82]. If this degree of flexibility persists into the reactor regime, there would be little reason to consider less flexible and more expensive electron cyclotron resonance heating for either bulk heating or current drive.

Penetration of the lower hybrid wave to the center of the plasma should occur if the wave is neither absorbed by the fast ion mode or reflected by conversion to the whistler mode. Using the interpretation in Yuen's reactor study [YU79], a critical frequency for fast wave cutoff (radians/s) is calculated by:

$$\omega_c = \sqrt{\left(\sqrt{1 + 4\,\frac{\Omega_{ce}^2}{\omega_{pe}^2}} - 1\right)\omega_{pe}^2\,\frac{\Omega_{ci}}{2\,\Omega_{ce}}} \tag{6.1}$$

The lower refractive index cutoff, is then calculated by:

If $\omega_I \leq \omega_c$,

$$n_{LC} = \sqrt{\frac{1}{1 - \frac{\omega^2}{\Omega_{ce}\Omega_{ci}}}} \tag{6.2}$$

If $\omega_I > \omega_c$,

$$n_{LC} = \frac{\omega_{pe}}{\Omega_{ce}} + \sqrt{1 + \left(\frac{\omega_{pe}}{\Omega_{ce}}\right)^2\left(1 - \frac{\Omega_{ce}\Omega_{ci}}{\omega^2}\right)} \tag{6.3}$$

where ω_I is the current drive launching frequency (radians/s). In this case, the critical frequency at the plasma center is 34.0 Grad/s and the launching frequency is 28.9 Grad/s , so the lower cutoff due to reflection of a whistler mode wave is 1.48 .

The upper cutoff set by conversion of the wave to a hot ion mode, followed by strong absorption is calculated by:

$$n_{UC} = \left(0.5\,\frac{c}{v_{Te}}\right)\left(\frac{\omega_I^2}{\omega_{pi}^2} + \frac{\omega_I^2}{\Omega_{ce}\,\Omega_{ci}} - 1\right) \tag{6.4}$$

$$n_{UC} = n_{UC}\left(\left(1.5\,\frac{T_e}{T_i}\right) + 0.375\left(\frac{\omega_I^2}{\Omega_{ce}\,\Omega_{ci}}\right)^2\right)^{-0.5} \tag{6.5}$$

where v_{Te}, the thermal electron velocity (m/s), is $\sqrt{2T_e/m_e}$. The upper cutoff index of refraction at the plasma center is then 4.0 . The accessibility window, then, is believed to be compatible with the wave spectra launched by PLT and Alcator C, and should be even more compatible with that of HESTER, because of its higher number of parallel waveguides in a grill. PLT is believed to have most of its launched spectrum concentrated between $n_{z\|1} = 1.5$ and $n_{z\|2} = 3.0$ [HO82], while Alcator C may have most of its launched spectrum between $n_{z\|1} = 1.0$ and $n_{z\|2} = 2.5$ [PO82]. Since there are 16 waveguides per grill in HESTER, as contrasted with 4 in Alcator C, the bandwidth of the launched spectrum should be twice as narrow, and the ability of the waves to fit within the accessibility window correspondingly better. The possibility of having adequate wave access at 4.6 GHz should allow significant economies in the microwave equipment for HESTER, as discussed in section 10. However, the selection of 4.6 GHz launching, which is very close to $\sqrt{\Omega_{ci}\Omega_{ce}}$ at the plasma center, may be contraindicated by further understanding of the Alcator C experiments, in particular, the finding that current drive efficiency is 50% higher at 10 T than at 8 T in Alcator C. The mechanism for this efficiency loss has not yet been adequately elucidated. If the lower efficiency at lower field is due primarily to a lower electron tail population at lower temperature, then the efficiency of current drive in HESTER will not be degraded by operation at 7 T. If the fundamental cause is partial inaccessibility of the wave spectrum, this may lead to the selection of a lower launching frequency on HESTER, despite the loss of credits from existing equipment. Since the equipment for Alcator C provides about half the needs of the HESTER current drive experiment, it would clearly be less expensive to operate at a lower frequency if the efficiency is double that at 4.6 GHz. The physics interest and reactor relevance, of course, would be greatest at whatever frequency gives the highest efficiency, but this cannot be predicted at present.

One simple-minded approach to the selection of power requirements for a new experiment is to scale from the best known performance of PLT or Alcator C, assuming that the power requirements scale linearly with electron density and major radius for a given current. The best case performance predicted by scaling from performance on PLT and Alcator C is somewhat worse than the performance predicted in reactor studies [YU79] [BA80]. This does not imply that the collisional theory predicting power requirements for current drive is incorrect. The reactor-grade plasmas were fed by larger waveguide arrays than the 6 waveguide grill on PLT or the 4 waveguide grill of Alcator C, and thus focussed a higher fraction of the wave energy into the desired band of wave velocities. In addition, each reactor study proposing lower hybrid current drive has also proposed at least one clever idea, in order to reduce the recirculating power to attractive levels. In STARFIRE, the idea was the use of edge currents [BA80], in the current-driven M.I.T. HFCTR [YU79], Kaplan proposed operating the reactor in the hot ion mode. More recently, Fisch [FI82] has proposed modulating the plasma density and/or effective impurity level in order to reduce the recirculating power. None of these ideas have been observed yet in present-day experiments. HESTER should be able to create a plasma with sufficiently hot and dense electrons to allow skin current formation and may be able to determine the desirability or undesirability of hollow current profiles in current driven plasmas. The hot ion mode is of no particular relevance in the absence of fusile fuel and will not be simulated in HESTER . The use of density fluctuation to decrease recirculating power can be easily tested in HESTER , using pellet injection. HESTER is particularly well suited to this last concept, because the high aspect ratio decreases the pulsed torques from swinging the equilibrium field in response to pressure changes and the restriction of HESTER 's current drive experiments to nonfusile fuel greatly decreases wall loading excursions and thermal stresses due to the density modulation.

Scaling from the best performance discharges of PLT and Alcator C, one would expect power requirements of

$$P_d = K\, I_p n_e R_o \tag{6.6}$$

where n_e is the line-average electron density (10^{20} m^{-3}) and K is 9.6, 12.0, and 8.2 for PLT, Alcator C at 8 T and Alcator C at 10 T, respectively. The best of the best, Alcator C at 10 T, was chosen for the purpose of design performance prediction, on the grounds that HESTER will have more waveguides in a grill than either Alcator C or PLT and that its design may benefit from the improved understanding of current drive expected from the ongoing experimental and theoretical program. Balanced against the optimistic considerations is that HESTER will not be able to achieve 10 T, with the corresponding possibility that the available 4.6 GHz supplies are suboptimal for current drive in any 7 T plasma. An important decision on the upgrade of the lower hybrid system to twice its present power will have to be made, whether to attempt to optimize efficiency by selecting a different frequency or to minimize cost by duplicating the existing launching system. The assumption of Alcator C efficiency at 10 T leads to the prediction that 4.8 MW is required for $q_{lim} = 2.1$ with a central electron density of 6.0 keV (eV). This power requirement is twice the power available for Alcator C experiments and also constitutes the most significant electron heating experiment scheduled for the tokamak program.

Adding one further level of sophistication, PLT suggests a scaling law for the current density/ power density ratio (A-m/W) [ST82], of a form first suggested by the STARFIRE study [BA80] of:

$$J_{overPdPLT} = \left(\frac{12.6 \times 10^{20}}{n_e}\right) \frac{n_{z2}^{-2} - n_{z1}^{-2}}{\ln(\frac{n_{z1}}{n_{z2}})} \tag{6.7}$$

Since the approximate limits of the index of refraction are 1.5-3.0 for PLT and 1.0-2.5 for Alcator C, the function of parallel index is almost twice as good for Alcator C as for PLT. This would suggest that even the best discharges on Alcator C fall below the PLT scaling law [ST82] in equation 6.7. However, since the fraction of the total launched power that actually couples to resonant electrons is unknown in either case, a true comparison cannot yet be made. HESTER should be able place most of its launched power spectrum between $n_{||}$ = 1.5 to 1.7 and test more fully the degree to which current drive efficiency can be improved by control of the launched wave spectrum

Using Alcator C scaling at 10 T and the transport simulation on TOKSYC, described above in chapter 4, the flattop experiments on HESTER, using lower hybrid current drive, are predicted in Figure 6.1. At high density, current drive is shown to collapse due to the lower sustainable current, accompanied by deteriorating ion confinement. If adequate cleanliness can be maintained in the plasma, high temperature and current should be achievable at central densities between 0.5-1.0 $\times 10^{20}$ m^{-3}.

Acknowledgments

We would like to thank N.J. Fisch and J.J. Schuss for helpful discussions.

References

[BA80] C.C. Baker et al, "STARFIRE - A commercial tokamak fusion power plant study," Argonne National Laboratory, ANL/FPP-80-1, 1980

[FI78] N.J. Fisch and A. Bers, Proc Third Topical Conf RF Plasma Heating, Pasadena, 1978

[HO82] W.M. Hooke et al, "Lower hybrid heating and current drive," IAEA-CN-41, 9th Internatl Conf Plas Phys and Controlled Nuclear Fusion Research, Baltimore, MD, Sept 1982

[PO82] M. Porkolab et al, "Lower hybrid heating and current drive experiments on the Alcator C and Versator II tokamaks," IAEA-CN-41, 9th Internatl Conf Plas Phys and Controlled Nuclear Fusion Research, Baltimore, MD, Sept 1982

[PR79] R. Prater, et al, General Atomic Report GA-A15229, 1978, GA-A15383, 1979

[PO82] M. Porkolab, J.J. Schuss et al, "Lower hybrid heating and current drive experiments on the Alcator C and Versator II Tokamaks," IAEA-CN-41, 9th Internatl Conf Plas Phys and Controlled Nuclear Fusion Res, Baltimore, MD, Sept 1982

[ST82] J.E. Stevens et al, "Lower Hybrid Heating and Current Drive on PLT," Third Varenna-Grenoble International Symp on Heating in Toroidal Plasmas, Mar 1982

S. Tanaka et al, "Plasma current drive and sustainment by lower hybrid wave in the WT-2 tokamak," IAEA-CN-41, 9th Internatl Conf Plas Phys and Controlled Nuclear Fusion Research, Baltimore, MD, Sept 1982

[YU79] S.Y. Yuen, J.H. Schultz, D.Kaplan and D. Cohn, "Design Features of Tokamak Power Reactors with RF-Driven Steady State Current," M.I.T. Plasma Fusion Center Report RR-79-2 Nov 1979

JHS-83-291

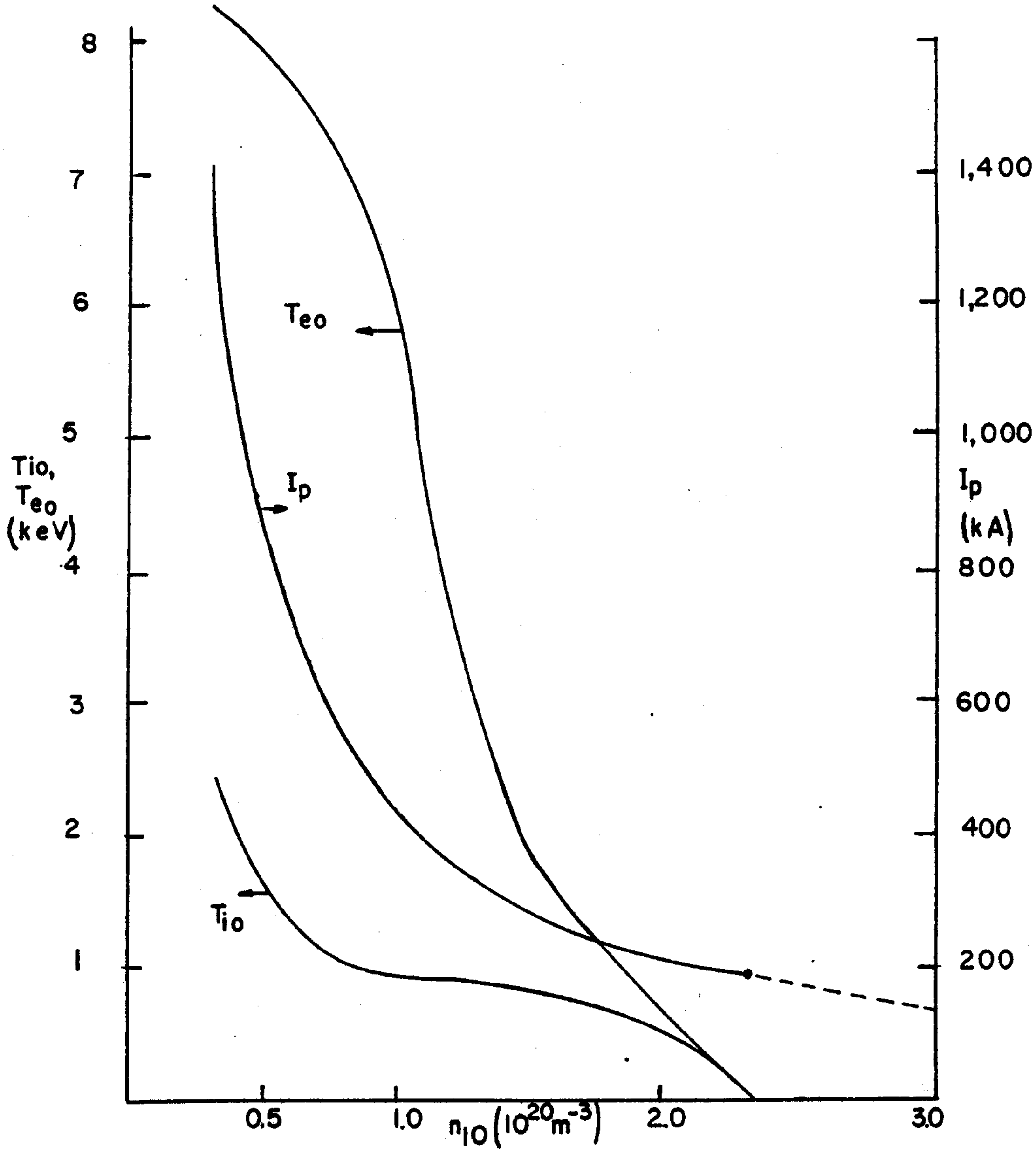

FIGURE 6.1

PLASMA CURRENT AND ELECTRON AND ION CENTRAL TEMPERATURES VS. CENTRAL ION DENSITY FOR LOWER HYBRID FLATTOP CURRENT DRIVE AT 4.8 MW.

7. Alternative Current Drive Experiments

7.0 Low Frequency Current Drive Experiments

Low frequency rf current drive mechanisms are attractive as possible reactor current drive mechanisms, because low frequency rf technology is relatively inexpensive, wave penetration to the plasma center is less difficult than for lower hybrid waves and higher theoretical efficiencies than those of lower hybrid are possible, according to the analysis of Fisch and Karney [FI81]. We consider three variations on this form of current drive for HESTER : slow wave below the first harmonic ion cyclotron frequency, slow wave between the first and second harmonic, and fast wave between the first and second harmonic.

As will be seen below, it is not practical to do a definitive test of these low frequency current drive mechanisms in a tokamak that is not capable of achieving high electron temperature and a pulse longer than magnetic diffusion times at high temperature. The HESTER experiments are well suited to be tests of these mechanisms, because HESTER is large enough to accommodate the ports needed for combined current drive and heating, but small enough not to require the large currents and power needed for similar experiments on larger, planned tokamaks. The lack of magnet derating with pulse time also allows the long pulses at peak performance needed for these experiments. A special effort will be made to use existing rf sources for these experiments, as will be discussed below.

7.1 Compressional Alfven Current Drive

Low parallel phase velocity waves were first suggested by Wort as an attractive method of current drive, because of their high momentum to energy ratio [WO71]. The compressional Alfven wave is a particular case of these low frequency waves. Motivation for interest in this case as a reactor concept was created by the analysis of Fisch and Karney [FI81], predicting a normalized J/P_d of

$$\frac{J}{P_d} = \frac{13}{w_a} + 1.4w_a^2 + 5 \tag{7.1}$$

for compressional Alfven waves, where w_a is the average ratio of plateau electron parallel velocity to electron thermal velocity. If w_a can be lower than 0.5, J/P_d ratios of 40 or higher are conceivable, representing at least double the expected efficiency of lower hybrid current drive. The actual efficiency of current drive/power efficiency, as defined by Fisch [FI81] is then:

$$\frac{I}{P_d} = 0.02\frac{T_{e10}\frac{J}{P_{d,norm}}}{R_o n_{e20}} = 0.1A/W \tag{7.2}$$

where T_{e10} is the central electron temperature, normalized to 10 keV and n_{e20} is the central electron density, normalized to $10^{20}m^{-3}$.

7.1.A Low frequency compressional Alfven wave current drive

It has been assumed that slow wave current drive must also be low frequency, in particular lower than half the ion cyclotron harmonic frequency, in order to avoid any cyclotron heating of the ions [FI81]. However, as discussed below, fast wave transit time current drive contemplates using a frequency between the first and second ion cyclotron harmonics, and, as is well known, heating of majority species at their fundamental frequency has not demonstrated strong damping. Therefore, we will also consider a high frequency compressional Alfven wave, intermediate between the first and second harmonic frequencies, as well as the low frequency, slow wave proposed by Fisch and Karney [FI81].

Tables 7.1 and 7.2 show the predicted current drive efficiencies for the pessimistic and optimistic bounds of a central electron temperature of 2 keV and 10 keV, respectively at a density of 10^{20} m^{-3}. As shown in Table 7.1, a low frequency, slow wave experiment might select a launching frequency of 39 MHz. This low a frequency could be provided by the triodes already available at M.I.T., but the delivery system would have to be altered. The two most expensive alterations would be to the resonant cavities at the tube outputs and the construction of new antennae. A manufacturer's estimate places the cost of modification of the output cavities at $200 K/ tube, or $1.2 M for a six tube experiment. This cost would be avoided by the high frequency, slow wave experiment described in the next section.

The experiment described in Table 7.2 assumes a central electron temperature of 10 keV at a central electron density of 10^{20}. If these parameters can be achieved, the theoretical current generation efficiency, according to equation 7.2, is 0.316 A/W. Thus, the baseline experiment would require 1.58 MW of ICRF power. A full ohmic current of 1.2 MA would require 3.8 MW. In neither case could the current drive provide adequate power to achieve the desired electron temperature and another auxiliary power source would be required. A curious feature can immediately be observed, which is true for all of the lower frequency current drive mechanisms. Since they all have a favorable dependence on electron temperature and higher theoretical efficiency than lower hybrid current drive, and since auxiliary heating power is simply the difference between current drive power and total plasma losses, which decrease with total current, the higher the current, the less total auxiliary power is required. For the case of the HESTER design problem, the total auxiliary power is fixed both by achievable thermal wall loading and available power supplies. For this case, the Fisch-Karney theory predicts a regime in which current drive power actually decreases with flattop current, as shown in Figure 7.1. This regime can be identified with any combination of temperature and density in which global confinement improves faster than linearly with current, e.g. plasmas whose transport is dominated by ions in either the colllisional or banana regimes.

7.1.B High Frequency Compressional Alfven Wave Current Drive

At the base field on axis of 7 T, HESTER can drive current at 180 MHz, the bottom of the range that can be excited by existing ICRF supplies at M.I.T., but a frequency sufficiently low that the second harmonic frequency is moved out to the edge of a 35 cm plasma. The high frequency option forces a small spacing between wave excitation elements, not dissimilar from the spacing between lower hybrid wave guides. It is not immediately clear whether this is inferior or superior to the larger spacings associated with slow wave, low frequency or fast wave, high frequency current drives, the other two options considered in this chapter.

A possible high frequency, slow wave experiment is described by Tables 7.3 and 7.4 for the pessimistic and optimistic bounds of electron temperatures of 2 keV and 10 keV at a central electron density of $10^{20}\ \mathrm{m}^{-3}$. At a central electron temperature of 10 keV and a central electron density of 10^{20}, the predicted efficiency of the high frequency experiment, 0.4 A/W, is somewhat higher than that predicted for the low frequency experiment. Thus, a baseline 500 kW flattop discharge would require 1.25 MW, while a full ohmic current discharge of 1.2 MW would require 3 MW. As above, a significant amount of auxiliary heating power would be required, in addition to the current drive power.

The antenna spacing for the high frequency experiment is only 2.1 cm for quarter-wave spacing and a required toroidal mode number of 48. This suggests the possibility of launching by a wave guide or some other form of slow wave structure. The 18 cm port in HESTER could accommodate at least 2 full wave lengths. However, it is unclear whether a practical launching structure can be designed for the high frequency compressional Alfven wave.

7.3 Fast Wave Transit Time Magnetic Pumping Current Drive

Transit time magnetic pumping current drive involves accelerating electrons that are locked in phase with a travelling wave, such that the parallel electric field vanishes and

$$m\frac{dv_z}{dt} = -\mu\frac{\partial B_z}{\partial z}$$

where $\mu = mv_\perp^2/2B_o$ is the magnetic moment and the z-direction is parallel to the magnetic field.

Fast wave transit time magnetic pumping has been suggested by Perkins [PE82] as a practical current drive mechanism for high temperature, high beta plasmas, such as those of FED or INTOR. The attractive features of fast wave transit time magnetic pumping are high theoretical efficiency in the reactor relevant high beta, high temperature regime and the use of a frequency high enough to be clearly compatible with waveguide launching in a reactor. The principal disadvantage or key question concerning fast wave transit time pumping is that it is lightly damped, allowing competition from other absorption mechanisms, such as superthermal alpha particle heating.

It is theoretically more difficult to establish a flattop current in HESTER using fast wave transit time pumping than using slow wave compressional Alfven current drive. As can be seen in Table 7.5, the parameters needed for a reasonably efficient fast wave current drive are much more restrictive than those for slow wave current drive. The reasons for this are the limitations of dealing with tail electrons, instead of bulk electrons in the slow wave drive. The fast wave current density must be assumed to be electron tail population limited, as lower hybrid current density was perhaps incorrectly assumed to be limited. Since fast wave current density interacts directly with the hot electron tail without establishing any toroidal eigenmodes, it is high Q and thus must compete with other weak damping mechanisms.

The limitations on fast wave transit time magnetic pumping are defined in terms of its efficiency and its damping rate. If there are no competing wave absorption mechanisms, the efficiency of transit time magnetic pumping current drive, according to Fisch and Karney [FI80] is:

$$\frac{J}{P_{d,norm}} = \frac{13}{w_a} + 1.4w_a^2 + 5 = 22 \qquad (7.3)$$

where w_a is the average ratio of parallel wave to electron thermal velocity, and $\frac{J}{P_d}$ is the normalized current density/power density efficiency. The actual efficiency of current drive/power efficiency, as above, is then:

$$\frac{I}{P_d} = 0.02\frac{T_{e10}\frac{J}{P_{d,norm}}}{R_o n_{e20}} = 0.1A/W \qquad (7.4)$$

where T_{e10} is the central electron temperature, normalized to 10 keV and n_{e20} is the central electron density, normalized to $10^{20}m^{-3}$. As can be seen in Table 7.5, even if the ambitious, but reasonable, goal of a central electron temperature of 10 keV at a density of 10^{20} is achieved, it will still require at least 5 MA for 500 kA current. Since the 5 MA could be provided by already existing equipment, this is not a problem in itself, but it is clear that a flattop current experiment cannot be done with fast wave transit time pumping without the use of a substantial auxiliary power source, perhaps lower hybrid electron heating.

The damping of the fast wave, as described by Perkins [PE82], is a strong function of the central electron beta, β_{eo} and of the ratio of the

$$\epsilon = \frac{m_e c^2}{2\, n_{||}^2 k T_e} = 4.5$$

where $n_{||}$ is the parallel wave index of refraction and $k = 1.6 \times 10^{-19}\, J/eV$.

The wave absorption coefficient γ is:

$$\gamma = 0.25\omega\sqrt{\pi}\beta_e\sqrt{\epsilon}e^{-epsilon} = 384 \times 10^3$$

The characteristic radial attenuation length Δ, defined such that the attenuation per pass is $e^{-\Delta}$, is [PE82]:

$$\Delta = \frac{2\gamma^* a_{minor}}{v_A} = \pi^{3/2}(\frac{a}{\lambda_{||}})\sqrt{\frac{M}{m}}\beta_{eo}^{3/2}\epsilon e^{-\epsilon} = 0.036$$

where v_A is the Alfven velocity. Thus the number of passes for wave absorption is 28.

Since highly favorable transport is necessary for a successful flattop experiment, using fast wave transit time magnetic pumping, the planning of this experiment, in particular the design of the fast wave launching antennae, would have to follow the demonstration of favorable plasma confinement in HESTER, and thus represents a possible machine upgrade.

Acknowledgments

We would like to thank N.J. Fisch for helpful discussions.

References

[FI81] N.J. Fisch and C.F.F. Karney, "Current generation with low-frequency waves," Phys Flu 24 (1), Jan 1981

[FI82] N.J. Fisch, "Current generation by minority species heating," Nuc Fus, Vol. 21, No. 1, 1981

[PE82] F.W. Perkins, "Fast Wave Current Drive: Prospects for a Purely Steady-State FED," to be published

[WO71]. D.J.H. Wort, Plasma Phys, 13, 258, 1971

Table 7.1 Low Frequency Compressional Alfven Wave Current Drive Experiment

Minimum Performance Case: $T_{eo} = 2$ keV

Parameter	Description	Units
R_o	major radius	2.05 m
a	minor radius	30 cm
T_{eo}	central electron temperature	2 keV
n_{eo}	central electron density	10^{20} m^{-3}
B_t	toroidal flux density on axis	7.0 T
f	wave launching frequency	39 MHz
v_A	Alfven speed	1.53×10^7 m/s
v_{Te}	electron thermal velocity	1.88×10^7 m/s
$v_{\|}$	parallel wave velocity	2×10^7 m/s
w_a	ratio of parallel velocity to thermal velocity	1.07
l	poloidal mode number	1
n	toroidal mode number	8
k_z	toroidal wave number	12.3 m^{-1}
k_x	poloidal wave number	10.5 m^{-1}
λ_z	parallel wavelength	51.3 cm
$\delta z_{antenna}$	antenna spacing for quarter-wave spacing	12.8 m
$\frac{J}{P_d}$	normalized ratio of current density to power	18.7
$\frac{J}{P_d}$	current generation efficiency	0.037 A/W

Table 7.2 Low Frequency Compressional Alfven Wave Current Drive Experiment

Parameter	Description	Units
R_o	major radius	2.05 m
a	minor radius	30 cm
T_{eo}	central electron temperature	10 keV
n_{eo}	central electron density	10^{20} m^{-3}
B_t	toroidal flux density on axis	7.0 T
f	wave launching frequency	39 MHz
v_A	Alfven speed	1.53×10^7 m/s
v_{Te}	electron thermal velocity	4.2×10^7 m/s
$v_{\parallel}$	parallel wave velocity	2×10^7 m/s
w_a	ratio of parallel velocity to thermal velocity	0.48
l	poloidal mode number	1
n	toroidal mode number	8
k_z	toroidal wave number	12.3 m^{-1}
k_x	poloidal wave number	10.5 m^{-1}
λ_z	parallel wavelength	51.3 cm
$\delta z_{antenna}$	antenna spacing for quarter-wave spacing	12.8 m
$\frac{J}{P_d}$	normalized ratio of current density to power	32.4
$\frac{J}{P_d}$	current generation efficiency	0.316 A/W

Table 7.3 High Frequency Compressional Alfven Wave Current Drive Experiment

Minimum Performance Case: $T_{eo} = 2$ keV

Parameter	Description	Units
R_o	major radius	2.05 m
a	minor radius	30 cm
T_{eo}	central electron temperature	2 keV
n_{eo}	central electron density	10^{20} m^{-3}
B_t	toroidal flux density on axis	7.0 T
f	wave launching frequency	39 MHz
v_A	Alfven speed	1.53×10^7 m/s
v_{Te}	electron thermal velocity	1.88×10^7 m/s
$v_{\|\|}$	parallel wave velocity	1.5×10^7 m/s
w_a	ratio of parallel velocity to thermal velocity	0.815
n	toroidal mode number	7
k_z	toroidal wave number	74 m^{-1}
λ_z	parallel wavelength	8.5 cm
$\delta z_{antenna}$	antenna spacing for quarter-wave spacing	2.1 cm
$\frac{J}{P_d}$	normalized ratio of current density to power	21.9
$\frac{J}{P_d}$	current generation efficiency	0.043 A/W

Table 7.4

High Frequency, Slow Wave Compressional Alfven Wave Current Drive Experiment

Parameter	Description	Units
R_o	major radius	2.05 m
a	minor radius	30 cm
T_{eo}	central electron temperature	10 keV
n_{eo}	central electron density	10^{20} m^{-3}
B_t	toroidal flux density on axis	7.0 T
f	wave launching frequency	180 MHz
v_A	Alfven speed	1.53×10^7 m/s
v_{Te}	electron thermal velocity	4.3×10^7 m/s
$v_{\|}$	parallel wave velocity	1.53×10^7 m/s
w_a	ratio of parallel velocity to thermal velocity	0.36
n	toroidal mode number	48
k_z	toroidal wave number	74 m^{-1}
λ_z	parallel wavelength	8.5 cm
$\delta z_{antenna}$	antenna spacing for quarter-wave spacing	2.1 cm
$\frac{J}{P_d}$	normalized ratio of current density to power	40.8
$\frac{J}{P_d}$	current generation efficiency	0.4 A/W

Table 7.5 Fast Wave Transit Time Magnetic Pumping Current Drive Experiment

Parameter	Description	Units
R_o	major radius	2.1 m
a_{minor}	minor radius	40 cm
T_e	electron temperature	10 keV
B_t	toroidal flux density	5.5 (T)
f	launching frequency	220 MHz
β_e	central toroidal electron beta	2.66 %
v_{Te}	electron thermal velocity	41.9×10^6 m/s
$v_{\|}$	parallel phase velocity	126×10^6 m/s
v_A	Alfven velocity	8.56×10^6 m/s
w_a	ratio of parallel phase velocity to thermal velocity	3.000E+00
ϕ_{ant}	relative phase of adjacent launching elements	90 degrees
λ_{par}	parallel wavelength	0.57 m
$\delta_{z,ant}$	antenna element spacing	14.3 cm
$k_{\|}$	parallel wavenumber	11 m^{-1}
$k_{\perp}$	perpendicular wavenumber	160 m^{-1}
$n_{\|}$	parallel index of refraction	2.39
ϵ	ratio of inertial to resonant electron thermal energy	4.5
γ	wave absorption coefficient	384×10^3
Q	quality of the toroidal eigenmode	1800
Δ	attenuation per pass coefficient	0.0359
n_{passes}	number of passes for wave absorption	28
J_{max}	maximum current density carried by a near Maxwellian	5.95 MA/m^2
$\frac{J}{P_d}$	normalized current density/power dissipation ratio	21.9
$\frac{J}{P_d}$	current drive/power ratio	0.10 A/W

Appendix 7-A

The Relativistic Electron Beam Current Drive Experiment

The interest in relativistic electron beam current drive, largely motivated by the high efficiencies predicted in the STARFIRE DEMO study [BA82], has declined sharply in recent months, because of the inability of researchers in this field to find a solution to overly severe constraints on beam penetration. An additional demotivating factor for the use of REB on HESTER is that the high cost of transmission diodes discussed below makes the experiment unaffordable within the cost guidelines of this study, unless the efficiency of current drive is indeed almost as efficient as ohmic drive. However, since the definition of this experiment was completed before REB lost popularity, it is included in the appendix below, but not accorded its own chapter.

A 500 kA relativistic electron beam (REB) current drive experiment was planned for HESTER , using equipment being developed for the electron heated inertial confinement program. The REB experiment would inject relativistic electrons into a 7 keV plasma, heated by lower hybrid or ICRF power, with a line-average electron density of 1.0×10^{20} m $^{-3}$.

Relativistic electron beams have been suggested as an attractive reactor current drive concept, because of their high Q [BA82], since the required power approaches the ohmic power dissipation of the plasma in the limit of perfect momentum transfer to bulk electrons due to non-linear wave processes. For a HESTER plasma of 500 kA and 7 keV, the predicted average power of 250 kW is twice the ohmic power dissipation of a nondriven plasma and an order of magnitude more efficient than the lower hybrid experiment described in section 5.

In a possible developmental circuit for an REB experiment in HESTER, a rotating flux compressor discharges its stored energy into an air-core, 1 turn transformer in 1 ms. The transformer output charges a 1.0 MV water capacitor bank. As soon as the capacitor bank reaches its maximum charge, it is discharged into the plasma through a high voltage diode delivery system, with magnetic insulation, in 40 ns.

The rotating flux compressor is identical to those being developed at the University of Texas for the HYDRA-MITE program at Sandia. The RFC would have to be charged up to its full rotational energy by a 700 hp motor, and would discharge its energy in 1.0 ms at a peak voltage of 20 kV. The 1.0 ms pulsed, step-up transformer is a relatively simple one-turn primary, 50 turn secondary, air-core transformer in an oil tank, being developed by Sandia. The HYDRA-MITE upgrade of HYDRA will also 40 ns, 35 kJ Marx banks. In order to use the available designs of the rotating flux compressor, transformer and diode, four 35 kJ systems would be necessary for a 125 kJ pulse into the plasma twice a second. However, since present Marx generators require an hour to charge, temporary high voltage charge storage would have to be performed by water capacitors, such as those used in the PFBFA-1 facility at Sandia. The overall delivery efficiency is expected to be 50 % efficient, requiring an additional 500 kW of line power to drive the REB experiment.

The equipment cost of the experiment is dominated by the machining costs of the diode. A tokamak transmission has been previously costed at $1.1 M for a single transmission line. All other components for the experiment are costed at about $0.5 M. It is unclear at this time whether the system requirements can be met by a single diode. Since 35 kJ diodes have already been developed, 4 ports should be an absolute maximum requirement.

One of the chief problems associated with REB injection, beam deflection at the diode mount, followed by breakdown, may be solved by the short 40 ns pulses, since 40 ns is slightly less than a toroidal transit time on HESTER . The magnetic field needed for diversion of the beam, in order to avoid collision with the walls, is then self-created by the 2 MA of beam current by bending the cathode at the diode mouth. This technique was proven to be effective by Proulx and Küsse [PR82] at Cornell.

An interesting demonstration of current drive would be to heat the electrons with lower hybrid current drive, instead of ICRF. Since the efficiency of REB current drive is a strong function of electron temperature and is not expected to be a strong function of ion temperature, the use of an electron heating mechanism, should allow more efficient current generation. Of course, since both the REB and the lower hybrid current drive will be operating at the same time, it will be impossible to separate out the physical effects of the two mechanisms. However, the combination current experiment will allow an investigation of enhanced lower hybrid current drive, similar to the low electric field enhanced current drive experiment suggested in chapter 1. Also, if expected efficiencies are observed, it will also allow a current drive experiment to probe as deeply below $q_{lim} = 2.0$ as disruptions will permit at moderate to high electron densities.

Acknowledgments

Sizing of the REB experiment was done by D.A. Ehst. Equipment recommendations were made by D. Cook.

References

[BA82] C. Baker et al, "STARFIRE/DEMO: A Demonstration Tokamak Power Plant Study," Argonne National Labortory Report in preparation, 1982

[BI81] W.L. Bird et al, "Compulsators and active rotating flux compressors (ARFC)", Proc 3d IEEE Int. Pulsed Power Conf., Albuquerque, NM, 1981

[PR82] G.A. Proulx and B. Kusse, Phys Rev Letters, Mar 15, 1982

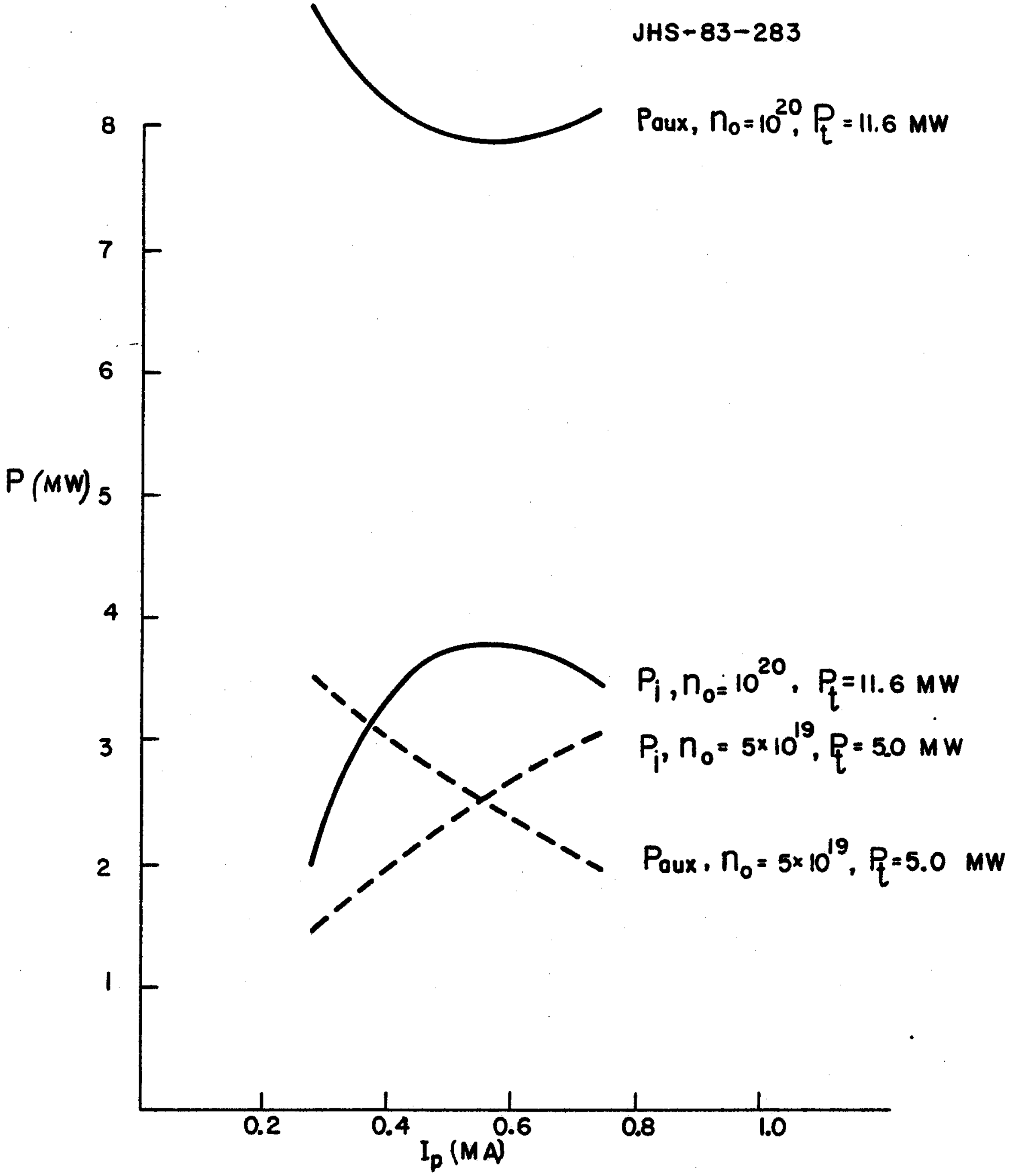

FIGURE 7.1
DIVISION OF AUXILIARY ICRF POWER AND COMPRESSIONAL AIFVEN WAVE POWER FOR FIXED TOTAL POWER AT TWO DENSITIES.

8.0 Superconducting Toroidal Field Magnet System

The toroidal field magnet system of HESTER includes several advanced features, which allow the coil system to be simultaneously high performance and inexpensive. These include:

1 Use of already developed Nb_3Sn, ICCS superconductor, avoiding the development programs that have been dominant costs in many other large superconductor purchases. This superconductor has large energy margins at the design flux density of 9.1 T, as well as probable cryostability.

2 The use of pressurized supercritical helium in a conduit, surrounded by an atmospheric pressure bath allows the electrical and mechanical integrity of potted construction, while avoiding the high entropy generation of supercritical helium circulation through long, narrow conduits.

3 The poloidal field system plans to use already manufactured superconductor, the 30 km of 7,000 A conductor from the cancelled MHD Component Development and Integration Facility (CDIF) program. This superconductor can probably be run up to 10 kA at the low fields prevailing over most of the PF system and is more than adequate for the entire PF system.

4 The Nb_3Sn superconductor is reacted after winding and has a larger void fraction than either the Westinghouse LCP or M.I.T. 12 T magnets. These two factors will result in considerably smaller peak compressive strain in the conductor and a higher critical current density.

5 Circular magnets have been shown by Bobrov and Schultz [BO81] [BO82] to require less superconductor and structural material than the constant-tension D concept.

8.1 TF Magnet System Configuration

The TF magnet system reference design includes 36 circular magnets, wound in rectangular cases using the ICCS superconductor developed for the M.I.T. 12 T and the Westinghouse LCP coils. Each coil is wound in 4 double pancakes, with a maximum number of 11 layers in a pancake. In the two central double pancakes, 2 layers have been removed to reduce the toroidal ripple in the plasma. This concept is illustrated in Fig. 8.1.1. Each double pancake is potted, in order to ensure the mechanical and electrical integrity of the coil bundle. The individual cable-in-conduit conductors have a local helium inventory, which prevents conductor quench. Long term heat removal from the magnet system is provided by liquid helium pool boiling between double pancakes. The dimensions of the reference TF magnet system are shown in Tables 8.1-1 through 8.1-VI.

Fig. 8.1.1 also illustrates other features of the toroidal magnet system design. In this design, nitrogen-cooled thermal shields are provided along the walls of the common vacuum dewar enclosing the toroidal magnet system, and on the roof and floor. Only superinsulation and vacuum separate the coil cases and the plasma first-wall vacuum vessel. This thermal insulation concept is unusual, especially on the surface facing the warm first-wall structure, but is adopted because of space considerations in a high field magnet design. The concept has been successfully tested in the prototype dipole magnets for the Colliding Beam Accelerator [WE81].

8.1.1 Leads and Header Configuration

The outer section of the TF magnets in which coolant and electrical connections to the magnets are made is shown in Figures 8.1.1.1, and 8.1.1.2, while the method of termination fabrication is shown in Figure 8.1.1.3. The outer wall of a TF magnet dewar is extended several centimeters past the end of the winding pack in order to provide space for terminations, helium feeds, and intercoil bus and headers.

The atmospheric helium bath and the intercoil electrical leads run toroidally through two common bus and helium header conduits near the top and bottom of the TF coils, as shown in Figure 8.1.1.4. These conduits also contain a smaller tube, which is the header for the supercritical pressurized helium feed to the coil conduits. The entire volume enclosed within the outer coil cases of the TF magnets is bathed in helium, leaked through holes in the atmospheric helium inlet header.

Each double pancake is individually vented on either side. Figure 8.1.1.2 shows an interpancake hydraulic connection and vent line. The pressurized feed is from the inlet manifold into the far double pancake on one side of the winding pack and out of the other side to the outlet manifold. The feed does not go directly from the manifold to the coil, but travels up the vent stack through a Tee and back down to the cable hydraulic fittings, in order that all helium valves be outside the coil case in a serviceable location.

The cable hydraulic fittings are shown in Figure 8.1.1.3, which shows the fabrication method of the coil terminations. This method is identical to that being used for the M.I.T. 12 T coil [ST82], with the small exception that a Monel welding adapter is no longer believed necessary, so that the copper sleeve will be brazed directly to the stainless steel sheath. The stages in forming a termination are to remove the sheath and the stainless steel tape around a section of cable, swage a copper tube over the cable, separate the strands and insert a Monel cooling tube through the middle of the strands, then swage the copper tube down to a 5 % void fraction, squaring it off in a Turk's head. The joint is then made by soldering two such lengths of copper terminations together.

Interpancake joints are held in place by curved steel retaining pieces, as shown in Figure 8.1.1.2. Each steel retainer is welded to the outside of the cable leads' sheaths, near the termination. Pins are inserted between the copper terminations and the steel retainer, in order to resist intertermination shear, as a redundant backup to the solder joint.

8.1.2 TF Conductor Selection and Description

The TF magnets are wound with the jacketed, cabled superconductor of the type developed by Airco [SA79] for use in the Westinghouse LCP coil and the M.I.T. 12 T winding. The conductor dimensions are described in Table 8.1-II. This conductor was selected for several reasons. In order to meet the high field requirements of the plasma, it was necessary to select a high performance superconductor. However, a cost survey of large superconductor purchases indicated a requirement to avoid adding the cost of a superconductor development program to the the basic superconductor cost. The survey showed that even in quantities as large as those for LCP, new superconductor development could double the cost of superconductor. While a few other superconductors, tested in small quantities, have demonstrated higher performance than this conductor, none are considered to be fully developed at this time. A manufacturer's quotation confirmed that the specific cost of a new purchase of this conductor would be less than 3/4 that of the original purchases by either Westinghouse or M.I.T.

The performance requirements of the TF superconductor, when the response to pulsed ac losses and disruptions are taken into account are quite demanding. For example, an earlier design attempted to take advantage of already manufactured superconductor from the canceled CDIF program. Operating this conductor at only 70 % of its original design current, the calculated energy margin of the conductor for avoidance of coil quench was marginally smaller than the predicted peak energy deposition in the conductor. This behavior is symptomatic of design with monolithic NbTi superconductor at any temperature. The most significant example is that of the Tore Supra superconductor, which is only marginally stable against predicted energy depositions by disruptions, despite immersion in a superfluid helium bath [AY82]. Given some uncertainty in ac loss modeling and great uncertainty in disruption modeling, it was felt necessary to design to a conservative safety margin. Furthermore, the goal of an inexpensive experiment is influenced by the ability to use the same rf equipment as that to be used in Alcator C. The lower hybrid current drive equipment, in particular, improves in efficiency by 46 % as the central field increases from 8 T to 10 T, and falls off rapidly below 7 T [PO82], the central cutoff field at which the launching frequency $\omega = \sqrt{\Omega_{ci}\Omega_{ce}}$, the geometric mean of the electron and ion cyclotron frequencies. Thus, since 7 T is marginal for high efficiency current drive, it is desirable to design a system that can guarantee 7 T on axis, and perhaps be run up to 8.5 T. Sufficient structure for 8.5 T operation is incorporated in the initial design, with the "perhaps" relating only to fundamental uncertainties as the safety margin of the conductor vs. disruptions is reduced. The baseline operation has a large, defensible design against disruptions; after plasma operation has begun, plasma and TF currents would be increased until the empirical limit of TF magnet stability vs. disruption was established. The maximum possible field at the magnet then is 11 T, vs. the nominal, conservatively designed value of 9.1 T, effectively precluding an economical design against disruptions using NbTi, even in superfluid helium. The reference design would have to be subcooled to 2.5 K in order to achieve this performance.

8.1.1.2 Alternative Conductor Option

In the past year, a number of superconductor manufacturers have begun to produce moderate quantities of a new Nb_3Sn conductor, using an internal tin process that allows more complete reaction with niobium [SC82]. Critical current densities in noncopper of approximately twice that of bronze method Nb_3Sn have been reported over a range of magnetic fields and a few hundred pounds of practical conductor have been delivered for use in small dipole magnets for high energy physics.

An alternative cable-in-conduit conductor was recently proposed for HESTER, assuming 10^5 A/cm^2 in the bronze region of each internal tin conductor and using 486 0.7 mm strands within the sheath space of the reference conductor. Because of the high current density, as well as the low copper-noncopper ratio (3:7) in an individual strand, only 1/3 of the strands contain superconductor, the other 2/3 being pure copper. In the reference design, all of the strands are superconducting. Because of the smaller number of the more expensive superconducting strands, the manufacturer's estimate of the superconducting cable cost for HESTER is substantially less than that using bronze method conductor [SC82]. However, the manufacturer's estimate did not attempt to relate critical current density to compaction within a sheath. This correlation needs to be made before a fair quantitative comparison can be made between the two options. M.I.T. is currently acquiring samples of the new conductor in order to begin testing its properties for this application.

8.1.2 Conductor Critical Current

The estimate of conductor critical current is based primarily on the test data of Hoenig and Steeves [HO82], but also correlates well with data from the Westinghouse LCP Program [WE80]. Critical current in subcables of the basic conductor have been tested extensively by Hoenig and Steeves at 4.2 K and a wide range of magnetic fields. Besides temperature and field, critical current is also a first order function of conductor strain. The dominant cause of conductor compressive strain is differential contraction of the cable and sheath during cooldown. This effect is itself a strong function of the degree of cable compaction. The relation between critical current and cable compaction in subcables is shown in Figure 8.1.2.1.

The peak residual compressive strain in the superconductor is lower than that in the Westinghouse LCP coil and, therefore, the critical current density at any field is higher. The difference is due to a fundamental superiority of reacting after winding over winding after reacting, which was first discovered in the course of evaluating the HESTER design. The difference is illustrated in Figure 8.1.2.2. The test data of Hoenig is superimposed over the test data on the Westinghouse LCP coil [WE80] with the significant difference that the peak critical current density is at a superimposed tensile strain of 0.7 % for the Westinghouse LCP coil, while it corresponds to the zero external strain or zero compaction case for the HESTER conductor. The basic argument is as follows. The dominant compressive strain in ICCS conductor is typically that due to differential contraction between the cable and the sheath. For the 32 % void fraction of the LCP and MIT 12 T conductor, this is believed to be a 0.5 % strain [HO82]. If one winds after reacting, bending strain in the conductor is superimposed on the thermal contraction strain. Since all strands are fully transposed, each strand becomes a maximally compressed fiber at some position. Tests at Westinghouse suggest that at a void fraction of 32 %, the bending strain in a cable is $\frac{1}{4}$ that of the conduit. Thus, a 2 cm conductor with a bending radius of 50 cm would have a peak compressive strain of 2 % in the conduit and 0.5 % in the conductor, leaving a peak compressive strain of 1 % in the conductor, corresponding to a loss of 80 % of the zero strain critical current. The Westinghouse LCP fabrication procedure attempts to compensate for this by winding on the activation reel in the opposite direction from the winding on the coil bobbin, so that the unwinding and rewinding strains partially cancel. Unfortunately, all LCP coils are Dee-shaped, with a wide range of radii of curvature, so that exact cancellation is impossible. The process of reacting the superconductor after winding anneals out all of the bending stresses due to winding. The compressive stress is also less than that in the Westinghouse or the original

M.I.T. 12 T winding, because the void fraction is 42 %, instead of 32 %.

8.1.2.1 Conductor Stability

The performance of the TF superconductor against ac losses and disruptions is shown in Table 8.1-III. The average power dissipation of 26 W is a very small fraction of the total system refrigeration requirements. The maximum predicted energy deposition in the conductor, due to start-up, is only 3.9 mJ/cm^3, less than the adiabatic stability limit, and orders of magnitude less than the enthalpy of the conductor and helium in a conductor envelope. The maximum predicted energy deposition in the conductor during a disruption occurs off the equator on the inside, as it does in Tore Supra [AY82], and is 29 mJ/cm^3, corresponding to better than an order of magnitude safety margin vs. the available enthalpy in a conductor envelope between the bath temperature of 4.2 K and the current-sharing temperature of 5.9 K. As shown in Table 8.1.V, the total enthalpy per cubic centimeter of metal needed to raise the metal and helium bath of an envelope around the conductor to the current-sharing temperature is 565 mJ/cm^3. The actual recovery energy of an ICCS conductor is generally smaller but comparable to this simple measure of the energy margin.

Experimental confirmation of the expected energy margin for recovery was provided by Hoenig [HO78], who heated a 3 m long, 57 strand, Nb_3Sn cable with a 1.5:1 copper/noncopper ratio at a temperature of 4.2 K and a pressure of 3 atmospheres. At 9 T and 5.8 kA, corresponding to 73 % of critical current and 402 A/mm^2 in the noncopper, the entire conductor was heated for 18 ms. With no bulk helium flow, the energy margin was 533 mJ/cm^3, increasing to 608 mJ/cm^3 at a Reynold's number of 76,000. These parameters are all very close to those of the HESTER design. Two transient simulations of HESTER , using SCAN, an ICCS transient recovery code developed by Arp, showed recovery after a 10 ms pulse over 1.0 m of 445 mJ/cm^3 and no recovery after a 623 mJ/cm^3 pulse, with no bulk flow, an initial temperature of 4.2 K and an initial pressure of 2.4 atmospheres. The recovery case is shown in Figure 8.1.2.1.1.

8.1.3 Heat Removal

Heat generated within the TF windings, in particular the heat generated by routine start-up and shut-down pulses, must be largely removed from the TF coil system, before a new cycle can begin. This may be a limiting step in determining the minimum time between plasma discharges. In order to remove heat entirely from the TF system, it must diffuse through the conduit jacket and through the potting insulation into the interpancake pool. From there, bubbles must rise through the height of a TF coil.

The thermal time constant of the jacket and insulation can be estimated by using the specific heat and thermal conductivity of epoxy at cryogenic temperatures. If a double pancake is heated to 6.0 K, which is the expected threshold of current-sharing at 9.0 K in Nb_3Sn, the calculated heat flux at a temperature difference of 1.8 K between the coil and the bath is 2.25 W/m, while the enthalpy difference in the conduit-enclosed helium at constant density is 210 J/m. Thus, the initial slope of the energy transfer implies a thermal time constant at 6.0 K of 92 s. The pressure at constant density at 6.0 K is 11 atmospheres, as opposed to a pressure of 2.4 atmospheres at 4.2 K. If only one part of a pancake were heated, this pressure differential would be eliminated in far less than 92 s, so we assume isothermal heat transfer along each double pancake. In order to heat the double pancakes uniformly to 6.0 K, it would be necessary to deposit 2.6 MJ in the windings, which would cause an instantaneous heat flux into the pool of 28.5 kW. These rather high values contrast with the calculated values of 2.8 kJ of expected energy deposition per start-up ramp and 224 kJ of expected energy deposition per disruption. At 5.0 K, the heat flux decreases to 1.0 W/m and the enthalpy rise decreases to 100 J/m, giving an instantaneous time contant of 100 s. At 4.3 K, the thermal time constant has risen to 300 s, implying that for the reference cycle of 600 s between pulses, the temperature difference between the cable and bath will be somewhat under 0.1 K. The predicted thermal time constant of 300 s is somewhat long and should perhaps be reduced in order to compensate for likely debonding and other causes of increased thermal resistivity. However, it is interesting to note that if helium were circulated through each double pancake with a total length of 92 at a velocity of 25 cm/s (the same as the nominal velocity of helium through the Westinghouse LCP conductor at the Large Coil Facility), it would take 368 s for helium to travel from the inlet to the outlet. The greater reactor relevance of the stagnant helium design being used here should be apparent when one considers that the lengths of double pancakes in reactors are usually measured in kilometers.

8.2 Force Calculations and Stress Analysis

The achievement of a mechanically efficient design of the toroidal field magnet sytem is perhaps the key engineering problem of the machine. Although not absolutely necessary to the machine mission, it is highly desirable to achieve higher fields on axis than the larger tokamaks being built in the 1980's, including TFTR, JET, JT-60, Big Dee and Tore Supra. This goal is desirable in order to allow unique regions of plasma parameter space to be explored, in particular current drive at high densities, and because of the at least linear improvement of achievable plasma temperature/pressure for fixed auxiliary power with toroidal field. At this early point in the design, it would be untrue to claim that the necessary structural efficiencies have been achieved or that understanding of overall structural behavior is adequate to know whether it can be achieved. However, with the achievement of this goal established as the principle mission of the TF magnet system design, the engineering effort will be focused on the twin goal of achieving at least 7 T on axis, while supporting the overturning moments and pulsed losses due to the highest possible beta plasma discharge.

The structural principles that, it is hoped, will allow a mechanically efficient design include:

1 Potted, rather than open pool boiling, pancake construction.

2 Use of the most structurally efficient coil shape, i.e. circular. The justification of the belief that circular coils have greater structural efficiency than, for example, Dee shaped coils is found in Appendix 8.A.

3 A large number of toroidal magnets, allowing the structural concept to approach a monolith as nearly as possible.

4 High aspect ratio, minimizing the pressure differentials between the inner and outer legs of the coils. This minimizes the bending and centering stresses due to the departure from solenoid magnet behavior of a toroidal coil system.

5 Solid intercoil wedges. This is not the most mass efficient concept nor the concept that minimizes pulsed losses, but it should be the strongest for a fixed volume.

6 Poloidally continuous wedges between every second toroidal field magnet. The creation of two coil modules greatly increases the effective moment of inertia against overturning. Because of the high expected power density launching capability, using only rf sources, it is possible to achieve high overall wall loading with only half of the possible number of ports. However, as explained below, the existence of vertical ports between every second coil still provides stress relief against the strain incompatibility at the

crown of the toroidal structural shell.

8.2.1 Stress Allowables

Although no structural standards have been adopted for the construction of superconducting magnets and there appears to be a broad consensus that such standards would be premature, the ASME Power Boiler Code for Nuclear Power Plant Components [AS80] has been used for many recent large superconducting systems designs, such as LCP, EBT-P, FED and INTOR. Barring any specific structural insight that the code is inapplicable in a given situation, it will be adopted for the HESTER design. The sort of structural insight that might lead to deviation from the Boiler Code rules might be expected to include shear limitations in composite bonding materials and strain limitations in Nb_3Sn.

ASME Boiler Code limitations are shown in Table 8.2-I. Whichever limit is the most restrictive is taken as the basis for design. Primary membrane stress intensity is defined as the average (i.e. uniform stress necessary to achieve global force balance) difference between principal stresses over a cross-section. Primary bending stress is the linearly varying component of the stress normal to a cross-section (i.e. for nonlinear cases, the linearly varying component that would give global moment balance).

Because a detailed fatigue analysis has not yet been performed for each material, an allowable membrane stress of 420 MPa (630 MPa membrane plus bending) has been selected for the stainless steel structural members, including the bobbin, outer plate, case sidewalls, outer leg wedging blocks, wedging block pins and wedging block bolts, even though the pins and bolts should have higher strength than the larger structural members. This conservatism could not quite be obtained in the conductor sheath, as explained in section 8.2.2. The sheath strength of the JBK-75 jackets is limited by the weld strengths, which have a yield strength of 1156 MPa and an ultimate tensile strength of 1622 MPa for the GTA weld (SA-982 C) [GO80]. These properties imply a static allowable membrane stress of 540 MPa (78.5 ksi). This higher allowable membrane stress is supported by fatigue tests at Westinghouse, in which a sheath was stressed to 90 ksi for 5,000 cycles with no yielding or inelastic behavior [WE80].

8.2.2 Finite Element Analysis of In-Plane Stress

Finite element analysis of the toroidal field magnet structure was done using the PAFEC stress analysis code. Three simulations were completed in order to determine the correct and/or desirable boundary conditions for the coil restraints. These simulations were

[1]: Coil supported by inner bobbin only, with no slip between coil layers. The specification that the coil is supported by the inner bobbin only, corresponds to the case in which there is a significant weld gap between the outermost layer and the outside case wall, as was done in the EBT-P prototype magnets [BA81]. The specification of no slip implies a perfectly potted coil, with no delamination.

[2]: Coil supported by outer case only, with no slip between coil layers. The finite element analysis showed that, if the outer case is sufficiently close to the outermost layer ($<$ 0.1 mm), the coil winding will leave the inside bobbin, and will be supported against in-plane translation everywhere by the outer case.

[3]: Coil supported by outer case only, with no shear between coil layers. This corresponds to an unpotted case or to a case in which shear stresses were sufficiently large that hardly any bonds survived. Since we are not contemplating deliberately unbonded construction, the second and third models represent upper and lower bounds on coil behavior.

The finite element analysis of a TF coil supported by the inner bobbin quickly revealed the undesirability of designing the coils without positive support from the outer case. Without outside support, the coils lift off 3 mm from the inner bobbin on the inner leg. Figure 8.2.2.1 shows the membrane tensile stresses in the sheaths of the first, fifth and tenth layers. The peak membrane stress, occurring in the first layer, near the crown of the coil, is 570 MPa, vs. an allowable in JBK-75 of 540 MPa membrane stress at 4 K. The radial stress adds another 175 MPa to the membrane Tresca stress, while the potential upgrade to 11 T would increase stresses by another 40 %. Thus, the approach of using self-supporting conductors does not satisfy Boiler Code allowables.

If the coil is potted and there is no gap between the outer case and the coil winding, the winding will lift off the inside bobbin everywhere and the outside winding will be directly supported by the outer case everywhere. In this case, as shown in Figure 8.2.2.2, the peak poloidal stress is reduced to 290 MPa and the radial compressive stress at the tenth layer is 170 MPa, as shown in figure 8.2.2.3. At the tenth layer, the peak poloidal stress is only 50 MPa at the inside equator and 140 MPa at the crown. Combined Tresca membrane stress was not printed out directly by the finite element code, but is equal to 220 MPa at the inside equator of the tenth layer, 245 MPa at the crown of the tenth layer and 305 MPa at the inside equator of the first layer, all well within the allowable of 540 MPa, and allowing the possibility of an upgrade to 11 T. The radial gap between the first layer of conductor and the inner conductor varies from 0.08 mm at the outside leg to 0.18 mm at the inside leg, as shown in Figure 8.2.2.4, indicating that the winding pack will lift off from the winding bobbin, everywhere along the coil. The maximum radial deflection of 0.18 mm is lowest for this case and is only one-twentieth the maximum deflection of that for the coils supported by the inner bobbin. The shear stress in the conduit walls due to in-plane loads is shown in Figure 8.2.2.5. These stresses are most severe in the middle layers, peaking at 30 MPa in the fifth layer. In the ground wrap surrounding the conduit, this translates to a shear of 4.4 MPa (650 psi). Considering the additional shear due to out-of-plane loads, considered in the next section, this may be marginal for epoxy bonds. This consideration leads to the third model, assuming that the coil is supported by the outer case, but that all layers are free to slip (no bonding). This is not an actual proposed fabrication method, but represents a limit of coil behavior. The actual stresses in the TF coils should be intermediate between those calculated in the second and third finite element models. Finally, the primary poloidal tensile stresses in the case walls are shown in Figure 8.2.2.6. The peak value of 77 MPa appears at the inside equator in the winding bobbin. These values are low in comparison with the stresses in the conduits and reflect the ability of a perfectly bonded winding pack to take most of the load.

With the coils supported by the outer case and each layer free to slip, there is no shear in the conduit walls due to in-plane forces. Similarly, the poloidal tension stresses in each layer are essentially constant over a turn, as shown in Figure 8.2.2.7. The peak tensile stress appears in the first layer, as before, and is only 220 MPa. The peak radial stress, as shown in Figure 8.2.2.8, appears in the tenth layer at the equator, and is 180 MPa, as before. The peak Tresca membrane stress in the tenth layer is 285 MPa, only slightly lower than that in the perfectly bonded model, despite the significantly lower peak tensile stress, because the peak tension and compression stresses are more "out-of-phase" for the bonded case. The radial gap between the first layer and the inner bobbin is shown in Figure 8.2.2.9, which shows that the winding separates from the bobbin everywhere, as it did for the bonded model. The peak gap of 0.195 mm is only slightly higher than the peak gap for the bonded case. The primary, poloidal tensile stress in the inner, outer and side walls of the coil cold case are shown in Figure 8.2.2.10. The peak stresses are low, with the worst spot being 165 MPa at the inside equator of the inner bobbin. This peak stress is, however, about double the peak bobbin stress for the bonded case.

The finite element analysis as it has been completed does not answer all questions about the structural behavior of the TF magnets. Bending in the conduits, buckling and local stress concentrators have not been addressed. However, as far as the analysis goes, if the primary stresses and allowables studied in the finite element analysis and the primary plus bending stresses studied in the shell model are indeed the dominating factors, it appears that one should design for a fully bonded design with winding pack translation supported by the outer case. If shear stresses must be lowered to allow a conservative design against debonding, increasing the thickness of the outer case, as will done on the 24 coil Alcator DCT iteration of this design, appears to be a solution.

8.2.3 Toroidal Shell Analysis

A quick and accurate analysis of stresses in coil cases and out-of-plane structures can be made by using the thick toroidal shell model of Bobrov [BO81] [BO82]. This model uses the equations from Reissner's toroidal shell theory in order to find the solution for the stresses in a thick shell with orthotropic (i.e. anisotropic in two directions) properties, acted upon by symmetric (in-plane) and antisymmetric (out-of-plane) forces. The technique is sufficiently detailed to model exactly the lack of structure in port regions, the discrete nature of forces on the structure and the lack of toroidal symmetry in the ports (i.e. only every second coil pair has ports between them). The finite difference solution using the Bobrov analysis technique requires less than a hundredth of the computer time needed by a finite element analysis and less than 1/10 the set-up time, making it appropriate for parametric analysis and planning exercises, such as the present study.

The results of the in-plane stress analyses are shown in Figures 8.2.3.1 and 8.2.3.2. The primary membrane stress in the shell in the poloidal (winding) direction varies from a peak of 147 MPa (21.4 ksi) at the inside equator to a minimum of 116 MPa near the outside equator. The peak stress is 10 % lower than that calculated by the finite element method for a coil supported by the outer case. The peak stress is 11 % higher than the average or ideal constant stress. The toroidal shell compressive stress varies from a peak of 197 MPa (28.6 ksi) at the equator to 178 MPa (ksi) at the vertical ports in the inside wedge and is nearly constant at 117 MPa (17 ksi) in the outside wedges. The peak primary membrane stress intensity then is 344 MPa (50 ksi) in the case walls at the inside equator. For 304 LN at 4.2 K, the minimum tensile strength is 1,700 MPa (247 ksi), while the minimum yield strength is 760 MPa (110 ksi) [RE79]. Using the above figures of material strength, the allowable primary membrane stress intensity would be limited by the yield strength at 73 ksi, but for thick pieces has been limited to 60 ksi, as discussed in section 8.2.1.

The combined membrane and bending stresses in the outer fibers of the toroidal magnet structural shell are shown in Figure 8.2.3.2. The combined membrane and bending stress in the poloidal direction has a peak of 228 MPa (33 ksi), an increase of 55 % over the peak primary tensile stress. The combined membrane and bending stress in the toroidal direction has a peak of 244 MPa (35.5 ksi), an increase of 24 % over the primary compressive stress. The combined membrane and bending stress intensity at the outer fibers of the inner equatorial cross-section is 472 MPa (68.6 ksi), an increase of 37 % over the peak primary stress intensity. Thus, bending stresses, being less than 50 % of primary stresses have no effect on allowables. This points out again that the many reactor designs that assumed that the minimization of bending was the sole criterion for structural efficiency in superconducting, toroidal magnet systems were making an unjustified assumption.

The ratio of peak to allowable stress is marginal for a 2 T upgrade from 9 T to 11 T peak field at the coils. Since all of the peak stresses occur at the outer fibers of the structure at the inside equator, reinforcement of that area with a thicker outer case is suggested. A thicker outer case wall would also be helpful in reducing local centering forces, as discussed below.

8.2.4 Out-of-Plane Loads and Shear Stress Analysis

Out-of-plane loads can dominate toroidal magnet design because of their pulsed nature and because of the inability of the winding pack to contribute much strength in resisting them. A preliminary evalution of these loads has been made, again using the Bobrov thick shell analysis [BO82].

The radial and vertical fields at the toroidal field magnet due to the reference high beta, high current discharge used for engineering sizing (See Ch. 9) are shown in Figure 8.2.4.1. The running shear stress resultant due to these forces, using thick toroidal shell analysis, is shown in Figure 8.2.4.2. The shear stresses across the planes of the case and the winding pack are very low. Shear stress multipliers in the intercase pins and the interlayer sheets have not yet been completely determined.

8.3 TF System Heat Loads

8.3.1 Pulsed Magnetic Field Losses

The pulsed losses in the toroidal field system are very low due to the use of the low eddy and coupling currents in cabled conductors, relatively low poloidal fields due to the high aspect ratio plasma and the lack of high elongation or beta experiments, and relatively slow start-up and ramp down times. As will be discussed in chapter 11, the losses in the poloidal field magnet system dominate the system refrigeration requirements due to pulsed losses.

Two methods were used for calculating pulsed losses. When applicable, the test data of Wagner on the Westinghouse LCP conductor was used. The shorted transformer secondary approximation of Shen [SH78] [SH79] was used as a check. Although Shen does not ascribe second-order accuracy to his method, it was selected because of its ability to handle nested structures, because it does not break down in the transition regime between full flux penetration and full flux exclusion, it has adequate experimental verification, and because it is significantly easier to understand than most other methods, especially for complex configurations. The Shen shorted secondary method, however, only describes diffusive flux penetration effects, such as transverse and parallel eddy losses and transverse coupling losses. Filament hysteresis losses are straightforward, while parallel coupling losses are modeled as a macroscopic hysteresis phenomenon with only partical flux penetration, because of the long decay time of parallel coupling supercurrents. However, since parallel coupling losses are predicted to be the largest loss component in the superconductor, they require a more sophisticated analysis, supplemented by experimental investigations. The identification of parallel coupling loss, followed by transverse coupling loss, as the two largest loss components differs from the implication of the Westinghouse test data that transverse filament hysteresis losses would be predicted to be the single largest loss term. The predictions of transverse filament hysteresis losses have been calibrated against test data, but the predictions of coupling losses are more dependent on the strand insulation concept, since the interstrand insulation selected for both the Westinghouse LCP cable and the M.I.T./Livermore 12 T cable have a relatively low quality coil insulation whose effectiveness in preventing interstrand current is inadequately characterized. M.I.T. is currently working with Airco to independently develop the higher quality CuS strand insulation, benchmarked at Westinghouse [WE80].

8.3.2 Conduction and Radiation Losses

Radiation losses in HESTER are high in comparison with conduction losses, because of the absence of nitrogen cooled radiation shields on the inside surfaces of the TF magnets. However, as shown in the summary of cryogenic losses in Table 11.1.1., radiation losses are less than a fourth of the dominant refrigeration load, the pulsed losses in the poloidal field system. Radiation losses were scaled from the measured losses in the dipole magnets in ISABELLE [WE81], which are separated from a high vacuum beam tube by superinsulation without a nitrogen cooled shield. Confirmation of heat loss performance would be part of the experimental development program proposed for HESTER.

8.3.3 Joint Losses

The joint concept used for the HESTER TF coil system was developed and tested for the M.I.T. ICCS-HFTF program [ST82]. A 2/3 scale conductor was tested up to 20.9 kA for that program, with a measured joint voltage of 56 μV at zero field. Extrapolating test data to 25 kA indicates a probable joint voltage of 65 μV in HESTER . However, the joint concept to be used in HESTER will have at least twice the contact length of that tested by Steeves [ST82]. The new concept will be tested in 1983. If there is an average joint voltage of 33 μV at 25 kA, the total joint losses in the TF system for 36 coils and 3 interpancake joints and 2 lead joints per coil would equal a refrigeration load of 150 W.

8.3.4 Lead Losses

The selection of the number of leads to be brought out to warm bus is based on the trade-off between low refrigeration requirements with a low number of leads and low terminal voltage with a high number of leads. As explained in the section on TF magnet protection, a voltage limit of 4 kV was imposed, leading to a design discharge voltage of 3.2 kV when 18 coils are discharged in series. This design leads to 2 pairs of leads being brought out to warm bus and 2 pairs of 18 interleaved coils being discharged in parallel.

The nominal current through the TF conductor is 25 kA, but the coils must be designed for a possible upgrade to 30 kA. If the original set of leads are designed for 30 kA, approximately 180 l/hr of helium flow would be required through the 4 leads. If supplied directly by a refrigerator, this would require the same amount of power as 550 W of refrigeration at 4.2 K. If the initial lead design were sized for 25 kA, the helium requirement would be reduced to 150 l/hr.

8.4 TF Magnet Protection

In the event of a TF magnet quench, the magnet must be discharged through an external dump resistor. Quench is detected by pressure sensors within each of the double pancakes. The temperature rise in the conductor is limited to 200 K, while the terminal voltage across a coil dump circuit is limited to 3.2 kV

8.4.1 TF Magnet Protection Circuit

The TF magnet system consists of 2 parallel pairs of 18 coils in series, charged through 2 pairs of 25 kA leads. Each coil is surrounded by 2 coils from the other pair. When a quench is detected in one coil, all 36 coils are dumped simultaneously through 2 independent dump networks. The dump resistor for each series coil set is 125 mΩ and is capable of dissipating 200 MJ.

8.4.2 Temperature Rise Limitation

Absolute limits on temperature rise on coil quench include copper annealing at $\approx$ 150 C and damage to epoxy insulation at $\approx$ 50 C. In most magnet designs, the most limiting failure mechanism may be delamination of the epoxy-conductor bond due to thermal stresses. In a potted ICCS winding, delamination should not cause failure, because there is no place for a debonded insulation to move. However, the avoidance of bond breaking is still desirable.

If one takes the most conservative basis for design, that there is no compression on the bond from adjacent conductors and that there is no reduction of conductor current as the coil warms up, and that heat transfer from helium to the conductor jacket is rapid, while heat transfer from the jacket to epoxy is slow, a conservative temperature limit can be calculated. If one assumes that a cryogenic bond between epoxy and steel has a shear strength of 2 ksi, and that the shear stress developed in the bond is typically equal to the tensile stress developed in the conductor due to differential expansion, the permissible strain for a G-10 epoxy/glass fiber composite with a Young's modulus of 29.4 GPa is 0.5×10^{-3}, corresponding to a temperature rise from 4.2 K to 80 K. An exact limit cannot be calculated without a three-dimensional transient analysis and good knowledge of the statistical properties of the bond. Since delamination should not cause failure, and since case walls, reduction of coil current and compression on the bond should all reduce the probabilty of bond failure, we have adopted the more optimistic limit of 200 K.

8.4.3 Voltage Rise Limitation

The turn-to-turn and layer-to-layer insulation in a cable-in-conduit superconductor is more rugged electrically than an open pool conductor, because a complete ground wrap can surround each conductor, instead of merely spacers. The voltage rise limitation is based on the Westinghouse LCP verification testing [WE80]. Westinghouse tested several insulating wraps around rectangular copper bars of the same size as the HESTER conductor. These samples were bent to a radius of 70 cm, coincidentally the average turn radius of the HESTER windings. The voltage breakdown tests were performed at room temperature in air and in vacuum and at 4.2 K in vacuum. The minimum 60 Hz breakdown voltages of kapton, epoxy glass insulation at room temperature and in air were 15 kV, at room temperature and in vacuum were 11.5 kV and at liquid helium temperature and in vacuum were 9.2 kV. Since the highest voltage would be applied at the beginning of a coil dump, the voltage at low temperature is the most limiting.

The selection of a voltage slightly higher than 3 kV is somewhat arbitrary. The voltage tests indicate that a somewhat higher voltage could be selected. However, these tests were performed over a small number of samples. Furthermore, the Westinghouse LCP coil is designed for a dump voltage of only 2.5 kV, so higher voltages will not be field tested as part of the LCP program. This is particularly important because high voltage standoff will not be tested at all at hydraulic connections and electrical joints, except where they are benchmarked by the Westinghouse coil.

8.5 Toroidal Field Ripple

Because toroidal magnets consist of discrete coils, instead of a continuous winding, ripple will appear in the toroidal magnetic field, which can have a deleterious effect on plasma confinement of hot ions. The design approach to limiting toroidal ripple in HESTER includes the following concepts:

1. A large number of toroidal magnets, 36 , allows the coil bore to be close in size to the maximum plasma minor radius, thus using the high performance superconducting magnets in a cost effective manner.

2. There is no warm structure between adjacent magnets, obviating the need for space-consuming thermal isolation.
3. Wherever possible, necessary structure is placed external to the sidewalls at the throat.
4. The option of reducing ripple by introducing a notch in the middle of each TF coil has been investigated.

Contours of constant ripple for a baseline 36 coil case with no notch in the TF coil are shown in Figure 8.5.1. In a broad band between $1.92 < R < 2.27$ m, the toroidal ripple at the equator is less than 1 %. The contour of 1 % ripple runs between 1.79 m and 2.45 m, corresponding to a minor radius of 33 cm. The contour of 2 % ripple runs between 1.75 m and 2.5 m, corresponding to a minor radius of 37.5 cm. The constant ripple contours are nearly circular and very slightly more elongated than circular. Thus, the maximum ripple at most circular discharges would be at the equator, but more toward the crest for significantly elongated discharges.

A comparison between the toroidal ripple at the equator with and without the notch is shown in Figure 8.5.2. The principle beneficial effect of the notch is at the high field side of the plasma where ripple is halved, the effect being second order on the low field side. The trade-off between design with or without the ripple-reducing notch appears to be very close, and thus not very important.

Acknowledgments

E.S. Bobrov and T. Morizio created a finite element model of the TF magnet system and analyzed TF coil stresses. H. Becker analyzed magnet stresses. P. Gierszewski analyzed conductor recovery. M.O. Hoenig selected the TF superconductor. R.J. Thome and W.J. Langton analyzed toroidal field ripple.

References

[AS80] ASME Power Boiler Code, Section III, Nuclear Power Plant Components, Article XIII-1000

[AY82] R.Aymar, "Tore Supra: Programme of Development Qualifying Tests," Euratom Report EUR - CEA - FC - 1143, Feb 1982

[BA81] J.K. Ballou et al, "Design and construction of the EBT-P development coils," 9th Symp Eng Probs Fus Res, Chicago, IL, Oct 1981

[BO81] E.S. Bobrov and J.H. Schultz, "A model of toroidal magnet systems as orthotropic shells of finite thickness," 9th Symposium on Eng Probs of Fusion Research, Chicago Il, Oct 1981

[BO82] E.S. Bobrov and J.H. Schultz, "Analysis of toroidal magnet systems on the basis of the Reissner Shell Theory," M.I.T. Plasma Fusion Center Journal Article PFC/JA-82-14, Aug 1982, to be published in ASME Pressure Vessel and Piping Division Transactions

[GO80] R. Gold et al, "Evaluation of conductor sheath alloys for a forced-flow Nb_3Sn superconducting magnet coil for the Large Coil Program," Adv Cryo Eng, 1980

[HO78] M.O. Hoenig, private communication, 1978

[HO82] M.O. Hoenig and M.M. Steeves, "Experimental parameter study of subsize Nb_3Sn cable-in-conduit conductors," Applied Superconductivity Conference, Knoxville, TN, Dec 1982

[PO82] M. Porkolab et al, "Lower hybrid heating and current drive experiments on the Alcator C and Versator II tokamaks," IAEA-CN-41, 9th Internatl Conf Plas Phys and Controlled Nuclear Fusion Research, Baltimore, MD, Sept 1982

[RE79] D.T. Read and R.P. Reed, (F.R. Fickett and R.P. Reed, eds.) "Properties of selected austenitic stainless steels at cryogenic temperatures," National Bureau of Standards Report NBSIR 79-1609, Je 1979

[SA79] P.A. Sanger et al, "Developments in Nb_3Sn Forced Flow Conductors for Large Magnets," IEEE Trans Mag, Vol. MAG-15, No. 1, Jan 1979

[SC82] R.E. Schwall et al, "Properties and performance of high current density Sn-core process MF Nb_3Sn," Appl Superconductivity Conf, Knoxville, TE, Dec 1981

[SC83] J. Scudiere, private communication

[SH78] S.S. Shen and R.E. Schwall, "Transient loss analysis and measurements on normal conductors and composite superconductors," 7th Internatl Cryo Eng Conf, July 1978

[SH79] S.S. Shen, "Saturation and anisotropy effects of magnetization in practical composite superconductors," Oak Ridge National Laboratory Report ORNL/TM-7036, Oct 1979

[ST82] M.M. Steeves and M.O. Hoenig, "Lap joint resistance of Nb_3Sn cable termination for the ICCS-HFTF 12 tesla coil program," M.I.T. Plasma Fusion Center Report PFC/RR-82-22, Aug 1982

[WE80] Westinghouse Electric Corp, "Superconducting magnet coils for the Large Coil Program, Phase 2 Final report to Union Carbide Corporation, Volume 1: Introduction and verification testing report," Mar 31, 1980

[WE81] A.P. Werner, D.P. Brown and W.J. Schneider, "Heat load measurement of prototype cryogenic magnets and leads for the Isabelle Project," ICEC Conference, 1981

Table 8.1-1

DIMENSIONS OF THE SUPERCONDUCTING TF MAGNET SYSTEM

R_{mintf}	minimum major radius of the TF magnet, including warm case	1.385 m
B_{maxtf}	maximum flux density at the toroidal field coils	9.021 T
$wind_{build}$	radial build of the conductor winding pack	245.1 mm
$w_{intherm}$	total width of cold to warm thermal isolation, inside leg	20 mm
$w_{outtherm}$	total width of cold to warm thermal isolation, outside case wall	20 mm
t_{incase}	thickness of the inner case winding bobbin	14.55 mm
$t_{outcase}$	thickness of the outer case closure ring	29.10 mm
$t_{sidecase}$	thickness of the case side walls	29.10 mm
w_{wind}	width of the winding pack	184.1 mm
$r_{wpboreav}$	average bore radius of the winding pack	664.4 mm
$r_{inwpboretf}$	inner clear bore of the winding pack	520.0 mm
$r_{inmagnet}$	inner clear bore of the magnet can or dewar	500.0 mm
$r_{outcasebore}$	outer bore of the structural case	808.7 mm
δr_{casein}	inside radial build of the structural case	245.1 mm
δR_{case}	radial build of the structural case	288.7 mm
$R_{tfmagbore}$	major radius of the axis of the TF magnet bore	2.199 m
R_{minwp}	smallest major radius of the conductor winding pack	1.434 m
R_{bmaxtf}	maximum field radius of the magnet	1.679 m
R_{1dewar}	major radius of the high field side of the can or dewar	1.714 m
R_{2dewar}	major radius of inside of outer leg of can or dewar	2.714 m

Table 8.1-1

DIMENSIONS OF THE SUPERCONDUCTING TF MAGNET SYSTEM (continued)

A_{sc}	area of superconductor required in a coil	0.0044 m^2
A_{cu}	area of copper required in a coil	0.02987 m^2
A_{ins}	area of insulation required in a coil	0.0054 m^2
A_{case}	area of the structural case	0.02484 m^2
A_{coil}	total area of the winding pack and structural case	0.070 m^2
A_{heins}	area of helium and insulation required in a coil	0.0108 m^2
A_{wp}	total area of the winding pack, including ground insulation	0.0451 m^2
J_c	noncopper critical current density	56.02 kA/cm^2
A_{cucond}	copper area of a conductor	1.197 cm^2
$A_{noncucon}$	noncoppper area of a conductor	0.673 cm^2
t_{gaptf}	clearance gap between TF coils at the equator	231.6 mm
D_{port}	maximum inside diameter of port between the TF coils at the equator	180 mm
V_{vac}	volume evacuated by the main vacuum pumps	17.46 m^3
A_{outgas}	area of steel outgassing into the plasma	191.5 m^2
I_{cond}	conductor current	22.28 kA
$n_{dpancakes}$	number of double pancakes in a winding	40
n_{layers}	number of layers in a pancake	11
n_{turns}	number of turns in a winding	88
L_{scnew}	total length of new superconductor in the TF system	13.22 km
L_{sctf}	total length of superconductor in the TF system	13.22 km
NI_{mtf}	total number of ampere-meters in the TF system	294.6 MA-m

Table 8.1-II

INTERNALLY COOLED CABLED SUPERCONDUCTOR SPECIFICATIONS

$sctype$	superconductor type	Nb_3Sn ()
f_{He}	helium fraction of the inside cross-section	0.400
$Cu - noncu$	copper/noncopper ratio of a superconducting composite strand	1.700
$Scnon$	superconductor/noncopper ratio	0.200
$A_{noncucond}$	noncopper area of the cable	67.33 mm^2
A_{sccond}	cross-section area of superconductor in a cable	15.49 mm^2
A_{in}	inside cross-section, available for helium and conductor	282.7 mm^2
t_{jack}	jacket thickness	1.730 mm
w_{ojack}	outside jacket width	20.80 mm
D_o	strand diameter	700.0 μm
D_{br}	bronze diameter	420.0 μm
L_{pf}	filament twist pitch length	25.40 mm
L_{pcable}	cable twist pitch length	305.0 mm
n_{fil}	number of filaments in a strand	2869
N_{stran}	number of strands	486
P_w	wetted perimeter of the cable and conduit	1.137 m
ρ_{jak}	jacket resistivity	500.0 n$\Omega - m$
ρ_{noncu}	resistivity of the noncopper/nonsuperconductor	50 nΩ-m
R_{stran}	radius of a strand	350.0 μm
RRR	residual resistivity ratio of the matrix	75

Table 8.1-III

Pulsed Losses in the TF Magnet System

$L_{hystrav}$	average transverse field hysteresis loss/length	63.5 mJ/m
$L_{hyspaav}$	parallel field hysteresis loss/length	36.1 mJ/m
$L_{edparav}$	eddy loss/length, parallel field,	2.30 mJ/m
$L_{edtranav}$	eddy loss/length due to transverse field	714 μJ/m
$L_{couparav}$	coupling loss/length, parallel field,.	155 mJ/m
$L_{coutranav}$	average loss/unit length due to transverse coupling	111 mJ/m
L_{totav}	average loss/unit length in the conductor	369 mJ/m
L_{cascav}	average loss/unit length in the case	21.9 J/m
η_t	efficiency of field penetration	99.3 (%)
P_{scav}	average volumetric loss in the metal	1.97 mJ/cm^3
$P_{scvworst}$	worst case energy deposition in the metal, start-up	3.89 mJ/cm^3
$P_{dis,worst}$	worst case energy deposition in the metal, disruption	29.2 mJ/cm^3
Q	surface heat flux required to remove the pulsed losses	130 mW/cm^2
L_{turnt}	loss/turn in the conductor,	1.49 J
$L_{hyspadisav}$	average parallel hysteresis loss/length due to disruption	18.0 mJ/m
$L_{hystrdisav}$	average transverse hysteresis loss/length due to disruption	12.19 mJ/m
$L_{edparavdis}$	average loss/length from parallel field eddy currents, due to disruption	202 mJ/m
$L_{edtranavdis}$	average loss/length from transverse field eddy currents, due to disruption	27.18 mJ/m
$L_{coutranavdis}$	average transverse coupling loss/length, due to to disruption	1.43 J/m
$L_{couparavdis}$	average parallel coupling loss/unit length in the conductor	155 mJ/m
$L_{totavdis}$	average total loss per unit length on disruption	1.76 J/m
E_{coil}	loss/coil per pulse	131 J
$E_{syswind}$	loss in all the system's windings per pulse	4.71 kJ
$E_{syscasc}$	system case losses per pulse	3.18 kJ
E_{sys}	system loss per pulse	7.90 kJ
$E_{casedis}$	case loss due to a disruption	7.91 kJ
E_{sysdis}	winding pack system loss due to a disruption	307 kJ
$E_{sysrampdis}$	winding pack system loss due to a ramp followed by a disruption	312 kJ
$M_{heboiloff}$	system helium boil-off per pulse	395 g
$M_{heboiloffdis}$	system helium boil-off on disruption	15.6 kg
P_{cond}	average system power in the conductors	15.7 W
P_{cases}	average system power in the cases,	10.6 W
P_{avsys}	average system power requirement	26.3 W

Table 8.1-IV

ENERGY BALANCE TERMS: TF SUPERCONDUCTOR

$sctype$	superconductor material type	Nb3Sn ()
A_{noncu}	superconductor noncopper area	67.3 mm^2
A_{cu}	copper area of the conductor	119.7 mm^2
B_t	magnetic flux density	9.021 T
T_b	bath temperature	4.200 K
T_{cN3Sn}	zero-current critical temperature of Nb_3Sn	10.01 K
T_{cNb3Sn}	current sharing temperature in Nb_3Sn	5.943 K
ρ_{cu}	resistivity of copper at the specified field	933.7 pOhm-m
P_{lTc}	power dissipation per unit length at the critical temperature	115.7 kW/m
Q_{pp}	heat flux per unit area into the helium on quench	101.8 kW/m^2
k_{cuBT}	thermal conductivity of copper at design temperature and field	110.2 W/m-K
R_g	radius of the minimum propagating zone	8.509 mm
$v_{adiabatic}$	adiabiatic longitudinal propagating velocity of a quench	10.89 m/s
v_{qlong}	longitudinal propagation velocity of a quench, with cooling,	4.700 m/s
q	total heat transferred by nucleate boiling during film establishment	8.640 J/m
t_{adiacs}	metal enthalpy to current sharing divided by power/length	2.965 μs
t_{adiac}	metal enthalpy to critical temperature divided by power/length	26.59 μs
t_{isocs}	bath enthalpy to current sharing divided by the power per length	2.500 ms
t_{heatTf}	characteristic time to heat the copper to final temperature	3.035 s

Table 8.1-V

SUPERCONDUCTOR ENTHALPY MARGINS: TF MAGNETS

ΔH_{cubcsl}	bath to current sharing copper energy/length	288.3 mJ/m
ΔH_{nonbcs}	bath to current sharing change in enthalpy in noncopper	631.8 mJ/kg
$\Delta H_{nonbcsl}$	bath to current sharing energy/length absorbed by noncopper	54.80 mJ/m
$\Delta H_{metalbcsl}$	total bath to current sharing energy/length absorbed by metal	343.1 mJ/m
ΔH_{hebcsl}	bath to current sharing change in enthalpy/length in helium	76.03 J/m
ΔH_{bcsl}	enthalpy/length to raise entire conductor to current sharing temperature	76.37 J/m
$\Delta H_{metalbcsv}$	total bath to current sharing energy/volume of metal absorbed by metal	2.538 mJ/cm^3
ΔH_{bcsv}	total bath to current sharing energy/volume of metal	564.9 mJ/cm^3
ΔH_{cu}	change in copper enthalpy between bath and critical temperature	2.266 J/kg
ΔH_{cul}	enthalpy/length to raise the copper to the critical temperature	2.414 J/m
ΔH_{nonbc}	bath to critical change in enthalpy in the noncopper	7.650 J/kg
ΔH_{nonbcl}	bath to critical energy/length absorbed by the noncopper	663.4 mJ/m
ΔH_{hebc}	bath to critical change in enthalpy in the helium	35.14 kJ/kg
ΔH_{hebcl}	bath to critical change in enthalpy/length in the helium	286.3 J/m
ΔH_{bcl}	enthalpy/length to raise the entire conductor to the critical temperature	289.4 J/m
$\Delta H_{metalbcv}$	total bath to current sharing energy/volume of metal absorbed by metal	22.77 mJ/cm^3
ΔH_{bcv}	total bath to current sharing energy/volume of metal	2.141 J/cm^3
ΔH_{10bo}	10 % helium boil off energy/volume of metal	120.5 mJ/cm^3

8.1-VI CIRCULAR SUPERCONDUCTING TF MAGNET SYSTEM

N_{par}	actual number of parallel discharge circuits	20
N_{leads}	number of discharge leads	40
N_{series}	total number of series magnets, during discharge,	18
W_{mtf}	magnetic stored energy of the toroidal magnet system	369.0 MJ
F_z	total vertical force on the upper half of the magnet system	329.7 MN
F_r	total centering force on the toroidal magnet system	-177.8 MN
F_z	total vertical force on a magnet	9.159 MN
F_r	total radial force on a magnet	-4.940 MN

Table 8.2-1

S_m is defined as the lesser of 2/3 yield strength or 1/3 ultimate strength at operating temperature.

Stress Parameter	Ratio	Material Parameter
Primary membrane stress intensity	< 1	S_m
Primary membrane plus bending	< 1.5	S_m
Average shear stress	< 0.6	S_m, metals
Average shear stress	$< 1/3$	ultimate shear strength, nonmetals
Compressive stress	< 0.2	elastic buckling stress

Each of the above limits is multiplied by 1.5 for abnormal conditions, such as 1 coil disabled.

Appendix 8.A

8.A.1 The Desirability of Circular Superconducting Magnets

Circular magnets have always been the easiest to wind and the easiest to weld, as well as the easiest to analyze and understand. They have been used in PLT and will be used in TFTR and JT-60. They have been used in the small superconducting tokamak T-7, and have been proposed for use in the large superconducting experiment TORE SUPRA, as well as high aspect ratio toroidal devices such as EBT-P. However, to the best of our knowledge, they have never been proposed for use in a tokamak reactor or large tokamak test facility. There are three principal reasons for this:

1 The mistaken assumption that superconducting magnets have no strength in bending has led to a quest for optimizing the magnet shape, most popularly with the so-called constant-tension D. We will argue below that shape optimization, driven by the minimization of in-plane bending, is an unnecessary and harmful concept.

2 Small improvements in overall plasma beta, although not in the overall mass of the toroidal and poloidal coil systems, have been theoretically predicted, and not yet experimentally confirmed, for strongly D-shaped plasmas. The natural harmony of combining D-shaped coils with D-shaped plasmas was irresistible when plasma designers believed that magnet designers required a D and vice-versa.

3 Cylindrical bucking cylinders have been easier to design for some designers than a system of rings or intercoil wedging.

4 Because of the large available space, many designs introduce topological complications, such as poloidal divertors, internal poloidal field coils and high-side ECRH injection to the tokamak system. The space available under the soaring arches of the so-called constant tension D shape then becomes necessary and appears to be unwasted.

The argument in Bobrov's anisotropic, thick toroidal shell analysis [BO81] [BO82] that shape optimization is unnecessary is repeated below.

8.A.2 TF Magnet Shape Optimization: Background

The history of shape optimization for tokamak reactors sometimes appears to begin and end with the discovery by researchers at Princeton [FI71] that filaments in pure tension, subjected to a $1/r^2$ force field, and supported against inward centering forces by a stiff cylinder, would take on the now familiar "constant-tension" D shape. Following this observation, almost every tokamak reactor study has utilized this shape. When perturbations on this shape have been selected [LU77], they are generally accompanied by apologia justifying the deviation. Some theoretical modifications of the concept which have appeared include the analytical solution to the bending stresses induced because the filaments have finite thickness [WE77], perturbations to the shape because of the nonuniform toroidal field of a finite number of coils [MO75], and the effect of finite compliance in the bucking post on the optimum shape [OJ79].

An obvious deficiency in using a filament model to derive an optimum shape is that the presence of intercoil structure to support out-of-plane loads introduces circumferential force terms into the equilibrium equations, as was first analyzed by Gray et al [GR81]. Specifically, the equations of equilibirium for an axisymmetric shell of revolution loaded normally to the middle surface are:

$$\frac{dT_1}{ds} + \frac{1}{r}\frac{dr}{ds}(T_1 - T_2) + \frac{Q}{R_1} = 0 \tag{8.A.1}$$

$$-\frac{T_1}{R_1} - \frac{T_2}{R_2} + \frac{dQ}{ds} + \frac{1}{r}\frac{dr}{ds}Q = -q \tag{8.A.2}$$

and

$$-Q + \frac{dG_1}{ds} + \frac{1}{r}\frac{dr}{ds}(G_1 - G_s) = 0 \tag{8.A.3}$$

where T_1 and T_2 are the meridional (poloidal) and circumferential (toroidal) stress resultants, Q is the shear stress resultant, G_1 and G_2 are the meridional and circumferential stress couples, R_1 and R_2 are the radii of curvature, r is the radius of the hoop circle, s is the meridional coordinate, and q is the normal pressure. The terms with T_2 in equations (8.A.1) and (8.A.2) are neglected in the filamentary model, but included in Gray's model. The Bobrov model also includes Q, the shear stress resultant [BO81]. Gray's analysis showed that the inclusion of intercoil structure to support out-of-plane stresses would define a zero-bending shell shape which could have a significantly smaller perimeter and much less triangularity than the constant-tension filament shape. Unlike the significant shape deviations described by Ojalvo [OJ79] or Welch [WE75], the deviation from the D happened automatically, without deliberately adding reaction forces in what might be inaccessible places. Furthermore, the existence of a zero-bending shell shape suggested that real magnets, such as the LCP coils, which followed the so-called "constant-tension" D trajectory, might have large bending stresses due to the inevitable reaction forces in the intercoil structure. In many ways, the zero-bending shell is just as idealized as the constant-tension D. The D filament model ignores all intercoil structure, while the constant thickness shell ignores deviations from constant thickness and models current as being toroidally uniform, which is only a good approximaton for magnets with Bitter plate construction. In addition, there is an inherent strain incompatibility at the crown of a "zero-bending" toroidal shell, described by membrane theory, which can be eliminated by including bending. Stated differently, the greatest weakness of both idealizations is that the magnet structures are negligibly thick or have negligible moments of inertia, and thus must of necessity be bending free.

The existence of TF coils in the tokamak program of all shapes and sizes raises a more fundamental question about shape optimization, which is whether shape optimization based on the elimination of bending moments is a valid design criterion at all. The implicit assumption behind this method is that superconducting, pool-boiling magnets are so flimsy against in-plane stresses that only negligible bending moments are permitted. While it appears obvious that a pool-boiling coil cannot have the stiffness of a potted coil in the same case, it is unclear on first principles whether the stiffness limitations of this technology dominate shape selection. The operational Russian superconducting tokamak T-7 uses circular TF coils, as does the conceptual design of the French Tore Supra [AY80]. Hooper [FL81] calculated that the case thicknesses of the TF coils for the Fusion Engineering Device were determined entirely by out-of-plane loads.

8.B.2 Bobrov's Results

Bobrov's thick shell analysis allowed the analytical determination of stress in shapes which have non-zero bending. Using the example of the Fusion Engineering Device design of 1981, he addressed the question of whether bending stresses are dominant for realistic case thicknesses and significant deviations from "zero-bending" shapes.

The meridian shapes selected as examples were a circle and the "bending free" shell of Gray et al [GR81]. Both shells have dimensions of the toroidal field coils in the 1981 Fusion Engineering Device (FED) described in [FL81], i.e., r_{in} = 2.14 m, r_{out} = 10.5 m, NI = 115 MAT, effective shell thickness h = 0.66 m and a coil case thickness 0.08 m. Figure 8.B.2.1 shows the meridians of the circular and "bending free" shells analyzed, along with that of a Princeton D. These analyses were performed twice [BO81] [BO82], with the more sophisticated model [BO82] including out-of-plane forces and discrete currents in the shell.

The results of the latter analysis are presented in Fig. 8.B.2.2 and Fig. 8.B.2.3. Figure 8.B.2.2 shows the distribution of the effective meridional and circumferential membrane stresses in the coils and intercoil structures of both shapes. The effective meridional and circumferential bending stresses in the extreme fibers of the structural elements are as shown in Fig. 8.B.2.3. For the circular configuration the primary tensile stress at the inner leg at the equator is 151 MPa while the peak bending stress is 54 MPa. For the "bending free" configuration, the primary tensile stress in the inner leg at the equator is 139 MPa, while the peak bending stress is 66 MPa.

This demonstrates that if the finite thickness of the magnet structure is accounted for the "bending free" configuration proposed in [GR81] has bending stresses which are proportionally as large as the bending stresses in the circular configuration.

Since the total upward force on the upper half of the coil system must be

$$F_z = \frac{\mu_o (NI)^2}{4\pi} \ln \frac{r_{out}}{r_{in}} \qquad (39)$$

or 2122 MN, the theoretical minimum tension is 1061 MN in the inner leg, giving an average stress of 120 MPa in an ideal constant tension coil. Thus, the tensile stress in the inner leg at the equator for a circular coil is 1.26 times the theoretical minimum, while the tensile stress for the "bending free" configuration is 1.16 times the theoretical minimum. The primary stress in the "bending free" shape is 8.5 % smaller than that in the circle, while the perimeter of the "bending free" configuration is 18 % greater than that of a circle, implying that the circular configuration requires less mass for a given set of stress allowables.

8.B.3 Discussion

If circular magnets have lower mass than constant tension D or zero-bending shell shaped magnets before out-of-plane forces are considered, there will be no trade-off at all, once they are. The current required in external poloidal field magnets increases more rapidly than r, the poloidal radius, while the moment arm of the out-of-plane forces increases with coil height. Thus, there is a very high power dependence of both torsional moment and poloidal field energy on the height of the toroidal field coil meridian. The ability to drive flux through the narrow reactor center ohmically will improve as the inner legs open up into a circular shape. A ring or wedged support system will allow ohmic and poloidal coils with smaller major radii than the machine supports to the building to be simply removed upward and downward, as proposed by Brown [BR82], with no requirement for joints or displacement of machine structure. The replacement of high arched TF coils with circular coils propagates through the rest of the reactor system in such a dramatic way that it can easily halve the overall mass of a tokamak reactor, as suggested by an earlier reduced straight-leg concept by Brown [BR81] and to be proved by the authors in a subsequent design study. The reduction of the TF coil meridian, far from being an obscure theoretical issue, is probably the only way to significantly reduce the size of a commercial tokamak reactor, along with a solution to the simultaneous radial removal of toroidal field coils and blanket-shield structure, having more importance in our opinion than the improvement of toroidal beta.

References

[AY80] Aymar et al, "TORE SUPRA: Basic Design Tokamak System," Association Euratom-C.E.A. Report EUR-CEA-FC-1068, Oct. 1980

[BO81] E.S. Bobrov and J.H. Schultz, "A model of toroidal magnet systems as orthotropic shells of finite thickness," 9th Symposium on Eng Probs of Fusion Research, Chicago Il, Oct 1981

[BO82] E.S. Bobrov and J.H. Schultz, "Analysis of toroidal magnet systems on the basis of the Reissner Shell Theory," M.I.T. Plasma Fusion Center Journal Article PFC/JA-82-14, Aug 1982, to be published in ASME Pressure Vessel and Piping Division Transactions

[BR81] T.G. Brown, M.H. Kunselman, "Concept for modified FED configuration," Fusion Engineering Design Center Report FEDC-R-81-DC-006, 1981

[BR82] T.G. Brown, Fusion Engineering Design Center, private communication

[FI71] J. File, R.G. Mills, and G.V. Sheffield, "Large Superconducting Magnet Designs for Fusion Reactors," IEEE Trans Nuc Sci, NS-18, p.205, 1971

[FL81] C.A. Flanagan, D. Steiner, G.E. Smith and the Fusion Engineering Design Center Staff,"Initial Trade and Design Studies for the Fusion Engineering Device," Oak Ridge National Laboratory Report ORNL/TM-7777, June 1981

[GR81] W.H. Gray, W.C.T. Stoddart, and J.E. Akin, "A Derivation of Bending Free Toroidal Shell Shapes for Tokamak Fusion Reactors," Jour Appl Mech, Vol. 46, No. 1, Mar 1979

[LU77] J.W. Lue and J.N. Luton, "Toroidal Field Coil System of the Oak Ridge EPR Reference Design," IEEE Trans Magnetics, Vol. MAG-13, NO 1, Jan, 1977

[MO75] R.W. Moses and W.C. Young, "Analytic Expressions for Magnetic Forces on Sectored Toroidal Coils," Proc 6th Symp Eng Probs Fus Res, San Diego, CA, Nov, 1975

[OJ79] I.U. Ojalvo and I.J. Zatz, "Structural Support Design Method for Minimizing In-Plane TF Coil Stresses," Proc 8th Symp Eng Probs Fus Research, San Francisco, CA, Nov 1979

[WE77] D.W. Weissenburger, U.R. Christensen, J. Bialek, "Pure Tension Shape of a Thick Torus," Princeton Plasma Physics Laboratory Report PPPL-1353, Jul 1977

[WE75] C.T. Welch, "Bending-Free Shapes for Toroidal Magnet Field Coils with Concentrated Symmetric Reactions," Proc 6th Symp Eng Probs Fus Res, San Diego, CA, Nov 1975

JHS-83-3151

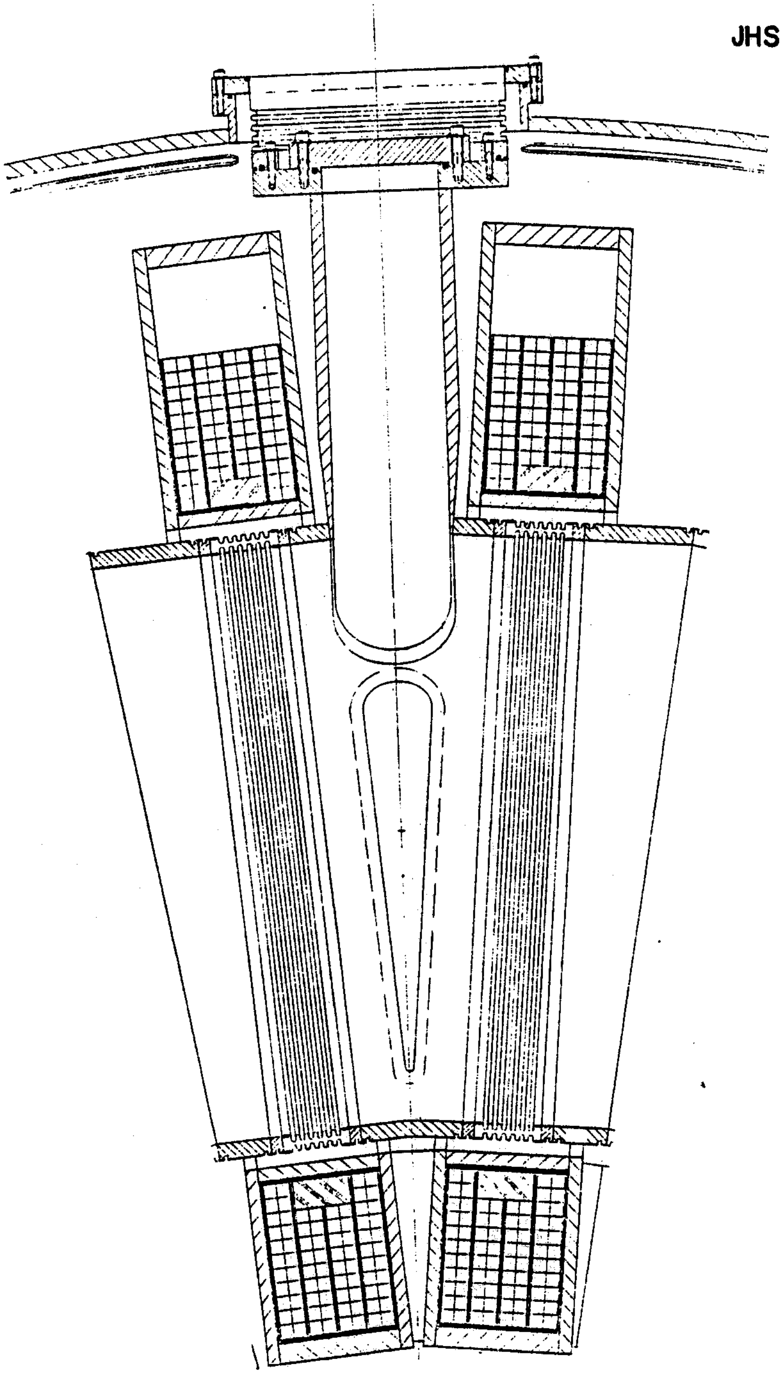

FIGURE 8.1.1
PLAN VIEW OF TOROIDAL FIELD MAGNETS AND VACUUM VESSEL AT THE EQUATORIAL PLANE.

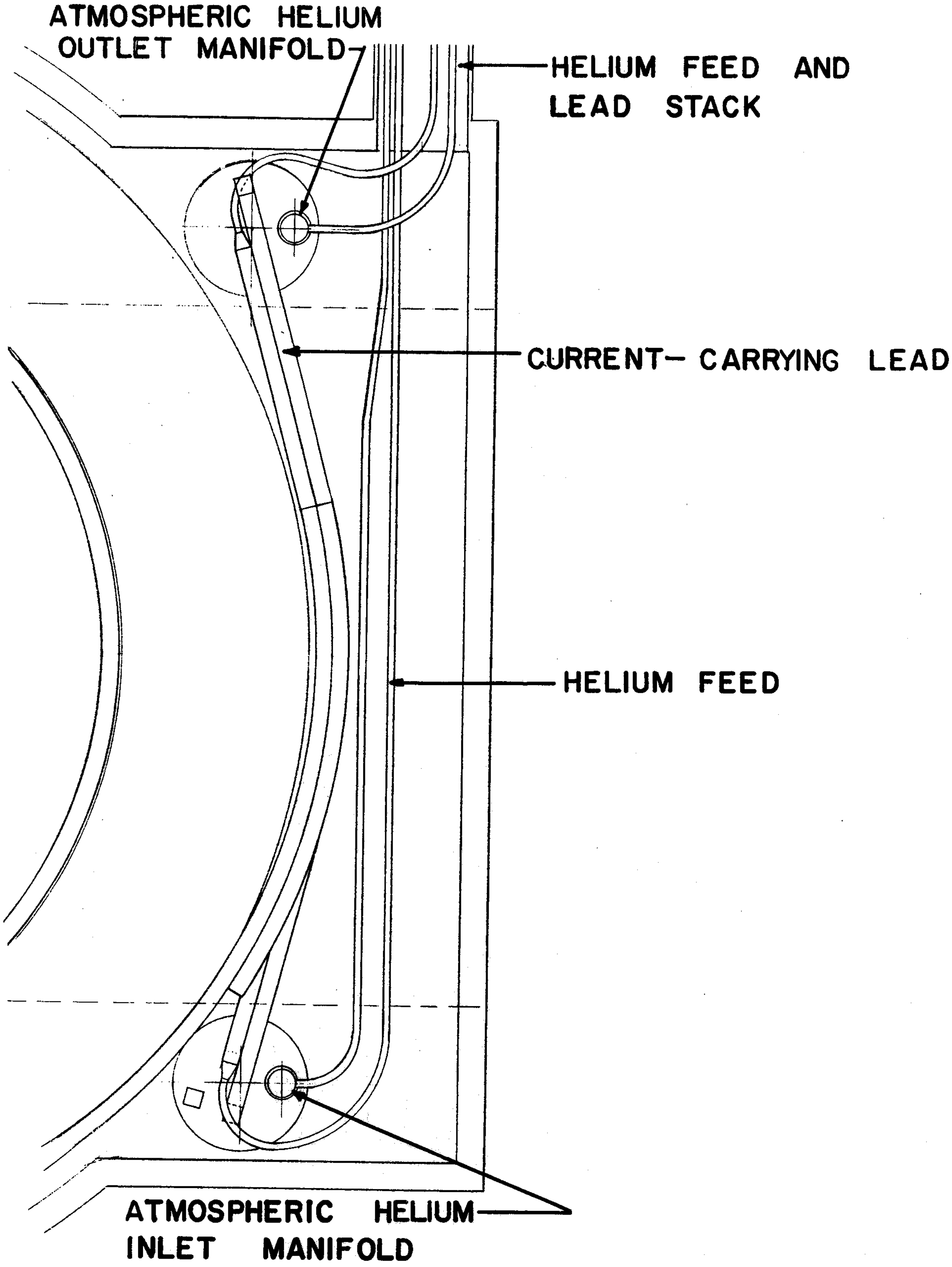

FIGURE 8.1.1.1

TF MAGNET HELIUM MANIFOLDS

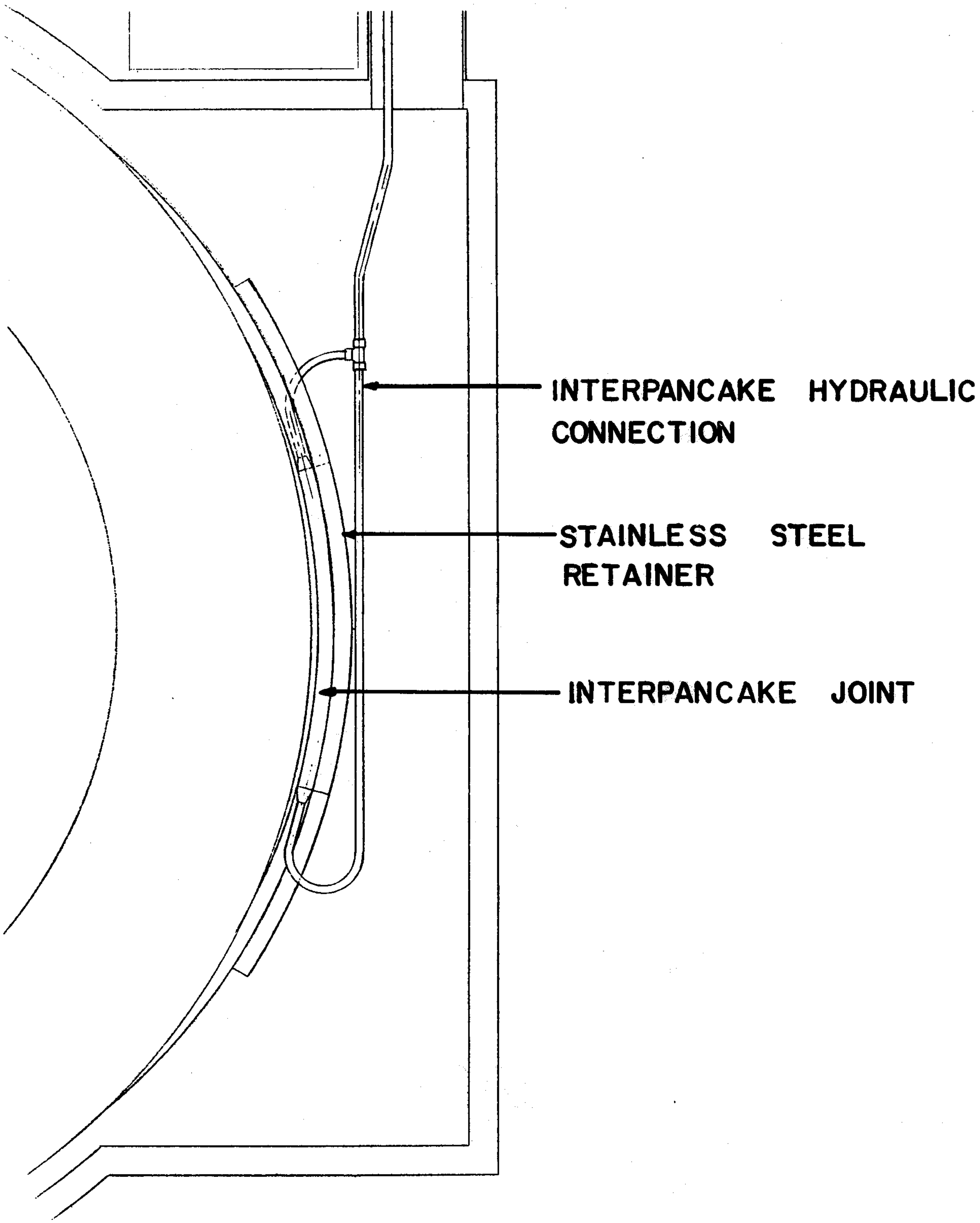

FIGURE 8.1.1.2
TF MAGNET INTERPANCAKE JOINT

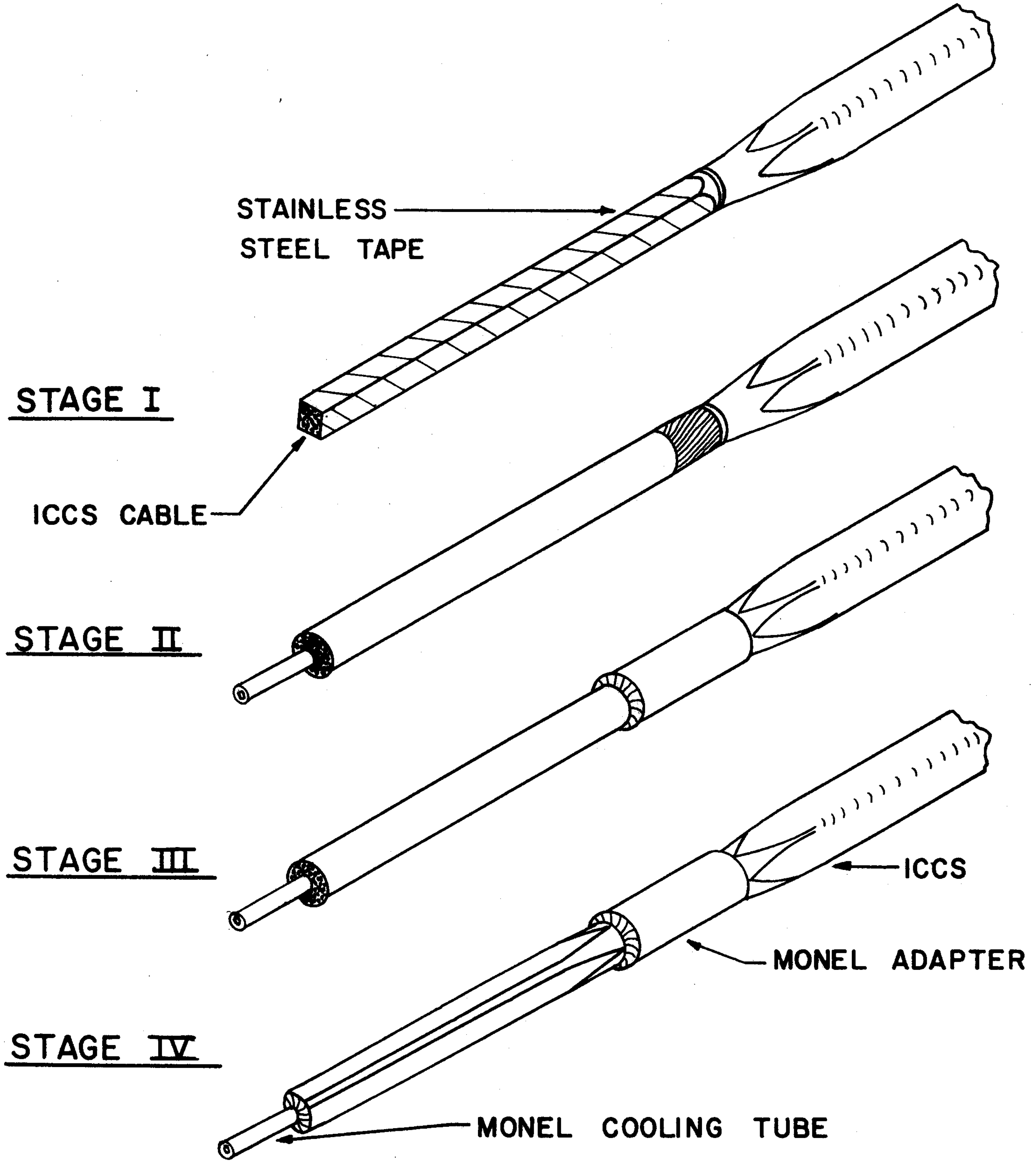

FIGURE 8.1.1.3

STAGES IN THE FABRICATION OF ICCS TERMINATIONS OF THE 12 T PROGRAM (Steeves and Hoenig PFC/RR-82-22)

JHS-83-3152

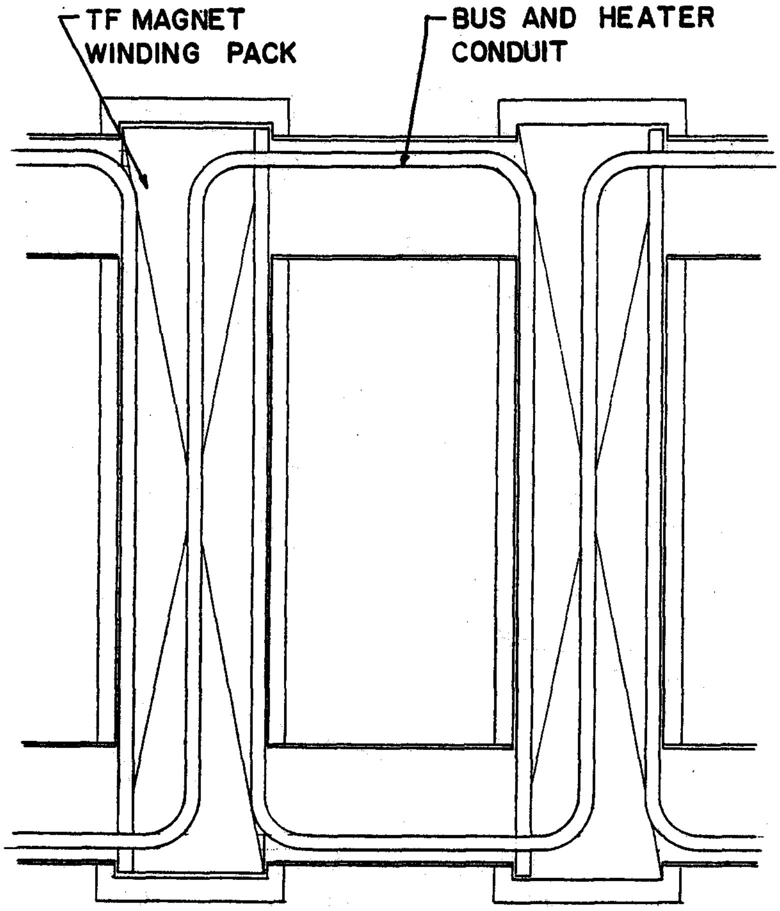

FIGURE 8.1.1.4

TF SYSTEM INTERCOIL BUS AND HELIUM HEATERS.

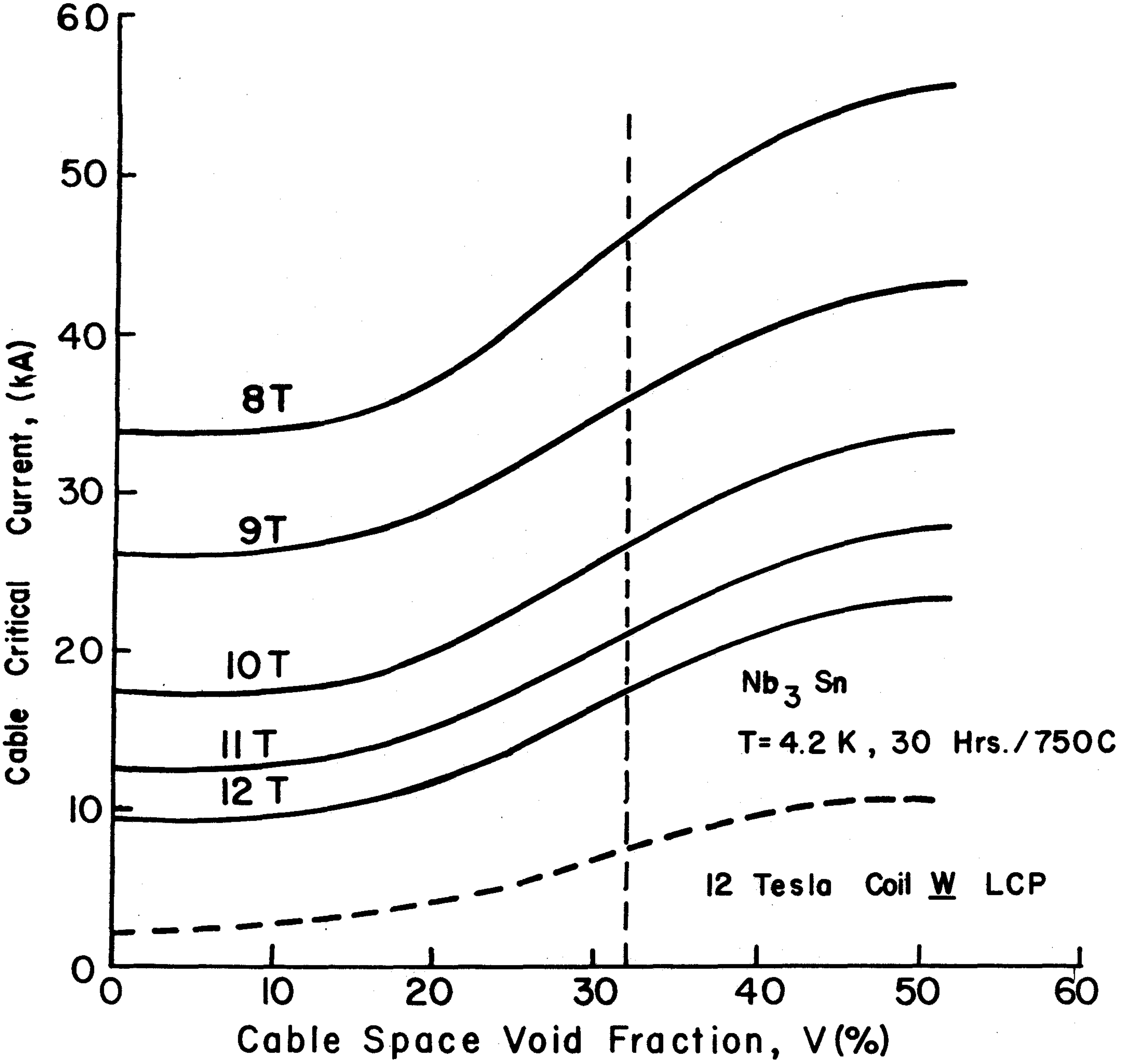

FIGURE 8.1.2.1

Predicted Critical Current as a Function of Cable Space Void Fraction. The cable consists of 486 strands of Airco 0.7 mm Diameter Nb_3Sn wire. Void fraction equals the space available to helium. The data is from conductors reacted at 750°C and tested at 4.2 K. Both the Westinghouse LCP and 12 Tesla Coil conductors have a 32% cable space void fraction. Critical currents were evaluated by an electric field criterion of 1.5 μV/cm.

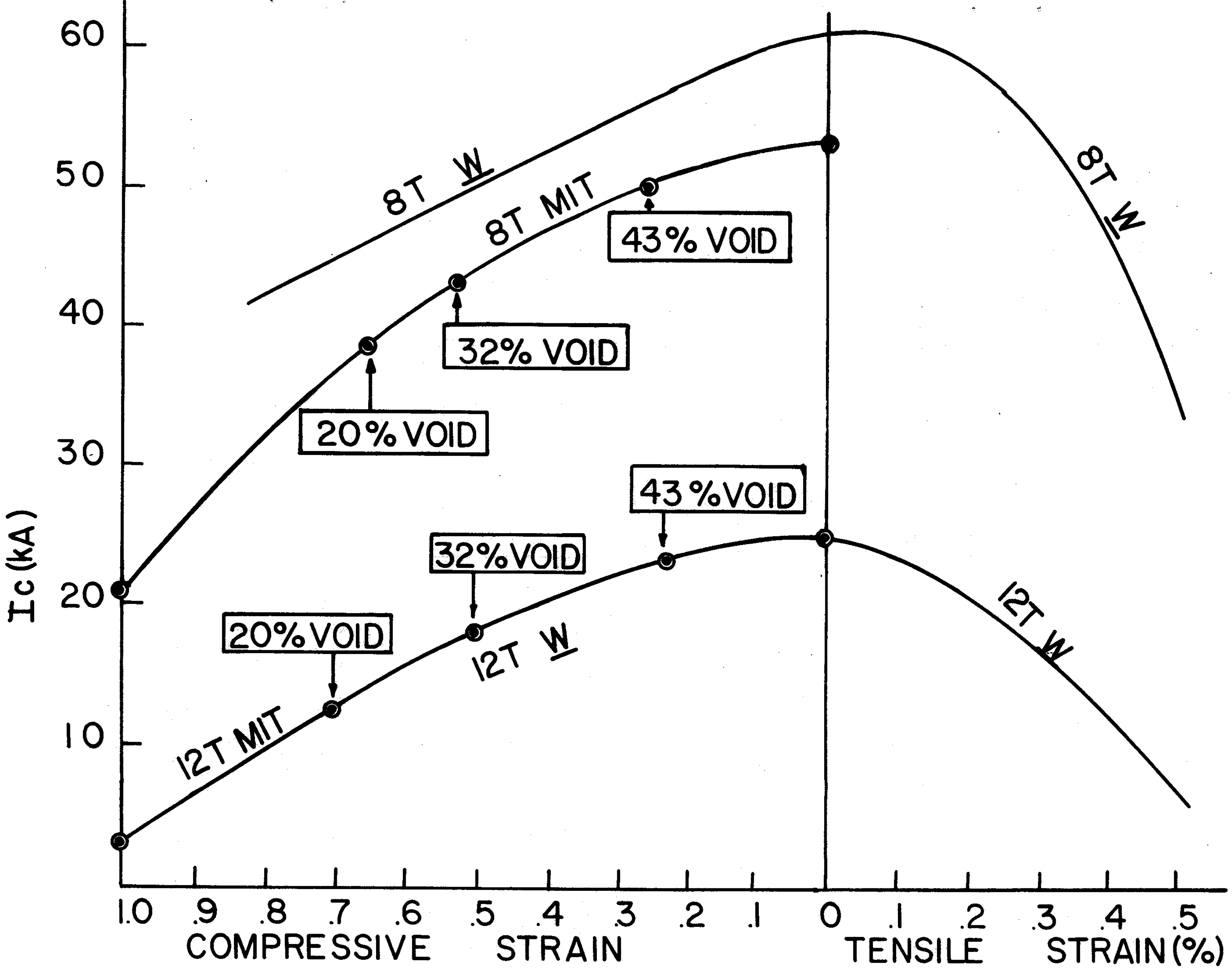

FIGURE 8.1.2.2

LCP(W) Conductor Critical Current Ic vs. Strain at 12 & 8T

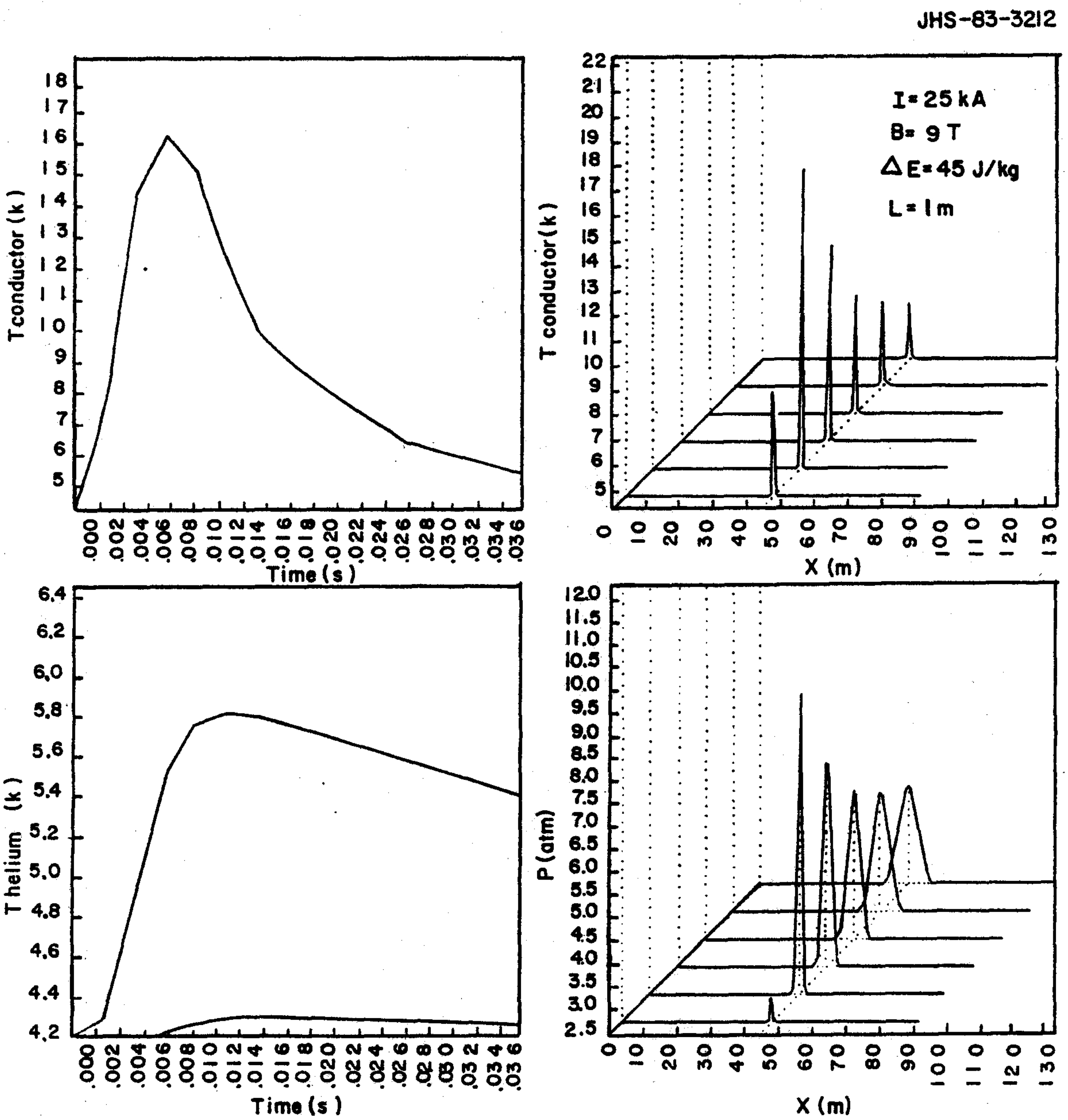

FIGURE 8.1.2.1.1

PRESSURE AND TEMPERATURE VS. POSITION AND TIME FOR TF RECOVERY FROM 45 J/kg ENERGY DEPOSITION OVER 1 m INTO 25 kA CONDUCTOR.

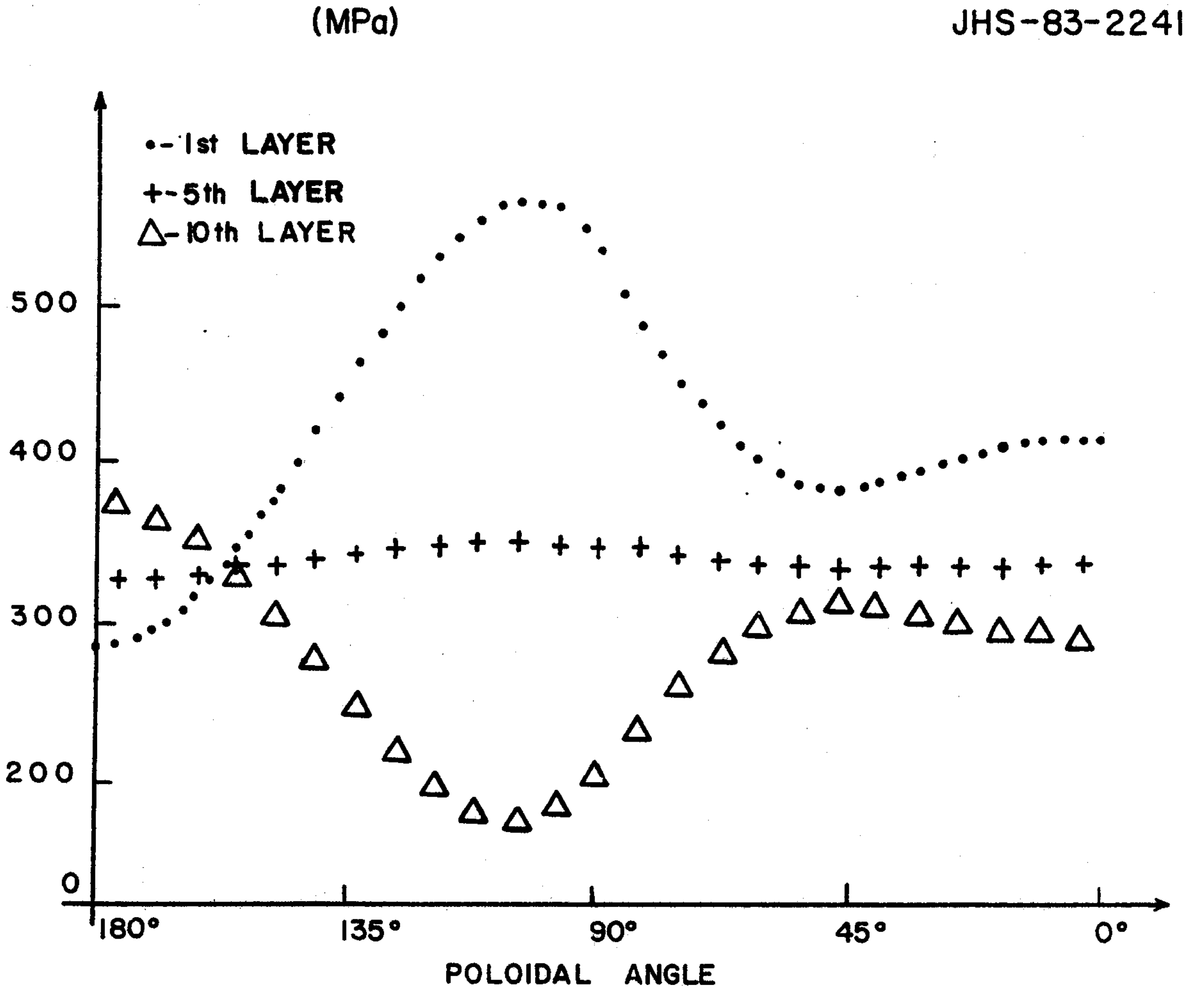

FIGURE 8.2.2.1

PRIMARY POLOIDAL TENSILE STRESS IN THE CONDUCTOR SHEATH VS. POLOIDAL ANGLE FROM THE TF MAGNET BORE, IF COIL IS SUPPORTED FROM INNER BOBBIN WITH NO SLIP BETWEEN CONDUCTOR LAYERS.

PRIMARY POLOIDAL STRESS JHS-83-2242

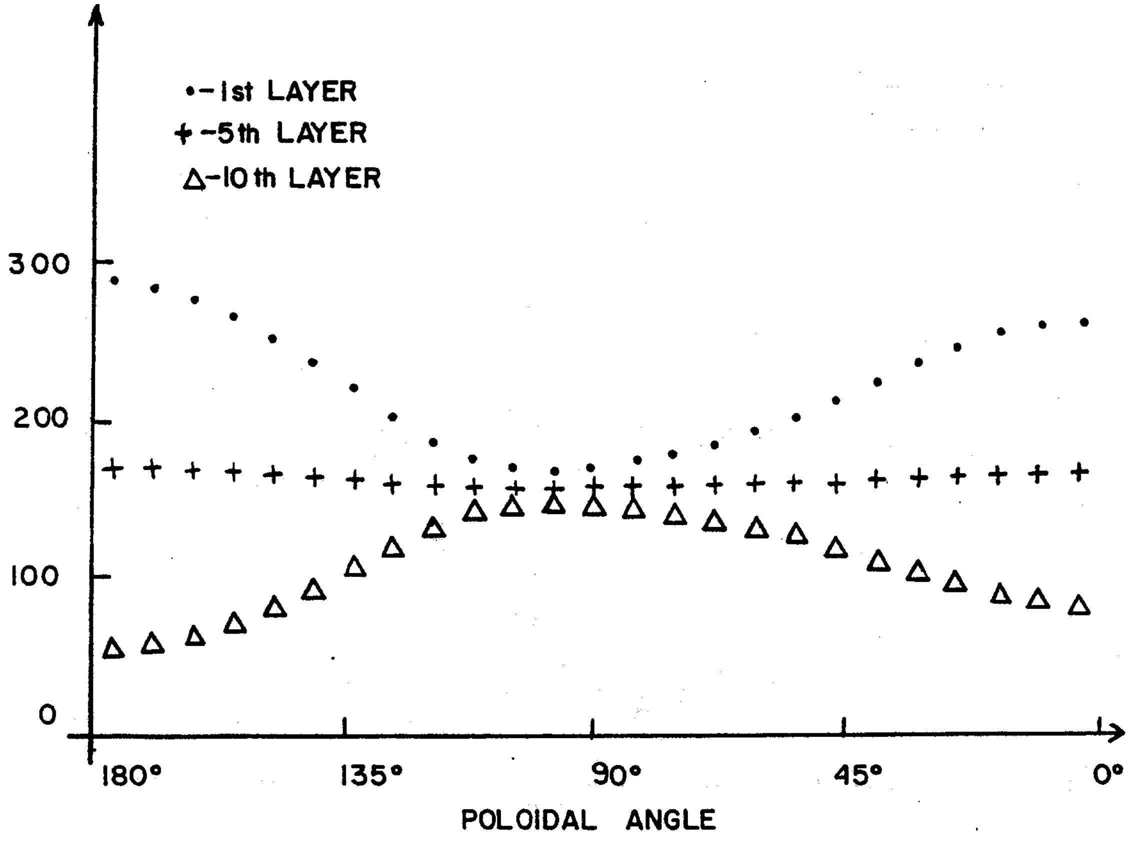

FIGURE 8.2.2.2

PRIMARY POLOIDAL TENSILE STRESS IN THE CONDACTOR SHEATH VS. POLOIDAL ANGLE FROM THE TF MAGNET BORE, IF THE CONDUCTORS ARE SUPPORTED BY THE OUTER CASE AND PERFECTLY BONDED.

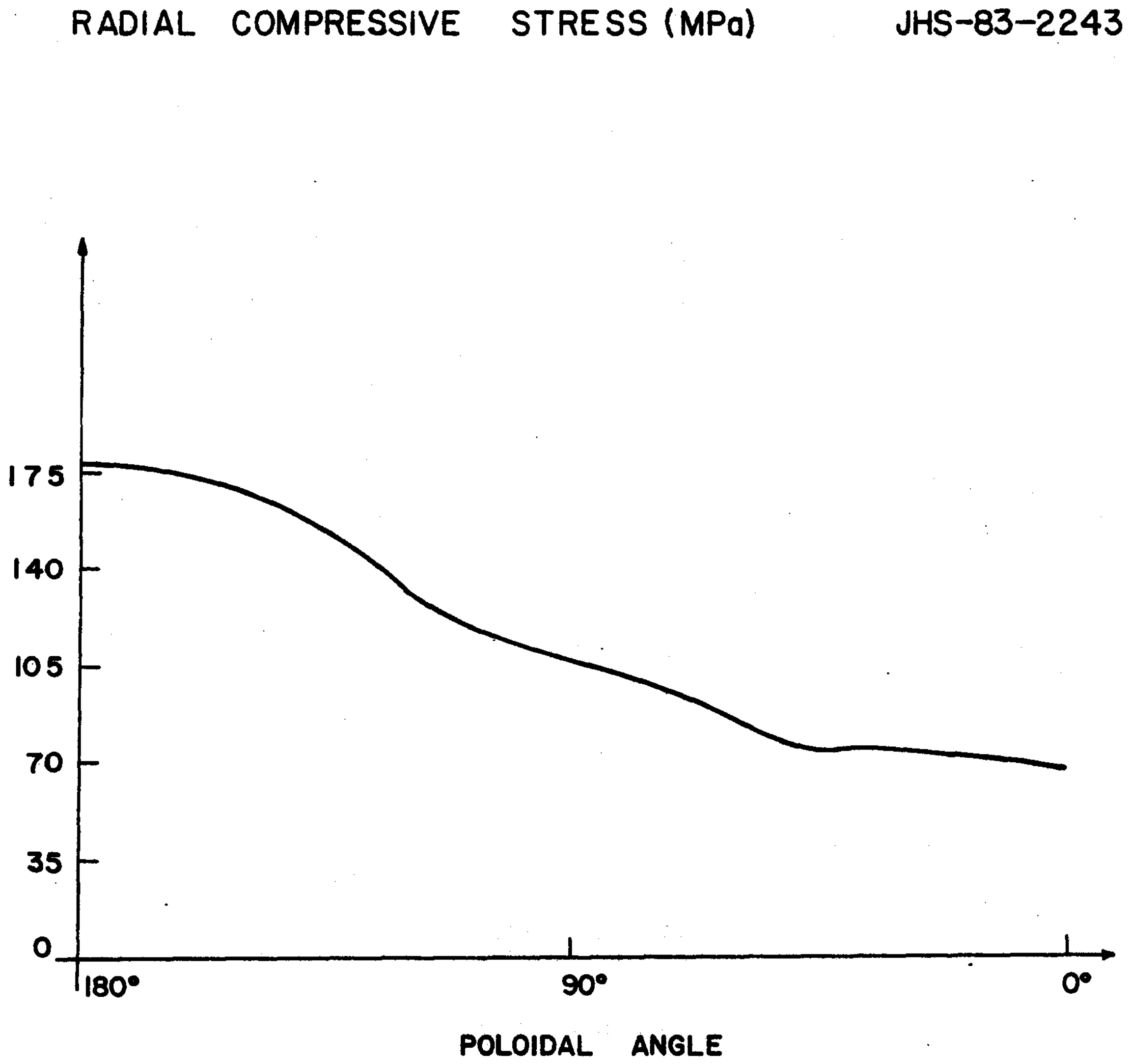

FIGURE 8.2.2.3

PRIMARY RADIAL COMPRESSIVE STRESS IN THE CONDUCTOR SHEATH OF THE TENTH LAYER VS. POLOIDAL ANGLE FROM THE TF MAGNET BORE, IF COIL IS SUPPORTED BY OUTER CASE AND PERFECTLY BONDED.

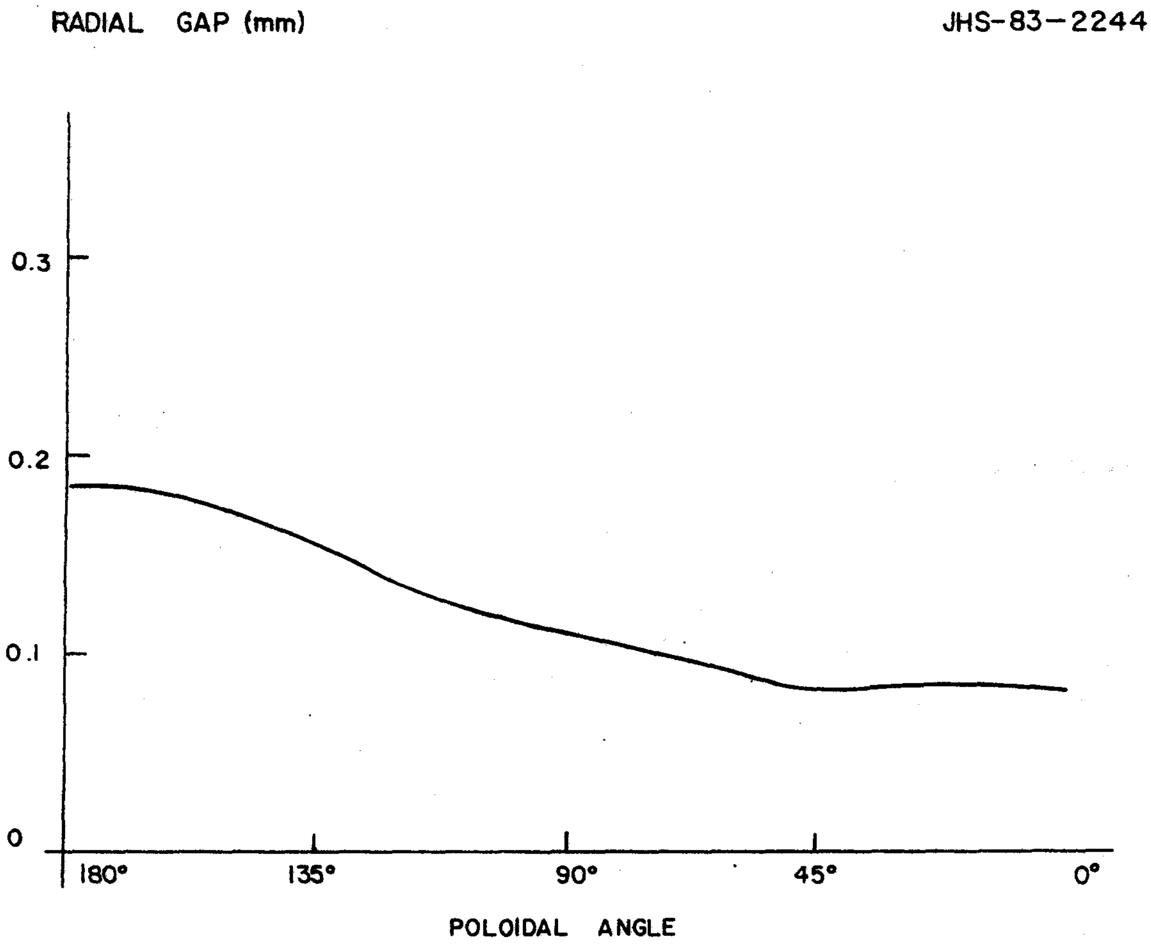

FIGURE 8.2.2.4

RADIAL GAP BETWEEN FIRST LAYER AND INNER BOBBIN VS. POLOIDAL ANGLE FROM TF MAGNET BORE, IF TF COIL IS SUPPORTED BY OUTER CASE AND PERFECTLY BONDED.

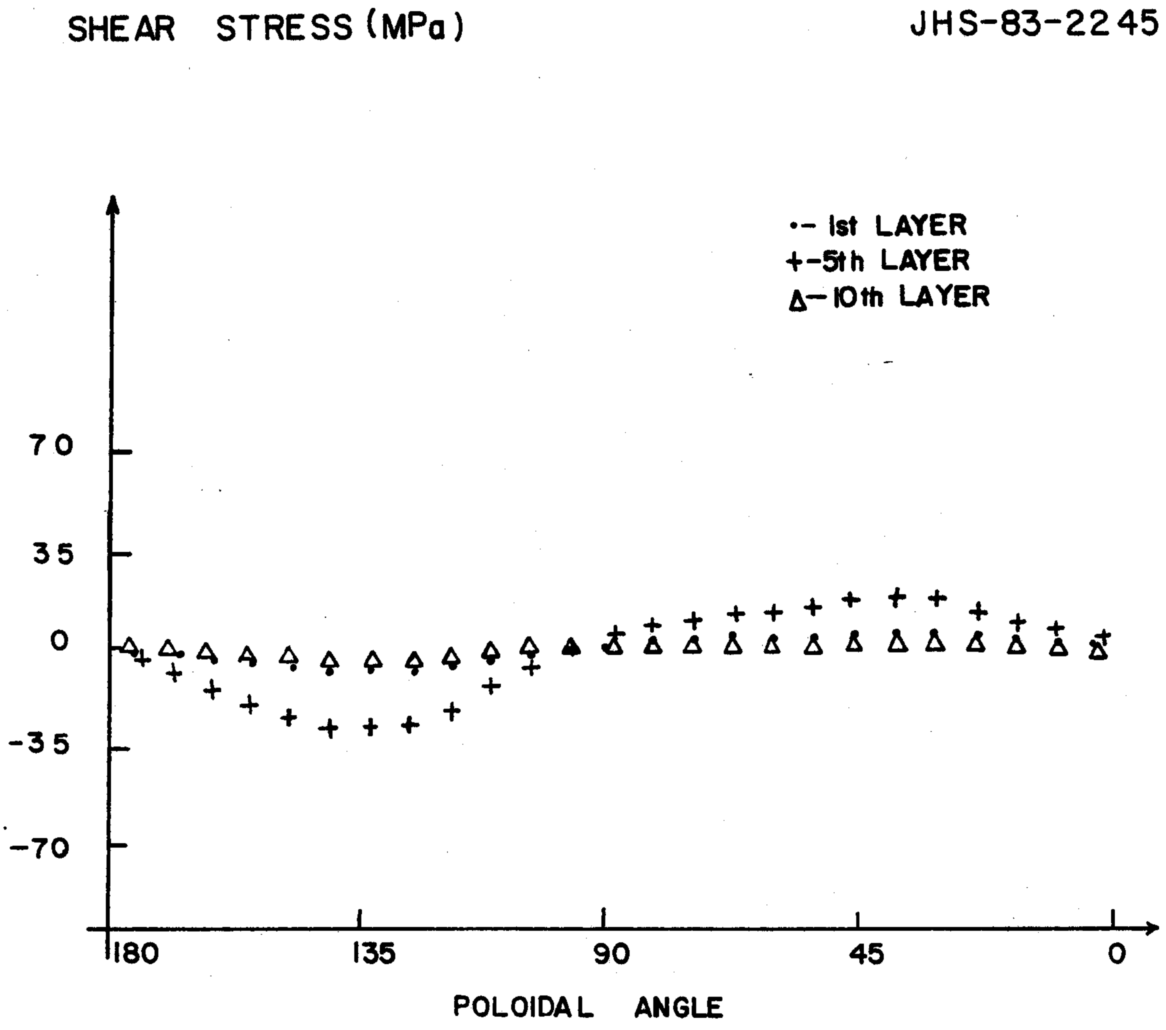

FIGURE 8.2.2.5

SHEAR STRESS IN THE CONDUIT WALLS VS. POLOIDAL ANGLES, IF THE TF COIL IS SUPPORTED BY THE OUTER CASE AND IS PERFECTLY BONDED.

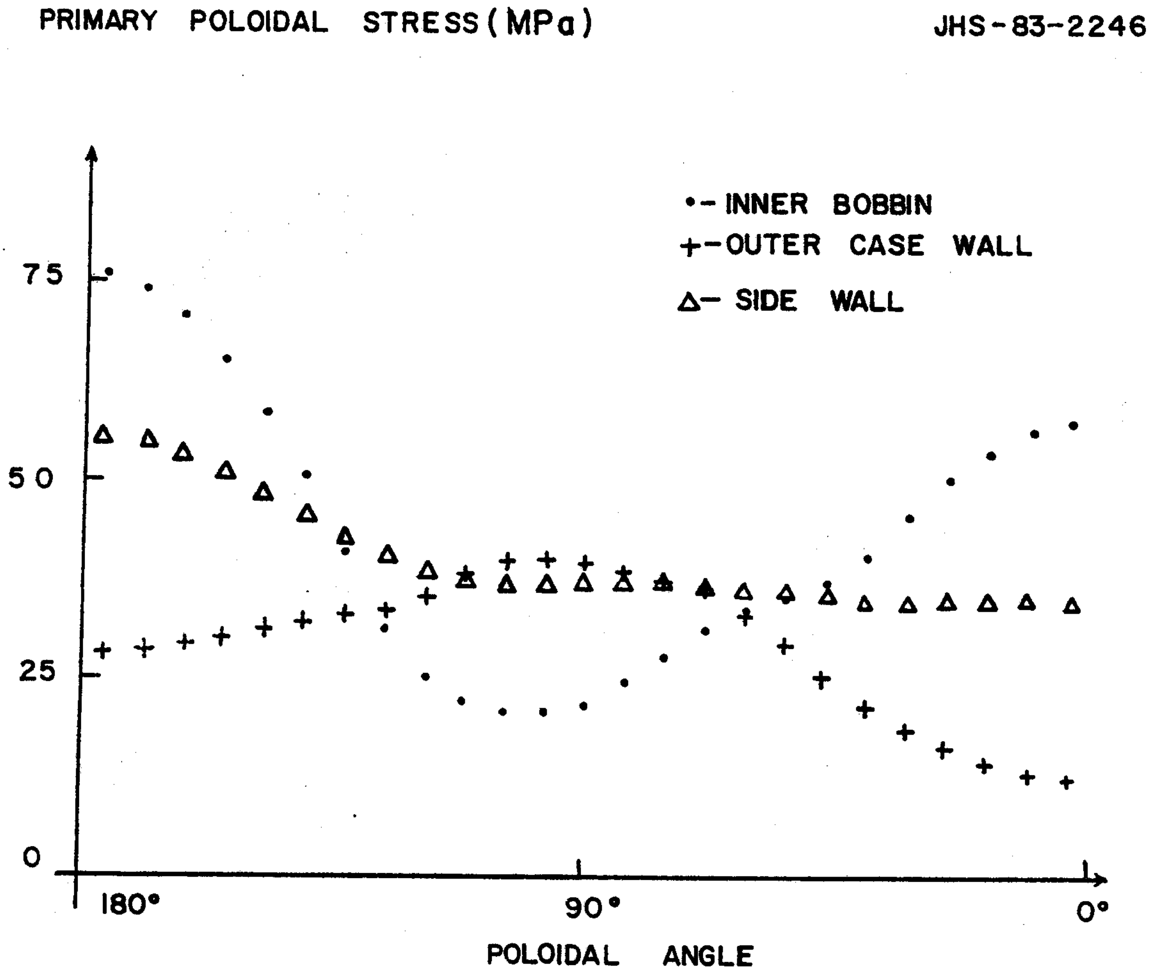

FIGURE 8.2.2.6

PRIMARY POLOIDAL TENSILE STRESS IN INNER, OUTER AND SIDE WALL OF TF COIL COLD CASE VS. POLOIDAL ANGLE, IF CONDUCTORS ARE SUPPORTED BY OUTER WALL AND PERFECTLY BONDED.

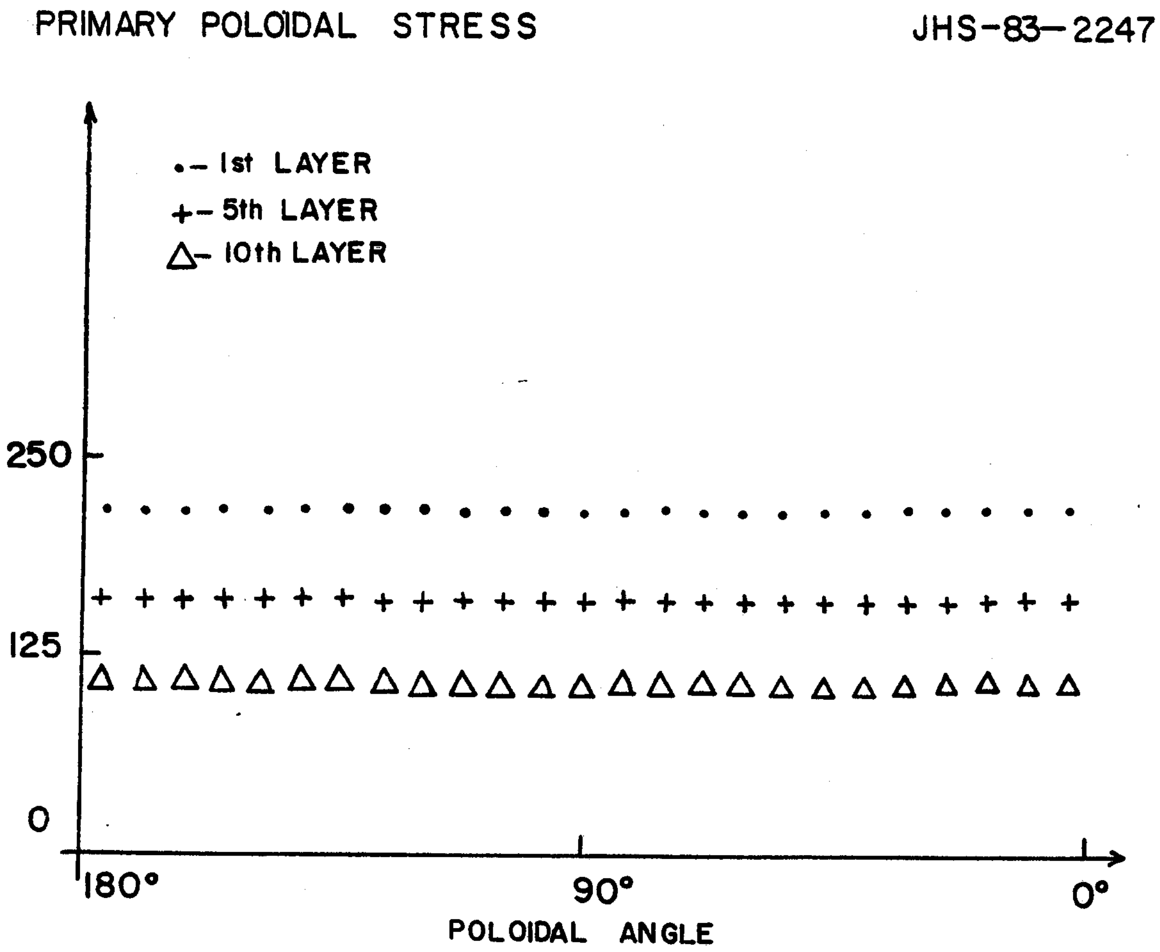

FIGURE 8.2.2.7

PRIMARY POLOIDAL TENSILE STRESS IN THE CONDUCTOR SHEATH VS. POLOIDAL ANGLE FROM THE TF MAGNET BORE IF CONDUCTORS SUPPORTED BY OUTER CASE AND UNBONDED.

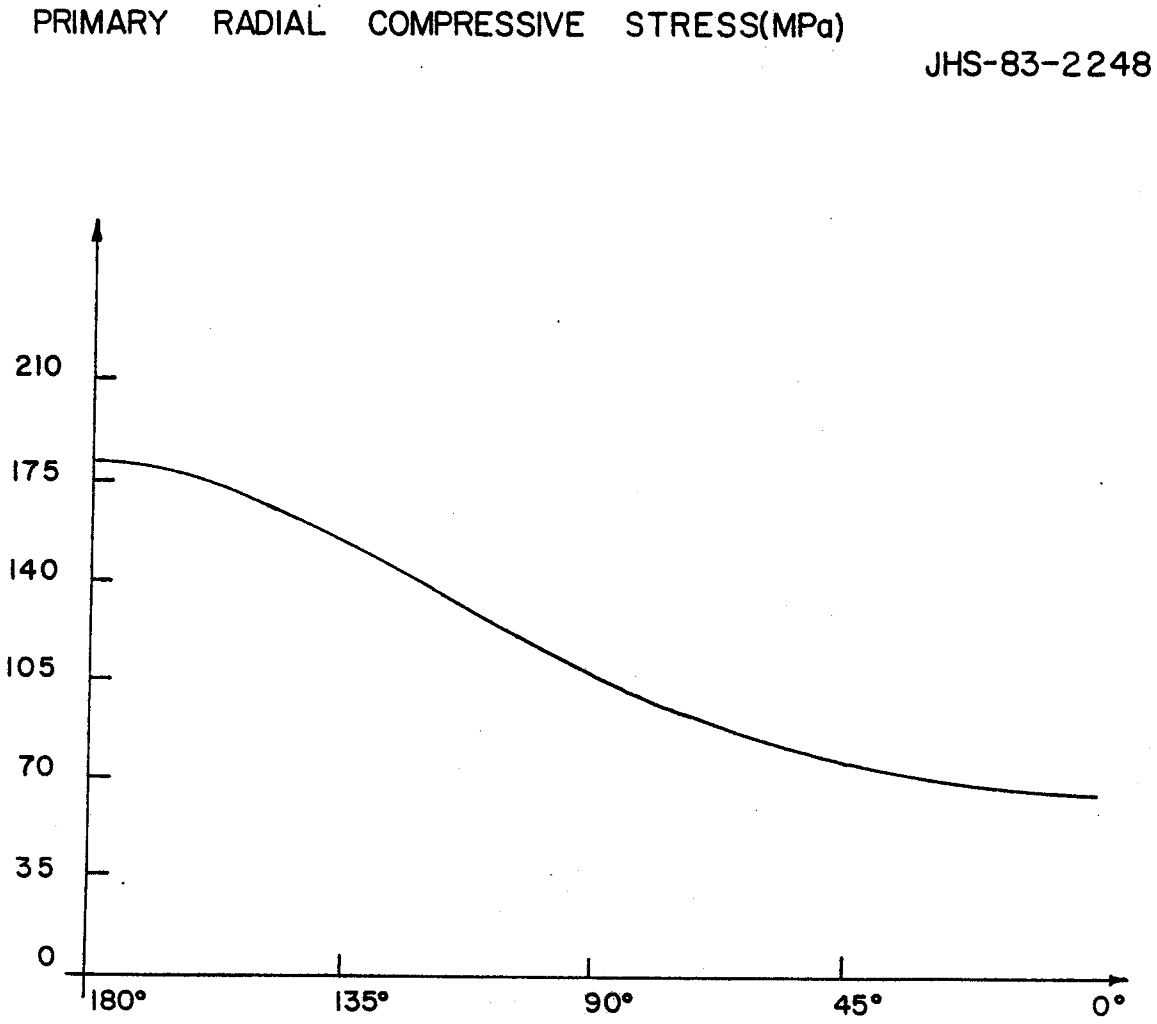

FIGURE 8.2.2.8

PRIMARY RADIAL COMPRESSIVE STRESS IN THE CONDUCTOR SHEATH OF THE TENTH LAYER VS. POLOIDAL ANGLE FROM THE TF MAGNET BORE, IF COIL IS SUPPORTED BY OUTER CASE AND UNBONDED.

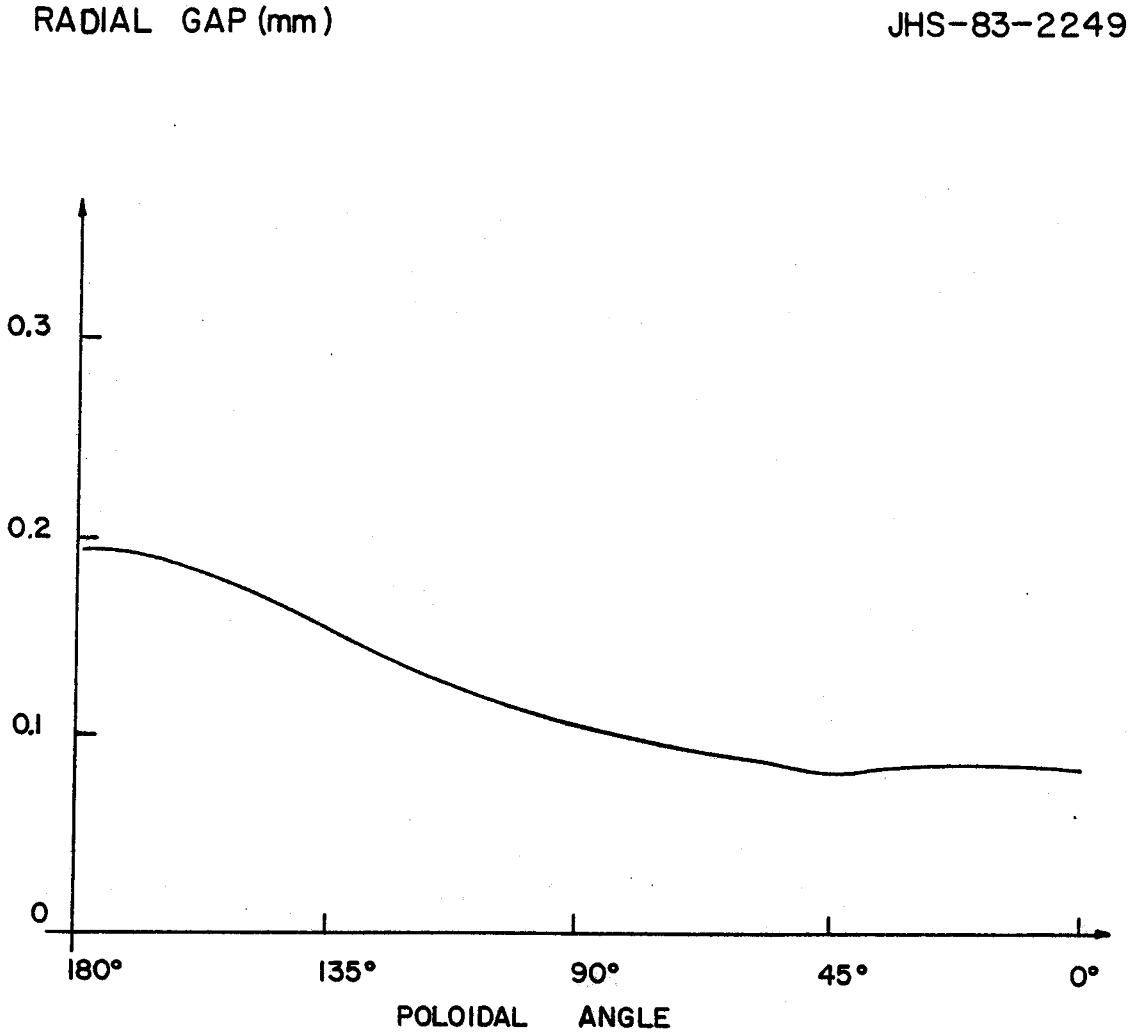

FIGURE 8.2.2.9

RADIAL GAP BETWEEN FIRST LAYER AND INNER BOBBIN VS. POLOIDAL ANGLE FROM TF MAGNET BORE, IF TF MAGNET SUPPORTED BY OUTER CASE AND UNBONDED.

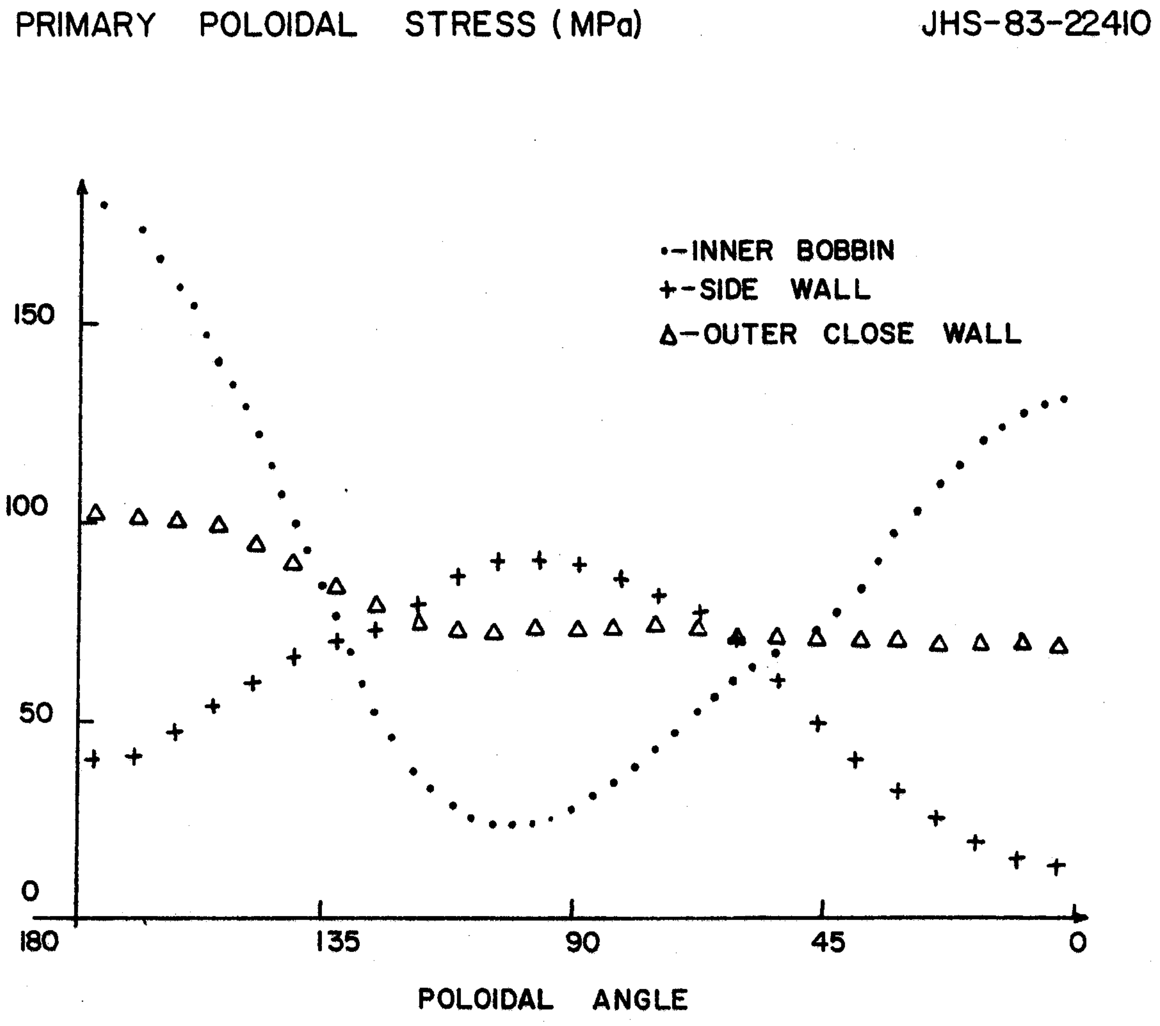

FIGURE 8.2.2.10

PRIMARY POLOIDAL TENSILE STRESS IN INNER, OUTER AND SIDE WALLS OF TF COIL CASE VS. POLOIDAL ANGLE, IF CONDUCTOR SUPPORTED BY OUTER WALL AND UNBONDED.

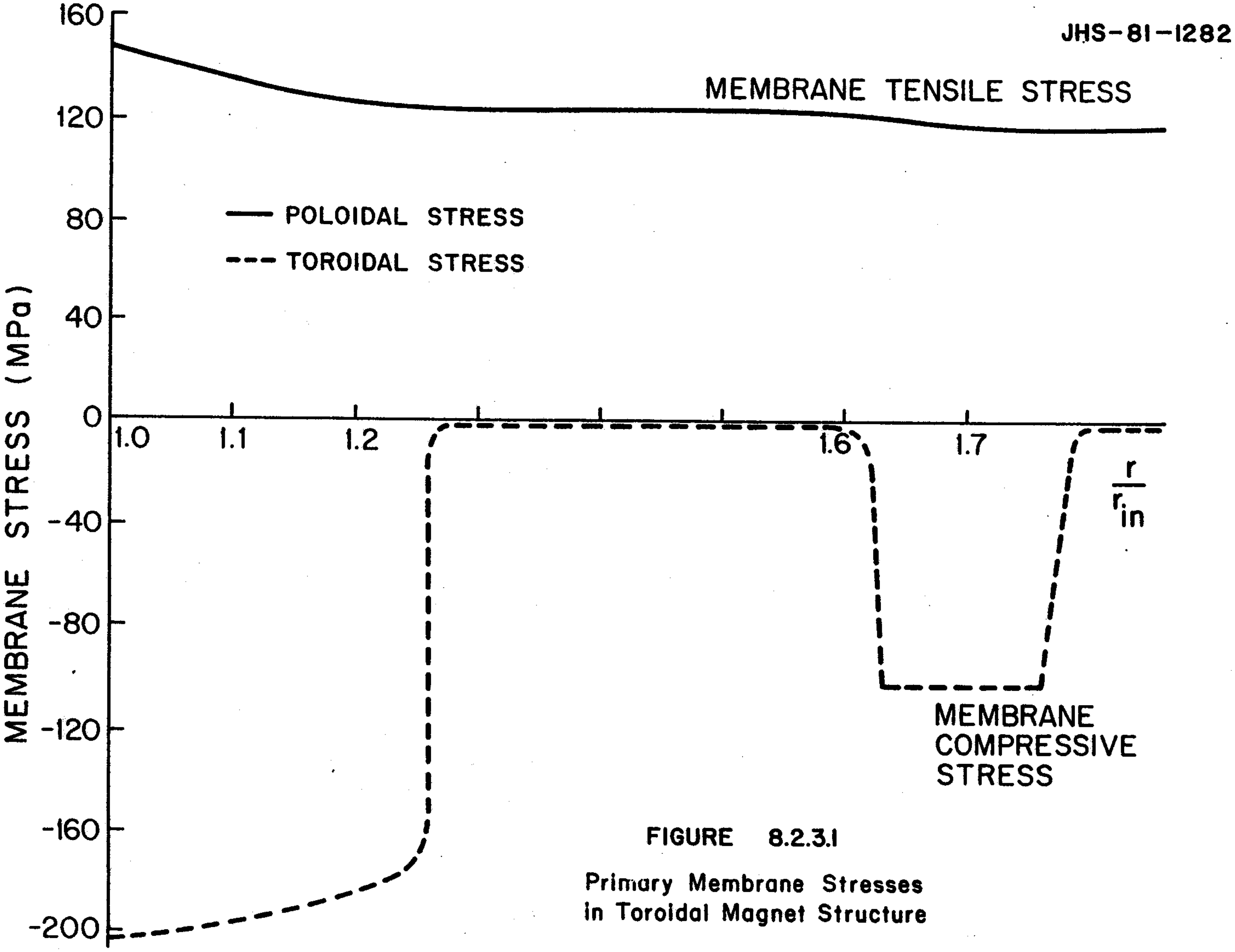

FIGURE 8.2.3.1

Primary Membrane Stresses
In Toroidal Magnet Structure

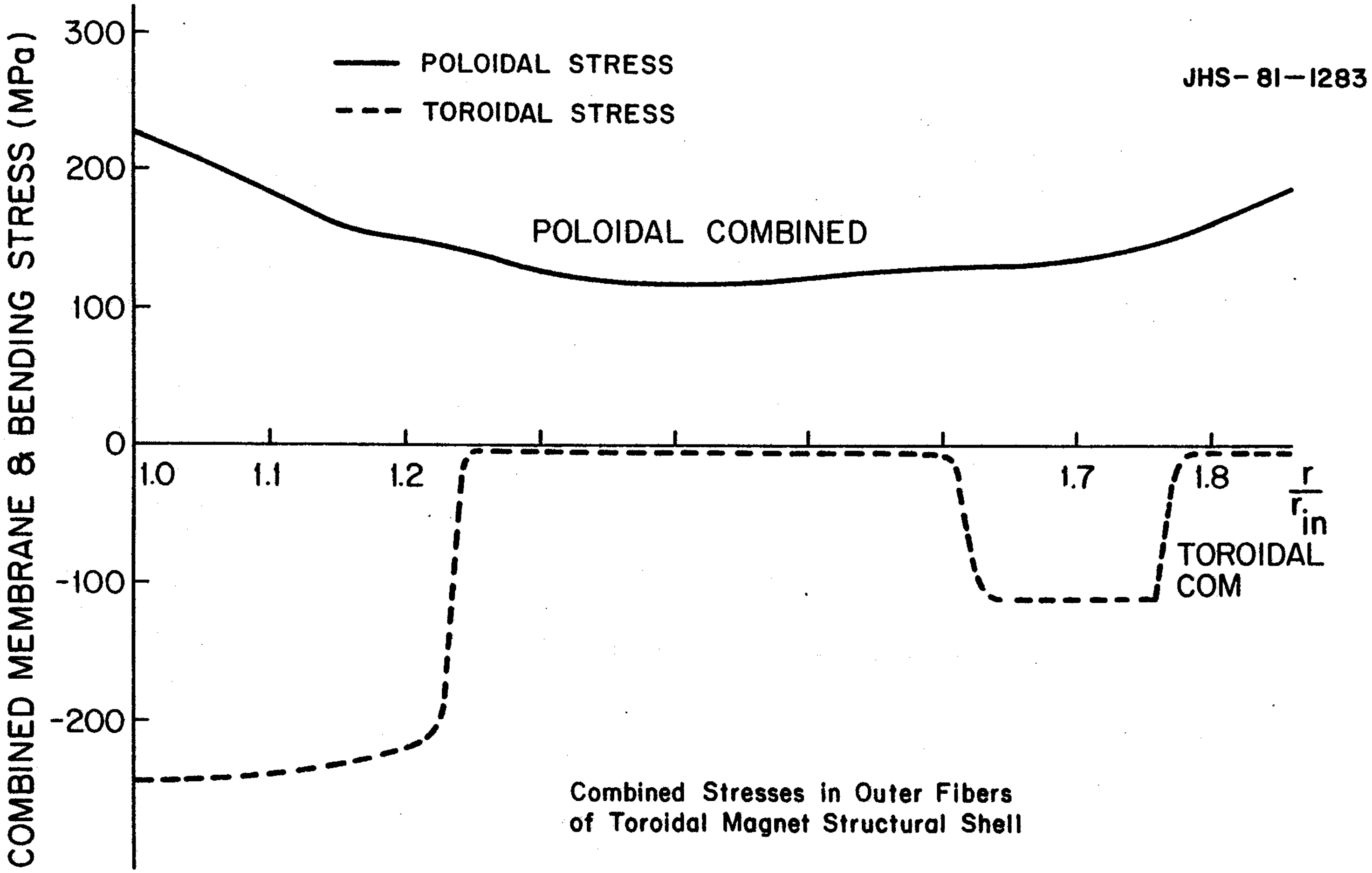

Combined Stresses in Outer Fibers
of Toroidal Magnet Structural Shell

FIGURE 8.2.3.2

JHS-82-1281

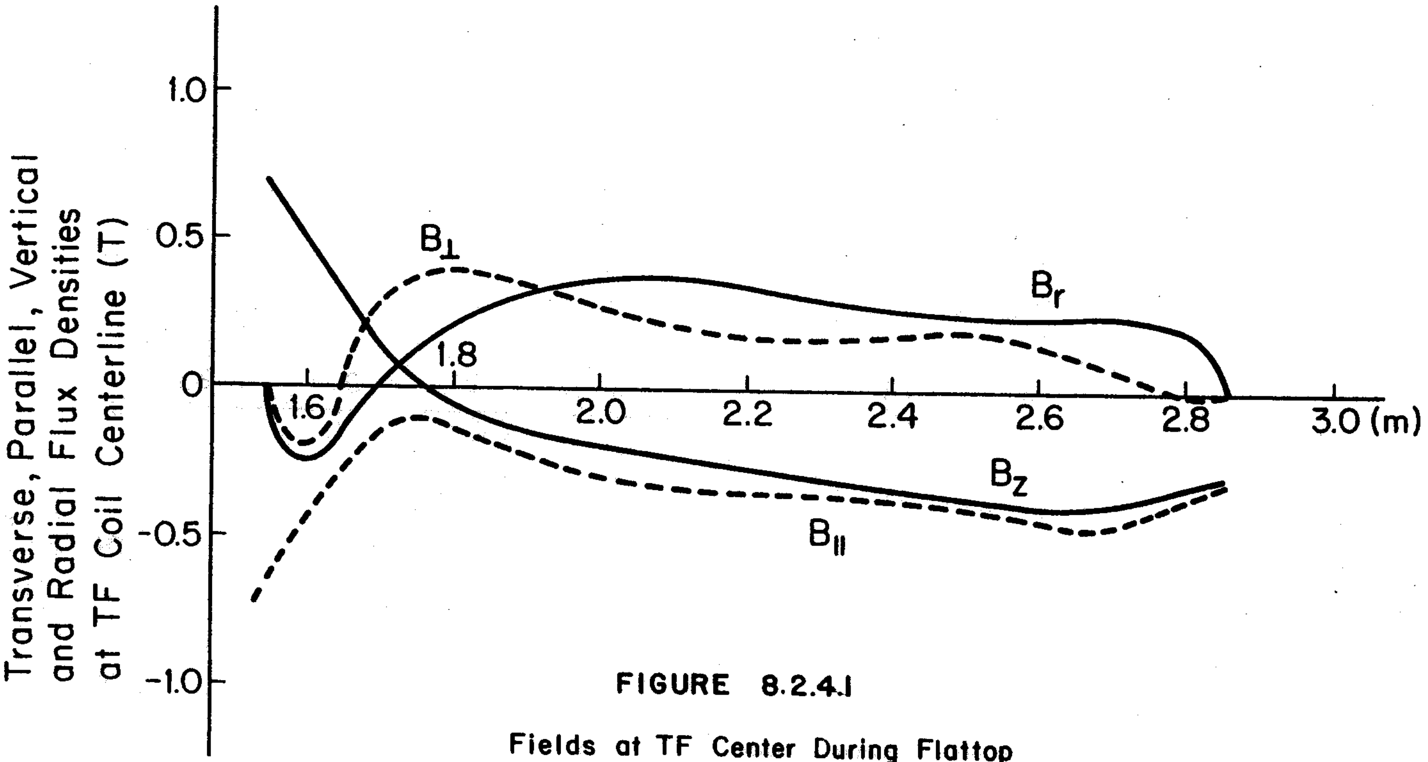

FIGURE 8.2.4.1

Fields at TF Center During Flattop for High Beta Discharge (Ip = 1.2MA)

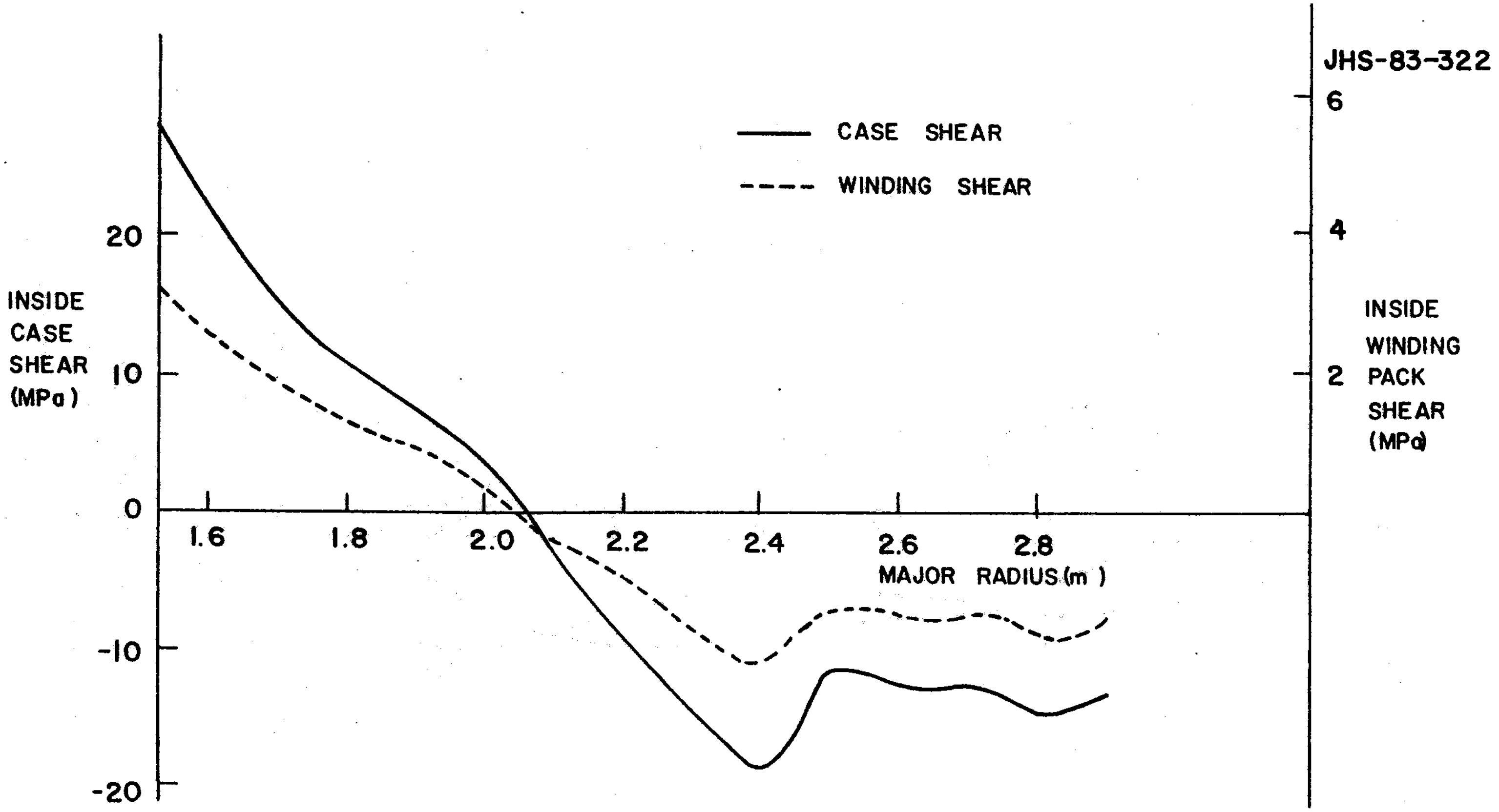

FIGURE 8.2.4.2

SHEAR STRESS VS. RADIUS DUE TO OUT-OF-PLANE LOADS ON TOROIDAL FIELD COILS.

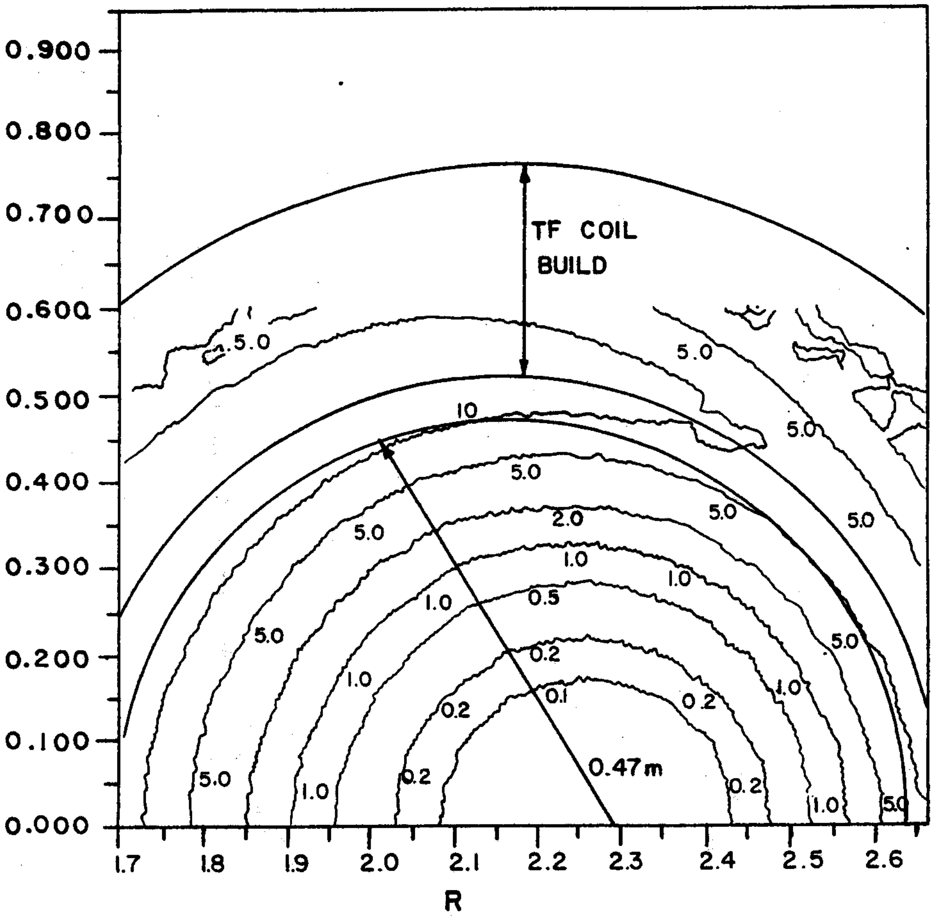

CONSTANT RIPPLE CONTOURS

FIGURE 8.5.1

CONSTANT TOROIDAL RIPPLE CONTOURS FOR THE 36 COIL CASE WITH NO NOTCH.

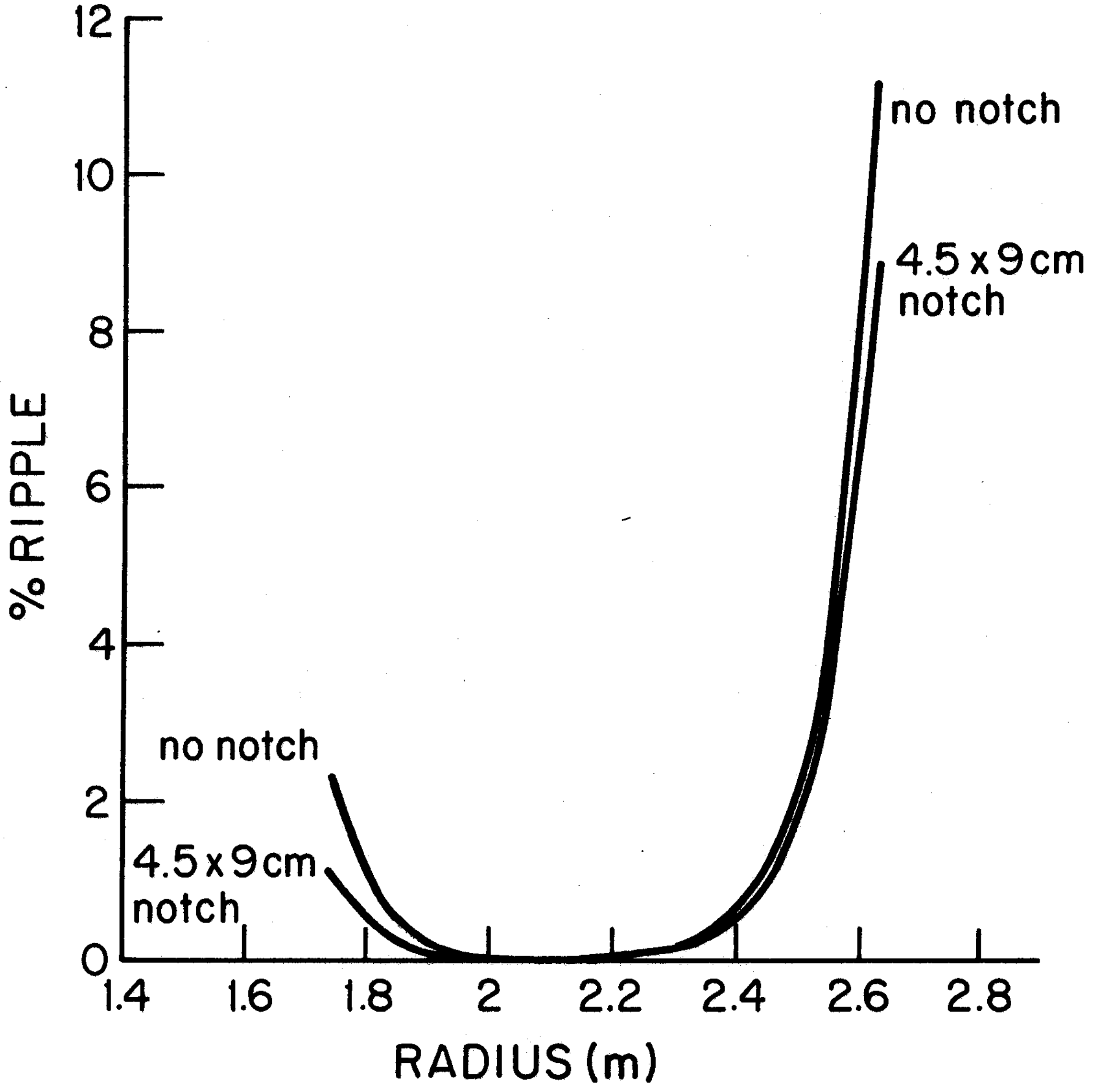

Figure 8.5.2
Comparison of Toroidal Ripple at Equator With and Without a Notch in the Toroidal Field Coil Winding Packs

9.0 The Poloidal Field Magnet System

The poloidal field magnet system is a conventional set of ohmic transformers and equilibrium field transformers. There is, of course, no fundamental distinction between these two sets of coils, except that the ohmic transformer power supplies are programmed independently from those of the equilibrium coil supplies, such that the ohmic system controls plasma current, while the equilibrium coils control position. These functions are independent but not orthogonal, since increases in the vertical equilibrium field also increase the plasma current. Shaping experiments being considered may use some of the coils normally used for control of plasma current to create elongated or triangular plasmas.

The poloidal field magnets could be either normal or superconducting without any substantial effect on the overall system cost, but superconducting magnets have been selected for the preconceptual machine because of their lower recirculating power and their greater relevance to tokamak programmatic requirements. Although, if all goes well, the ohmic transformer may no longer be required at the end of the HESTER experimental program, an ohmic transformer with a very large volt-second capability has been included. This allows a broad range of long pulse experiments, even in the absence of current drive, and including a class of experiments with partial current drive, reduced electric field and very long pulses. Perhaps most significantly, the ohmic volt-second swing of 35 V-s allows an ohmically driven pulse length at all temperatures, which is an order of magnitude higher than the classical magnetic diffusion time. For the first time, this will provide unambiguous differentiation between plasma behavior in the flux-conserving and magnetic steady-state regimes. Even if current drive should be wholly successful, the highest ion temperature and pressure experiments would use all available high voltage regulated supplies to drive the ICRF sources, so current drive would not be used in these important shorter pulse experiments.

9.1 The Equilibrium Field System

The equilibrium field coils have been designed on the basis of a low beta and high beta MHD equilibrium. The low beta equilibrium is for the maximum $n\tau$ discharge described in section 3. The high beta equilibrium is for the same plasma parameters, but with the toroidal beta increased to 1.5 %. This is actually somewhat higher than the highest beta expected in the high beta experiment described in section 4, but allows room for upgrade by sizing the EF system, the TF system intercoil structure and the refrigerator pulsed loss heat removal system for the more demanding requirements of a higher beta discharge. The positions and currents in the EF system coils are listed in Table 9.1-I. Several MHD equilibria have been obtained, but the equilibrium field system has only been sized on the basis of two discharges that appeared relatively attractive from the point of view of good plasma pressure with low total EF system ampere-turns and ampere-meters.

9.2 Ohmic Current Magnet System

Since the principal mission of the HESTER experiment is to provide a testbed for very long pulse discharges, the ohmic transformer is designed to provide a larger number of total volt-seconds. Although it is probably possible to design a lower hybrid steady-state drive with a relatively high degree of confidence, the large ohmic drive adds considerably more flexibility for high density discharges, current drive assisted discharges, and auxiliary power-limited discharges. The maximum number of volt-seconds for a double-swung ohmic heating transformer, 35 V-s , is considerably larger than that for other comparably sized tokamaks. The ohmic flux and voltage requirements of the plasma are summarized in Table 9.2-I. For an ohmic discharge with a predicted resistive voltage of 2 V , about 11.9 V-s are required from the ohmic heating transformer, after which a flattop discharge of 11.5 s is possible. For a high temperature discharge, for example a peak central electron temperature of 10 keV, the flattop discharge time could be extended to 120 s. For the slightly elongated, moderated beta discharges used for poloidal magnet sizing purposes, the inner elongating EF coil largely cancels the volt-second contribution of the outer, radial equilibrium EF coil, so that the contribution of the EF system to the overall flux requirement of the system is small.

The currents and positions of the ohmic heating coils are shown in Table 9.2-II. The ohmic heating system is divided into a central solenoid and an inner and outer coil pair in the same region as the inner and outer equilibrium field coils. The ohmic coils in the central solenoid are subdivided into 5 independent coils, because of the current limitations of the superconductor and the voltage limitations of unpotted, pool-boiling magnets. The current distribution in the three OH coil regions is selected to minimize field leakage into the plasma region.

9.3 Poloidal System Scenario

A scenario of coil and plasma parameters vs. time has been developed for the higher beta discharge described above. Ideally, the sizing of components should be based on all of the different types of planned experimental discharges, but no tokamak design to our knowledge has ever been able to either model all possibilities or absorb the results of such models at the conceptual design level. This capability is currently being built into the TOKSYC tokamak system analysis code [SC82]. It is felt that a discharge at the machine limits of beta and current will come close to defining the requirements of the poloidal field system. A scenario for a highly shaped, probably lower performance plasma should also be developed.

The plasma and poloidal system scenario has many purposes, being used for the selection of poloidal magnet power supplies, pulsed refrigeration losses, and electromagnetic force and stress analysis, as well as influencing the selection of auxiliary power levels. A possible set of voltages and currents for each coil in the poloidal field system is shown in Figure 9.3.1 for the EF system and Figure 9.3.2 for the OH system. This possible set fits the fixed ampere-turn and volt/turn requirements of the scenario. The selection of the operating current and the number of turns per coil is based primarily on the constraints that a maximum limit of 10 kA should be placed on the CDIF conductor, in order to be relatively close to cryostable operation at low fields, and that current be limited to 70 % of critical current at higher fields. At higher fields, the conductors are also constrained to 7,000 A, in order to assure cryostable operation, since the conductors operating in higher fields are the most likely to experience normal events. Since the CDIF conductor has not yet been tested for its behavior in a pulsed field environment, these criteria will probably have to be revised.

9.3.1 Force Scenario on the PF Magnets

The PF magnet currents in reference scenario above cause a time history of radial and vertical forces on each of PF coils. This time history is shown in Figures 9.3.1.1 and 9.3.1.2. As can be seen, the highest forces are usually, but not necessarily at the end of the discharge flattop. A common problem in magnet structural design for off-normal conditions is that forces can be in the reverse direction from those of their normal operating conditions, requiring in particular adequate structure against both radially inward and radially outward deflections. In a complex tokamak scenario, this phenomenon can be seen during a normal discharge, as occurs in coils 2, 4, 12 and 13. Similarly, vertical forces change direction in the course of a normal discharge for coils 1, 2, 3, 12 and

13. Axial forces on the ohmic heating central solenoid coils are only significant on the upper and lower outer modules. The radial forces on each of the 5 modules are nearly identical. Without doing a comprehensive fault analysis or a consideration of all possible types of plasma discharge, it is clear that all coils will require relatively stiff restraints against motion in all four case wall directions.

9.3.2 Poloidal Magnet Power Conditioning Equipment

Because of the absence of resistive power requirements in superconducting coils, the power conditioning equipment in use on Alcator C will be largely adequate for the poloidal magnet system of HESTER. The currents and voltages selected above would have to be changed somewhat in a final design for an optimum fit to the available power conditioning equipment at M.I.T., shown in Figure 9.3.2.1 in the configuration in use on Alcator C. The rectifiers in this set of equipment can be upgraded to steady-state operation by increasing the water flow to the thyristor collector heat sinks. Rectifier-transformers can be operated at short pulse currents up to pulse lengths of about twenty seconds, as shown in Figure 9.3.2.2. If HESTER achieves full power operation for longer pulse lengths, new transformers would be purchased.

The Alcator C rectifier set is adequate for the needs of the above scenario, if the OH system is discharged passively into switched resistors. If active control is required during the first half of the OH cycle, two new modules must be added to the eight already available.

Acknowledgments

L. Bromberg found MHD equilibria. R.J. Thome suggested current distributions for the ohmic heating system.

Reference

[SC82] Joel H. Schultz, "TOKSYC 82: A Tokamak System Design Code", M.I.T. Plasma Fusion Center Report PFC/82-27, Nov. 1982

Table 9.1-1

CURRENTS AND POSITIONS OF EF COILS

R_{ef1}	major radius of the first EF coil	2.915 m
Z_{ef1}	height of the first EF coil	715.0 mm
I_{ef11}	total number of ampere-turns in the first EF coil on discharge 1	-354.7 kA-T
I_{ef12}	total number of ampere-turns in the first EF coil on discharge 2	-413.7 kA-T
R_{ef2}	major radius of the second EF coil	1.495 m
Z_{ef2}	height of the second EF coil	700.0 mm
I_{ef21}	total number of ampere-turns in the first EF coil on discharge 1,	630.0 kA-T
I_{ef22}	total number of ampere-turns in the second EF coil on discharge 2,	731.0 kA-T
R_{o1}	plasma major radius for discharge 1	2.033 m
R_{o2}	plasma major radius for discharge 2	2.082 m
I_{p1}	plasma current for discharge 1	817.0 kA
I_{p2}	plasma current for discharge 2	1.190 MA
ϕ_{11}	flux linkage between EF1 and the first plasma	-1.023 V-s
ϕ_{12}	flux linkage between EF1 and the second plasma	-1.257 V-s
ϕ_{ef21}	flux linkage between the second EF coil and the first plasma discharge	1.208 V-s
ϕ_{ef22}	flux linkage between the second EF coil and the second plasma discharge	1.388 V-s
ϕ_{ef}	EF system contribution to the plasma inductive volt-seconds for an ohmic discharge	368.3 mV-s
ϕ_{efbeta}	EF system contribution to the plasma inductive volt-seconds for a high beta discharge	262.2 mV-s
NI_{mef}	number of ampere-meters in the EF system	28.89 MA-m
NI_{ef}	total number of ampere-turns in the EF system	2.289 MA-T

Table 9.2-I

OHMIC FLUX AND VOLTAGE REQUIREMENTS

R_o	plasma major radius	2.091 m
a_{minor}	plasma minor radius	312.3 mm
V_r	flattop resistive voltage	1.835 V
ψ_p	plasma inductive volt-second requirements	8.474 V-s
t_{flat}	flattop time	8.500 s
V_i	loop voltage required for initiation	105.1 V
Φ_{rsu}	resistive volt-seconds during start-up	3.390 V-s
Φ_{rflat}	resistive volt-seconds during flattop	15.60 V-s
Φ_r	total resistive volt-second requirement of the plasma	18.99 V-s
Φ_{tsu}	total volt-second requirement of ohmic start-up	11.86 V-s
Φ_{total}	total volt-second requirement of the plasma	27.46 V-s

Table 9.2-II

CURRENTS AND POSITIONS OF THE OH COILS

i	OH coil number	1
R_{1oh}	inner major radius	955 mm
R_{2oh}	outer major radius	1.240 m
Z_{1oh}	lower height	595.0 mm
Z_{2oh}	upper height	991.6 mm
I_{oh}	ampere-turns in the i-th OH coil	1.47 MA-T
i	OH coil number	2
R_{1oh}	inner major radius	955 mm
R_{2oh}	outer major radius	1.240 m
Z_{1oh}	lower height	198.3 mm
Z_{2oh}	upper height	595.0 mm
I_{oh}	ampere-turns in the i-th OH coil	1.47 MA-T
i	OH coil number	3
R_{1oh}	inner major radius	955 mm
R_{2oh}	outer major radius	1.240 m
Z_{1oh}	lower height	-198.3 mm
Z_{2oh}	upper height	198.3 mm
I_{oh}	ampere-turns in the i-th OH coil	1.47 MA-T
i	OH coil number	4
R_{1oh}	inner major radius	955 mm
R_{2oh}	outer major radius	1.240 m
Z_{1oh}	lower height	-595.0 mm
Z_{2oh}	upper height	-198.3 mm
I_{oh}	ampere-turns in the i-th OH coil	1.47 MA-T
i	OH coil number	5
R_{1oh}	inner major radius	955 mm
R_{2oh}	outer major radius	1.240 m
Z_{1oh}	lower height	-991.6 mm
Z_{2oh}	upper height	-595.0 mm
I_{oh}	ampere-turns in the i-th OH coil	1.47 MA-T
λ_{joh}	overall current-density in the i-th OH coil	13 MA/m^2

Table 9.2.II

CURRENTS AND POSITIONS OF THE OH COILS - CONTINUED

i	OH coil number	6
R_{1oh}	inner major radius	1.527 m
R_{2oh}	outer major radius	1.738 m
Z_{1oh}	lower height	839.2 mm
Z_{2oh}	upper height	1.051 m
I_{oh}	ampere-turns in the i-th OH coil	1.341 MA-T
i	OH coil number	7
R_{1oh}	inner major radius	1.527 m
R_{2oh}	outer major radius	1.738 m
Z_{1oh}	lower height	-1.051 m
Z_{2oh}	upper height	-839.2 mm
I_{oh}	ampere-turns in the i-th OH coil	1.341 MA-T
i	OH coil number	8
R_{1oh}	inner major radius	2.852 m
R_{2oh}	outer major radius	2.979 m
Z_{1oh}	lower height	773.8 mm
Z_{2oh}	upper height	900.5 mm
I_{oh}	ampere-turns in the i-th OH coil	482.1 kA-T
i	OH coil number	9
R_{1oh}	inner major radius	2.852 m
R_{2oh}	outer major radius	2.979 m
Z_{1oh}	lower height	-900.5 mm
Z_{2oh}	upper height	-773.8 mm
I_{oh}	ampere-turns in the i-th OH coil	482.1 kA-T
$NI_{ohtotal}$	number of ampere-turns in the OH system	7.364 MA-T
$NI_{mohtotal}$	number of ampere-meters in the OH system	46.27 MA-m

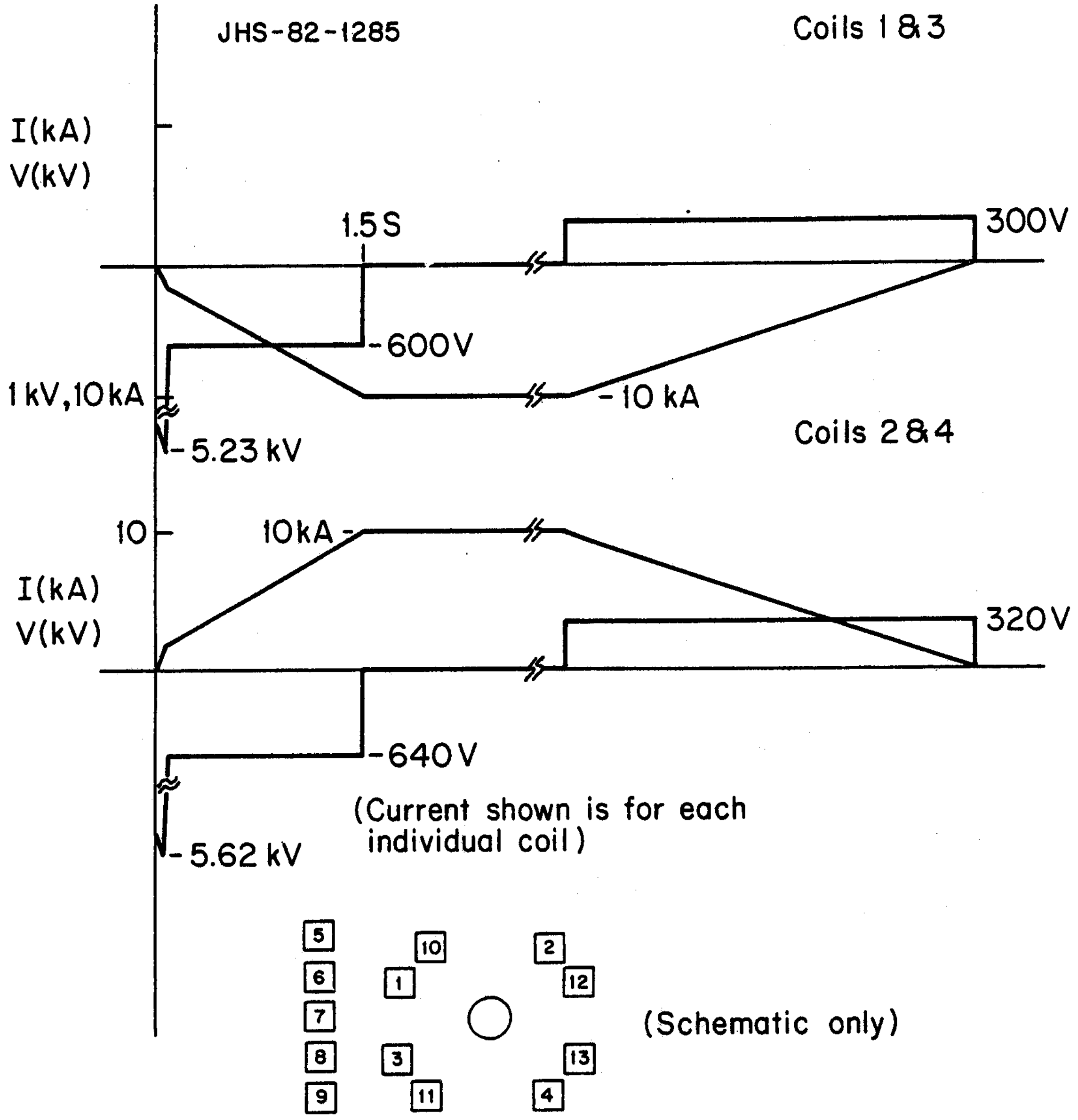

EF Coil and Supply Requirements

FIGURE 9.3.1

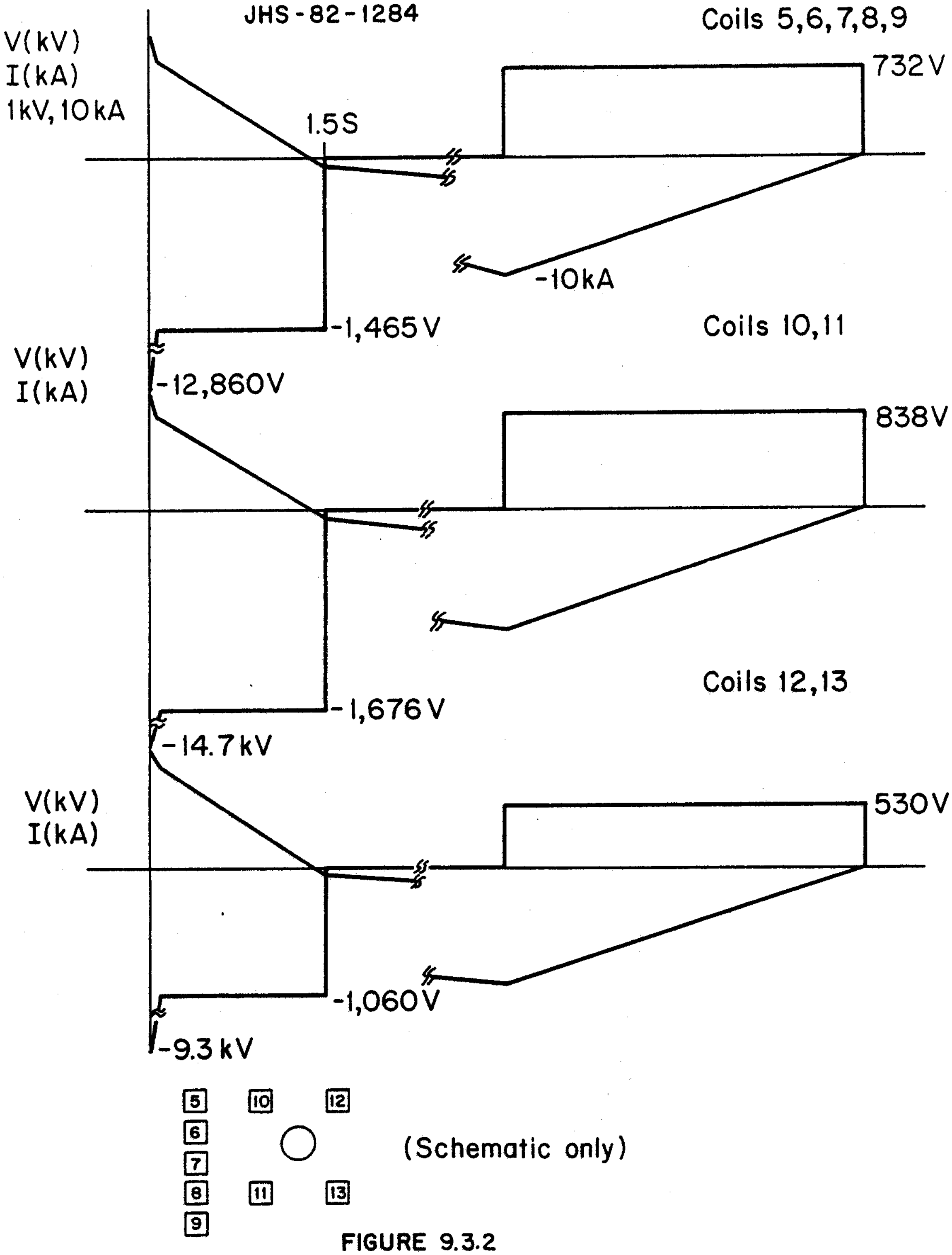

FIGURE 9.3.2
OH Coil and Power Supply Requirements

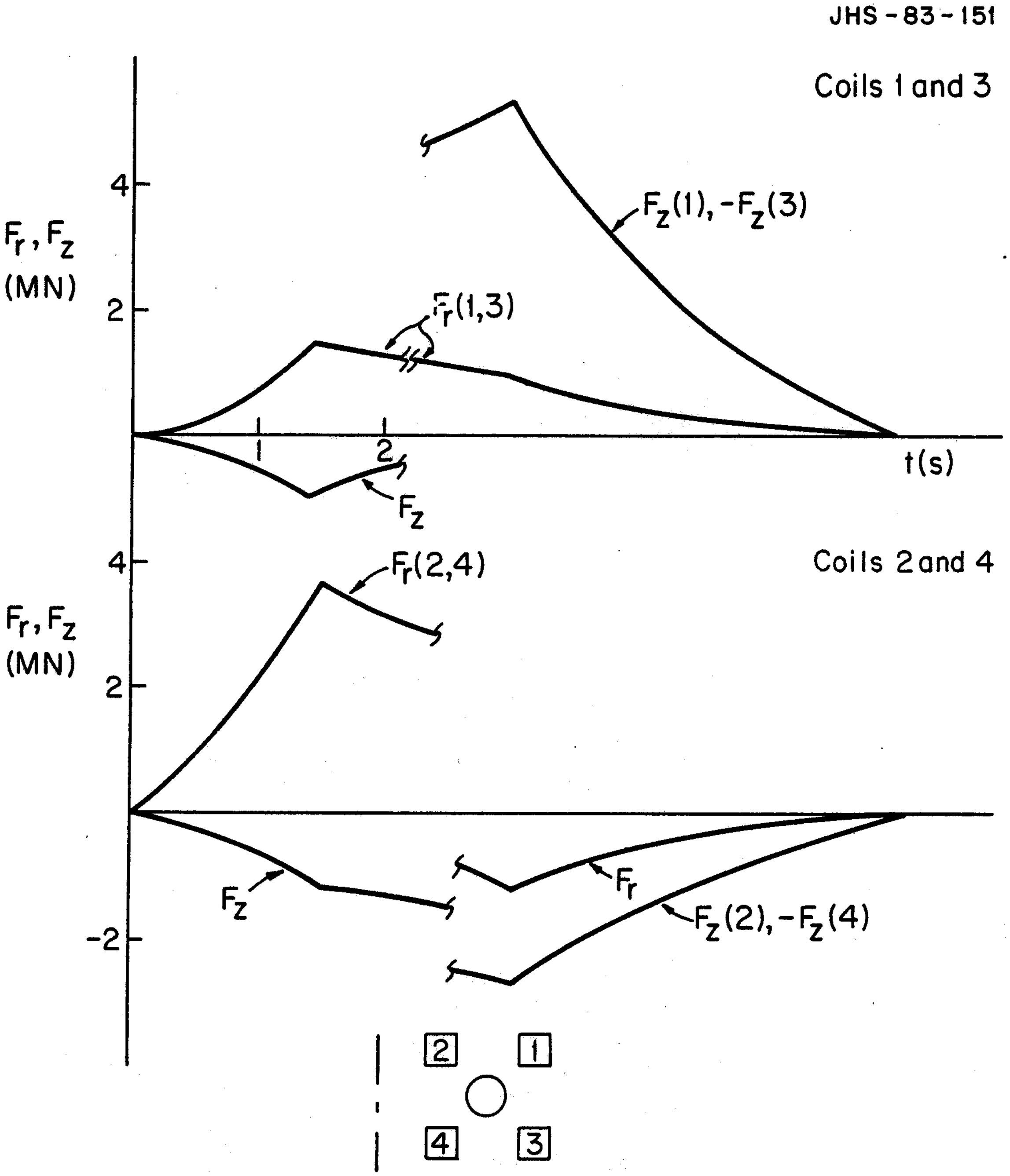

Figure 9.3.1.1
Radial and Vertical Forces on EF Coils for Reference Scenario

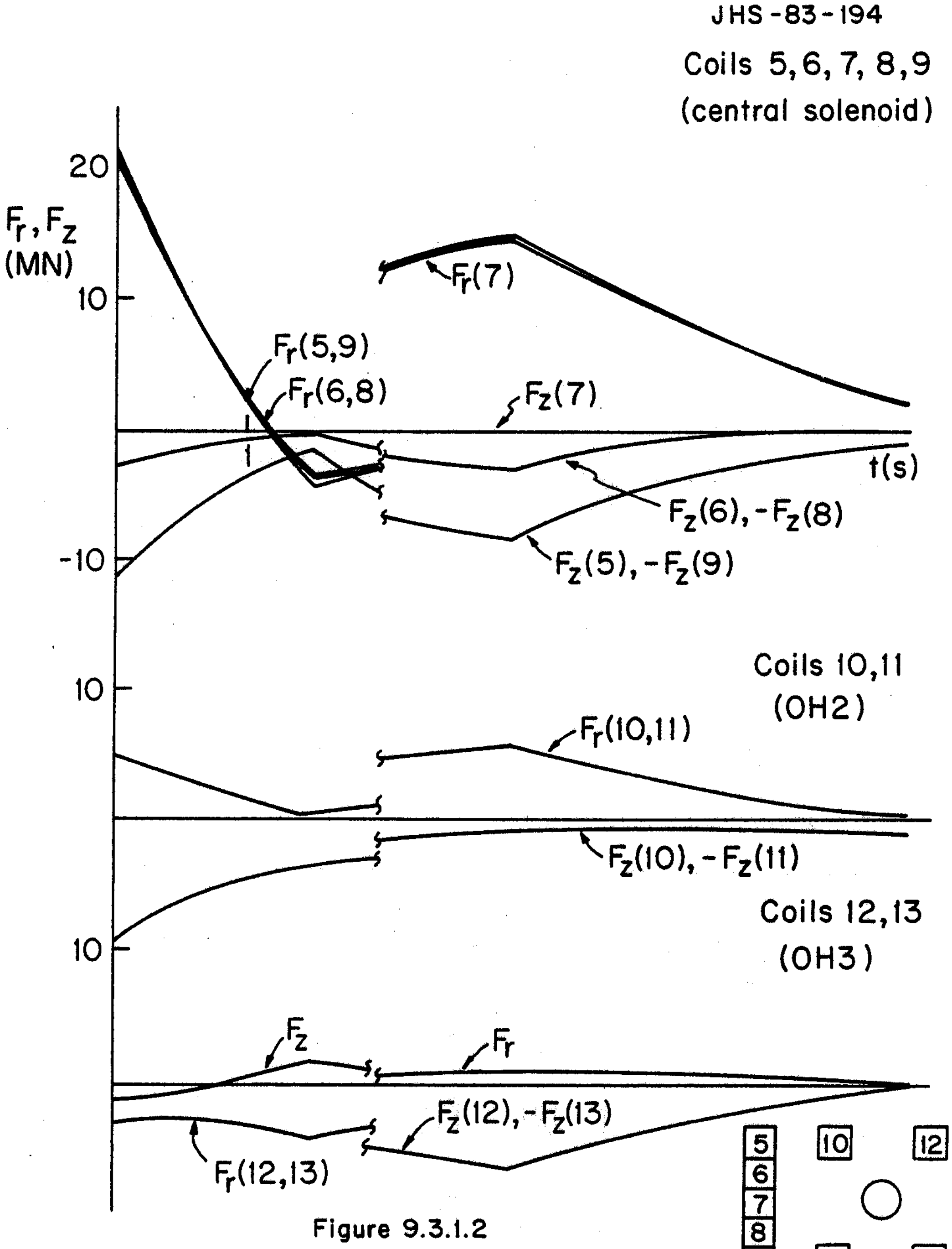

Figure 9.3.1.2
Radial and Vertical Forces
Ohmic Heating Coils

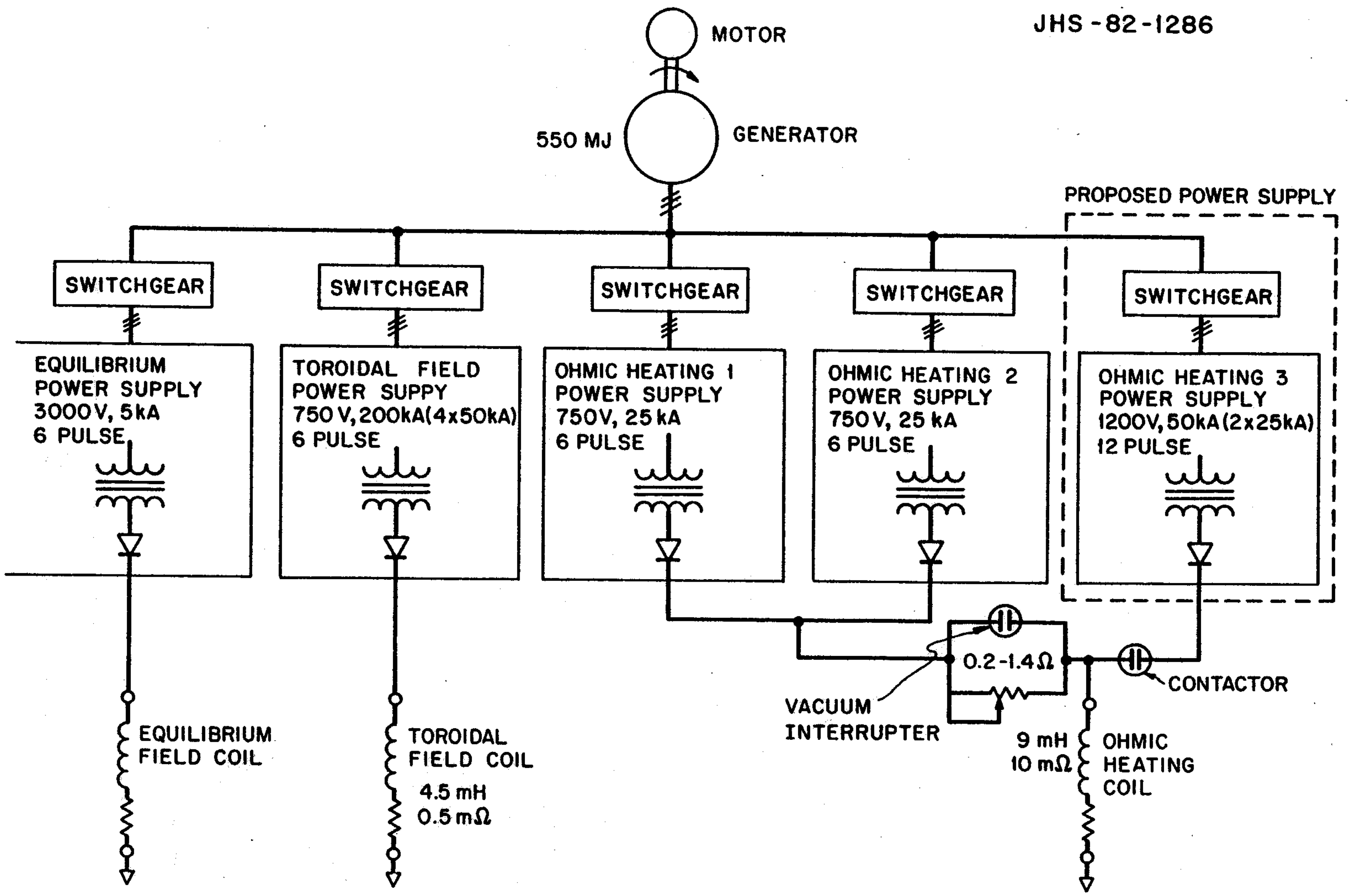

FIGURE 9.3.2.1
Existing Power Conversion Equipment at M.I.T.
Plasma Fusion Center for Alcator C

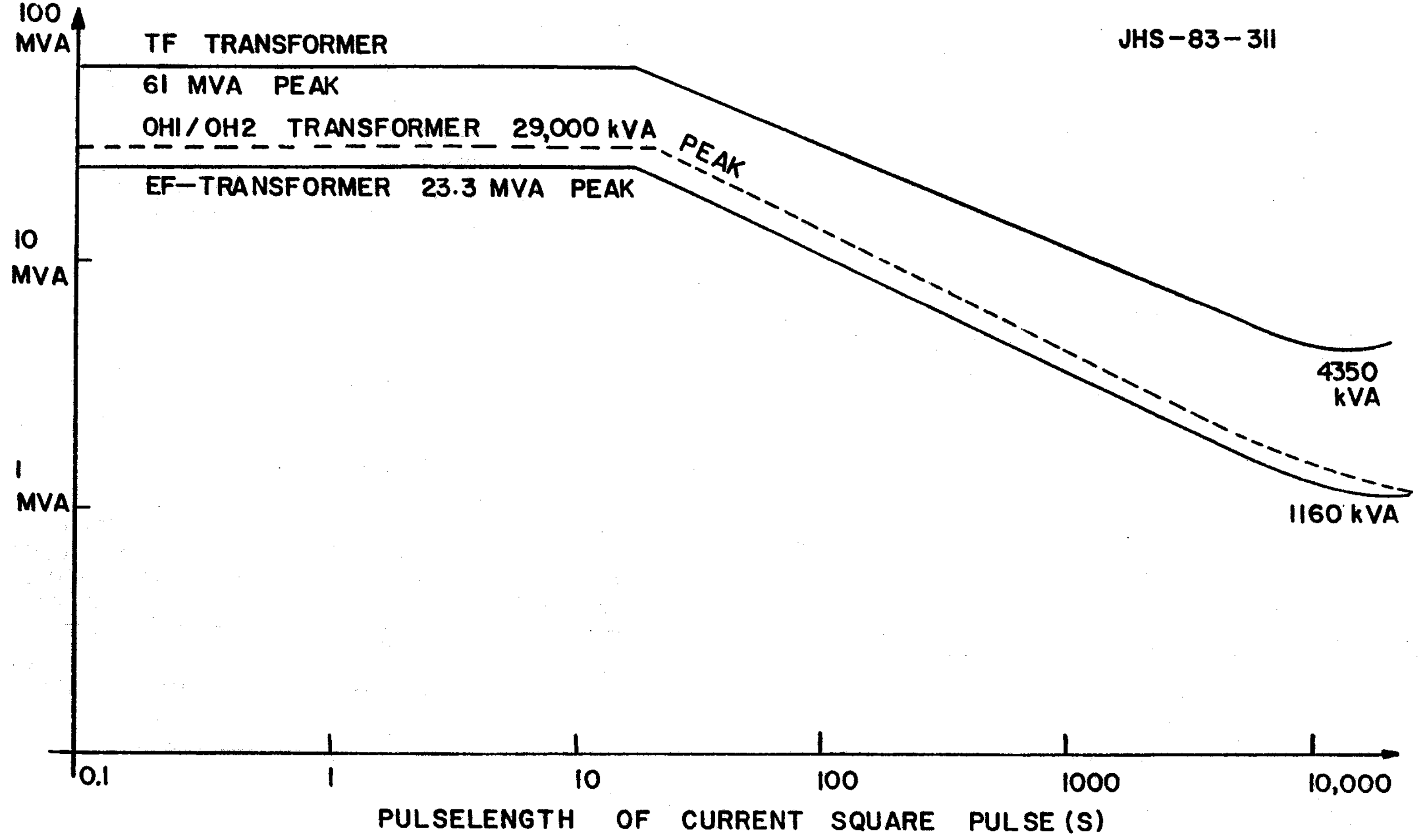

FIGURE 9.3.2.2

DERATING OF ALCATOR C RECTIFIER/ TRANSFORMER

10.0 RF Heating Electrical Equipment

The radio frequency (RF) electrical equipment in HESTER is a straightforward simple extension of the RF equipment already in use on Alcator C. In particular, the lower hybrid heating and current drive and ion cyclotron resonance heating equipment use the same frequencies as the Alcator C experiments. A limitation in utilizing the Alcator C equipment fully is the decrease in the peak available magnet flux density from 14 T to 7 T. This limits the ICRH experiment to second harmonic proton heating. The Alcator C ICRH experiment also plans to heat protons at the second ion cyclotron harmonic frequency, but the magnet engineering safety factor for the Alcator C experiment is much greater. Within accessibility limits, discussed in chapter 5, the efficiency of lower hybrid current drive is primarily a function of parallel phase velocity which can be better controlled at a high frequency, allowing sixteen parallel waveguides within the available horizontal port space of 24 cm. It remains to be determined whether the field limitations of HESTER will lead to suboptimal current drive efficiency, as discussed in chapter 6.

10.1 The Lower Hybrid (C-Band) Microwave Delivery System

The C-Band delivery system consists of high voltage transformers and rectifiers, series regulators, klystrons, circulators, microwave waveguide plumbing including power splitters and instrumentation, and internal, reduced width waveguides.

High voltage regulated power supplies in Alcator C are shared with the ICRF power delivery system described below. An option being considered for HESTER is the addition of unregulated power supplies for the ICRF transmitters, in order to permit simultaneous operation of lower hybrid and ICRF equipment at low cost. The regulators are supplied with rectified power from 4 rectifier-transformer tanks with 2 series rectifiers in each tank. Each tank is capable of providing the regulators with 58 kV and 16 A. Only 11.5 kA is provided to the regulators in actual operation because of current limitations in the C-band klystrons. The oil tanks are uncooled and would have to be derated by a factor of 2 for a 10 s pulse and by a much larger factor for cw operation. The addition of external cooling circuits for long-pulse operation in HESTER would be much less expensive than complete replacement of the rectifier-transformer sets, but tests are required to determine whether pulsed ratings can be duplicated in longer pulse operation. Under normal operating conditions, the voltage passed by the regulator is down to 46 kV, so that the plate power delivered to a klystron is 46 kV x 11.5

A = 529 kW. Since the gain of the klystrons is 45.7 db, the power requirement of the input ports is negligible. In a full power lower hybrid experiment on Alcator C, 16 klystrons will be driven, providing 4 MW of RF power and requiring 8.46 MW of regulated power and 10.7 MW of unregulated dc power.

10.2 Existing C-Band Equipment

The Alcator C microwave system can deliver 2.6 MW to the edge of the plasma. The basic RF drivers are 16 4.6 GHz klystrons, each capable of 260 kW of RF output. These klystrons are capable of delivering 260 kW cw, so no derating of the tubes is planned for the long pulse current drive experiments. The cost of 17 klystrons for the project was $1.13 M. The microwave delivery equipment includes regulated power supplies, circulators, waveguides and microwave electronics. Each klystron is followed by a filter and a circulator. The insertion losses of the filter and the circulator are 0.1 db apiece, reducing the power delivered to the waveguides to 158 kW per klystron, or 2.6 MW for the system.

10.3 New C-Band Equipment

The HESTER experiments require twice the power of the Alcator C system in order to test a broad range of current drive and auxiliary regimes. If waveguides and windows have to be derated by a factor of two or four because of the long pulse requirements, the cost in additional windows, power splitters and directional couplers will cancel the cost savings of using existing tubes and of using a window/launcher array concept which is already developed. The Alcator C and Alcator A delivery systems have achieved significantly greater power densities than the microwave delivery systems of other tokamaks. The Alcator A waveguides achieved 8 kW/cm^2 with the windows close to the plasma and the ECRF layer pressurized and 4 kW/cm^2 with the windows far from the plasma and the ECRF in vacuum. Alcator C has duplicated the power densities of Alcator A with the windows close to the plasma. FT has claimed power launching densities of 6 kW/cm^2 at 2.45 GHz through windows and waveguides also believed to be at cryogenic temperatures during a discharge [AL82]. Most tokamak experiments experience conditioning-like breakdown at power launching densities on the order of 1 kW/cm^2. In a noncryogenic environment, 2.5 kW/cm^2 has been reported on JFT-2. Since multipactor breakdown occurs at higher power densities for higher frequencies and is also suppressed by low secondary electron emission, such as is characteristic of metals at cryogenic temperatures, the reason for the superior performance of the Alcator C windows and waveguides is not entirely understood. According to Schuss [SC82], a half wavelength ceramic window, identical topologically to the Alcator C window, was tested with the Alcator A supply at 2.45 GHz, to a power launching density of 8 kW/cm^2 with 10-20 ms pulses at room temperature. The load side of the window was vacuum, while the source side was dry, unpressurized nitrogen. Windows have achieved 8 kW/cm^2 into vacuum. It is possible to test the limits of wave launching through warm windows into the Alcator C plasma, although this has not yet been done. The design of HESTER includes cooling passages that allow the circulation of liquid nitrogen as a last resort insurance that adequate wave launching density can be obtained. Another option being considered in order to reduce the cost of launcher arrays is to increase the width of the individual waveguides. This permits more efficient waveguide launching with fewer waveguides overall, although lower waveguide losses may be more than balanced by a loss in control of the launched wave spectrum. In particular, the broader waveguide limits the maximum parallel index of refraction, which is probably not too harmful for current drive, but probably limiting the range of heating experiments for which penetration can be achieved.

HESTER has adequate port space to perform combined ICRF and LH experiments, designing even to the relatively pessimistic assumption that only 2.5 kW/cm^2 can be achieved. Unfortunately, a hardware cost analysis shows that at this launching density, the RF system cost is dominated by the cost of launching grills, windows, power dividers and associated instrumentation. A compromise design goal of 4 kW/cm^2 is selected, requiring proof of principle experiments. Tests into plasma with room temperature waveguides and window have, however, not been done, so that present results are encouraging but not definitive as to whether HESTER can achieve high launching densities for long pulses at noncryogenic temperatures and possibly somewhat reduced frequency. Since breakdown limits for long pulses are frequently associated with breakdown between the waveguide and windows, the windows could be placed outside the ports and perhaps before the power splitters in order to limit the power density through the windows and improve the accessibility of cooling. This places the ECRF layer in vacuum. Although this has been an area of concern that led to the selection of pressurized ECRF layers in Alcator C and PLT, a review of the generally ambiguous operating history of tokamaks [SC80] revealed no evidence that electron cyclotron resonance enhanced breakdown has occurred in tokamaks at power densities lower than 4 kW/cm^2.

The assumed achievable power density through the HESTER waveguides gives an overall system requirement for 480 individual waveguides, arranged in groups of 16 waveguides in a horizontal grill in a vertical stack of 5 grills. One port would then be capable of launching 1 MW into the plasma. Since the Alcator C scaling employed in Chapter 5 suggests a requirement for a launched power of 6.0 MW , 6 will be devoted to lower hybrid wave launching.

If the same system efficiencies are achieved as for the Alcator C system, then the klystron tubes will have to deliver 13.4 MW and 23 MW will be required from either the utility line or the on-site alternator. There is a possibility of obtaining more efficient klystrons in order to reduce the power requirements and the cost of high voltage regulated power. The klystrons being used by M.I.T. in the Alcator C experiment have a plate efficiency of only 45 %. Klystrons in a lower frequency range than those used in Alcator C have been developed with higher efficiencies.

Another possibility is that of using developmental tubes, as was done for the neutral beam sources of all of the major neutral beam injection experiments, the RCA 301A switch/regulator tubes for the TFTR neutral beam power supplies and the Varian 200 kW gyrotrons for EBT-I and ISX-B. At Stanford, a 500 kW cw tube was developed for PEP at 353 MHz with an overall efficiency of 70 % [KO77]. A new generation of 500 MHz klystrons was developed by Valvo, Hamburg for the PETRA Storage Rings at DESY [MU81]. The klystrons for the A storage ring were 540 kW cw tubes, operating at 60 % efficiency. If klystrons were replaced by smaller but more efficient crossed-field amplifiers, as proposed by Schultz [SC79] and adopted by the STARFIRE design [BA80], less RF power conditioning equipment would be required. As an example of the system benefits that might accrue from a tube development program, in 1964 Skowron and Brown demonstrated a crossed-field amplifier which developed 400 kW cw at a frequency of 3 GHz, a gain of 9 db and an overall efficiency of 72 % [SK64]. The electronic efficiency of the tube, exclusive of power dissipated at the cathode, in the straps, and in circuit losses, was at least 80 %. At the time that DOE's super power tube development program was canceled, the same design team at Raytheon was proposing to build a 1 MW, S-band tube with an overall efficiency of 85 %. Since the dimensions of a tube are essentially fixed by the frequency, both power and efficiency tend to go up together, since vane dissipation is usually the power limiting factor for cw operation. Benchmark performance of the above historical prototype tubes indicates the probable success of a tube development program which would almost pay for itself through the reduced cost of regulated power supplies in HESTER , and could greatly enhance the performance of any lower hybrid current drive upgrades in TFTR, JET and JT-60. However, any development program would have to be compatible with the construction and experimental schedule of HESTER .

10.4 Lower Hybrid Launching Array

The lower hybrid launching array concept is shown in Figure 10.1, with the number of waveguides consistent with the larger port size of the competing 24 coil option for HESTER. The internal and external dimensions of each individual waveguide are identical with those of the Alcator C grills. Each waveguide is a seamless, 304 stainless steel case, internally coated with silver to prevent excessive RF losses in the relatively long waveguide run within the port flange. Each row of waveguides is cooled and partially supported by top and bottom steel plates, which are themselves supported from the horizontal port flange and in-port mounting brackets. The BeO windows are placed 10 cm back from the plasma to avoid any significant particle deposition, but are inside the ECRF layer. Each window is 1.6 cm thick, corresponding to half a wavelength in beryllia. The waveguides fan back radially, so that there is adequate space between waveguides to bolt the adapter flange to the row support flange between each individual waveguide, preventing possible arcing between flanges. Each row is positioned with the aid of an array flange, radially inside the row flanges, which permits a row of waveguides to be removed individually. Outside the port area, standard adapters are connected to the adapter flange and the waveguides broaden to standard C-band waveguide.

References

[AL82] F. Alladio et al, "Lower hybrid heating experiments in FT tokamak," 9th International Conference on Plasma Physics and Controlled Nuclear Fusion Research, IAEA-CN-41/I-4, Baltimore, MD, Sept 1982

[BA80] C.C. Baker et al, "STARFIRE - A Commercial Tokamak Fusion Power Plant Study," Argonne National Laboratory Report ANL/FPP-80-1, 1980

[KO77] G.T. Konrad, "Performance of a high efficiency high power klystron," SLAC-PUB 1896, March 1977

[MU81] H. Musfeld, H. Kumpfer, and W. Schmidt, " A new generation of cw-klystrons for accelerator and storage ring application, practical experience and aspects for future developments," IEEE Trans Nuc Sci, Vol. NS-28, No. 3, June 1981

[SK64] J.F. Skowron, W.C. Brown and G.H. MacMaster, "The Super Power CW Amplitron," Microwave Journal, Oct. 1964

[SC80] J.H. Schultz, "Towards a strategy of reliable fusion first wall design," M.I.T. Plasma Fusion Center Report PFC/RR-81-19, May, 1981

[SC82] J.J. Schuss, private communication

[SC79] S.Y. Yuen, J.H. Schultz et al, "Design features of tokamak power reactors with RF-driven steady state current," M.I.T. Plasma Fusion Center Report RR-79-22, Nov 1979

10.4 Engineering Aspects of the ICRF Heating Experiment

The outstanding feature of the ICRF heating experiment is that most of the equipment necessary for 10 MW of ICRF injection at the proton second harmonic frequency is already on-site at M.I.T. and will be largely wasted without the HESTER experiment to utilize it. This equipment was obtained as surplus, four years ago, from the United States Air Force, when the radar transmitter system deployed in Shemya, Alaska was dismantled. The useful parts of the system were acquired by the Department of Energy and then assigned to M.I.T. for use in ICRF heating on Alcator C. The first ICRF heating experiment using this equipment is scheduled for early in 1983. Transferred items included amplifier chains, coaxial transmission lines and miscellaneous RF and electrical components. Selected RF components from other USAF radar stations were also added at a later date to the Alcator C system. The power supplies, configured for high-power, short-pulse operations were unsuitable for experimental purposes and were replaced by new high voltage regulated supplies, used on both the ICRF and lower hybrid heating experiments on Alcator C. As explained below, these regulated supplies will provide half of the required power for HESTER . A full line of RF diagnostics and control instrumentation were also purchased for the Alcator C experiment, which can also be utilized on HESTER .

The VHF transmitters at M.I.T. employ RCA 6952 tetrodes, which can be run for 10 s with a plate dissipation of 500 kW and an expected overall efficiency of 60 %, giving an available RF output power of 750 kW/tube. Air Force test logs indicated that thirteen of these tubes are in perfect condition and can be run to full power. Twelve cabinets are available, each with output resonators that permit operation at 200 MHz. Only the two tubes to be used in the Alcator C heating experiments currently have driver amplifiers attached. The other 10 would require new drivers, such as one provided by EIMAC which would cost $5 per tube, along with another $5 per cabinet for cabinet modification and mounting.

The Y676A high voltage regulator tubes used for both the lower hybrid and ICRF heating experiments on Alcator C can pass 100 A at 25 kV steady-state, according to the manufacturer's curves. Therefore, 8-10 MW of regulated dc power is available for a long pulse experiment. If all 9 MW of RF power is transmitted to the plasma, four new regulated power supplies would have to be purchased. However, the purchase of new supplies could conceivably be postponed until initial success is achieved, heating at 4 MW.

Acknowledgments

Evaluation of the capabilities of RF equipment at the M.I.T. Plasma Fusion Center was done by D. Griffin. The lower hybrid wave launching array concept was developed by J.J. Schuss and N. Diatchenko.

Component/ Subsystem	No. of Units	Power Handling (100 ms)	Power Handling (10s)	Power Handling (CW)
Rectifier/ Transformer	4 tanks 8 rectifiers	58 kV × 64 A = 3712 kW, max 58 kV × 48 A, nom = 2,784 kW, nom × 4 = 11.1 MW	58 kV × 32 A = 1.856 MW/tank × 4 = 7.42 MW/syst	0
Y676A Regulator (High V)	16	46 kV × 11.5 A = 529 kW/tube × 16 = 8.46 MW	P_d = 100 kW I = 100 kW 112 kV = 8.33 P = 383 kW × 16 = 6.1 MW	P_d = 100 kW I = 8.33 A
Y676A Regulator (Med V)	- -	22 kV × 33 A = 726 kW × 12 = 8.7 MW	P_d = 100 kW I = 100 kW/5 kV = 20 A P = 22 kV × 20 A = 440 kW × 16 = 7.04 MW	P_d = 100 kW I = 20 A P_σ = 440 kW/tube × 16 = 7.0 MW
RCA 6950 triodes	12	1.0 MW, rf × 4 = 4.0 MW	750 kW, rf × 4 = 3.0 MWW	300 kW, rf × 4 = 1.2 MW
klystrons	16 1 spare	250 kW × 16 = 4 MW	250 kW	250 kW
circulators	16	244 kW × 16 = 3.9 MW		
filters	16	238 kW × 16 = 3.8 MW		
External waveguides	64	209 kW/wg × 16 = 3.34 MW		
Internal waveguides	64	47 kW/wg 3.0 MW/64 wg	700 kW/wg	700 kW/wg
vhf coax	200 ft 9"			
vhf antennas	1			
measurement & control				
vhf, 2041 tetrodes	3	82 kW	82 kW	82 kW

Input Requirements	Efficiency (%)	Original Cost (K$)	Replacement Cost (K$)
		$ 1,245 K (3 rect. × FMR, modulators) $ 185 K/tank + $ 230 K/modulator	$ 278 K/tank
58 kV × 11.5 A = 667 kW/tube × 16 = 10.7 MW	79.3	$ 180 K/1 + $ 50 K, rehab /4 modulators	$ 86 K/modulator
27 kV × 33 = = 891 kW/tube × 16 - 14.3 MW	81.5		
3 × 22 kV × 33 A + 1 × 22 kV × 33 A/driver = 2.18 MW/tetrode (1.25 MW @ 750 kW) 600 kW/driver	60	0	$ 200 K/tube (RCA estimate, includes driver)
46 kV × 12 A = 552 kW × 16 = 8.83 MW		$ 66 K/1 $ 1.13 M/17	$ 100 K/klystron
250 kW × 16 = 4 MW	97.5%	$ 5 K/circulator $ 80 K/16	$ 7.5 K/circulator
244 kW/filter × 16 = 3.9 MW	97.5%		
238 kW/wg × 16 = 3.8 MW	90%	$ 12.5 K/wg	$ 12.5 K/wg
52 kW/wg × 64 = 3.34 MW	90%		
	.05 db/200 ft		
		$ 20 K	$ 80 K 70 cm id × 17 cm × 4 cm
		$ 5 K/wg	$ 7 K/waveguide
15 kV × 10 A = 149 kW/tube	55%	- -	$ 10 K/tube

ASSUMED POWER FLOW/RF EXPERIMENTS

JHS-83-391

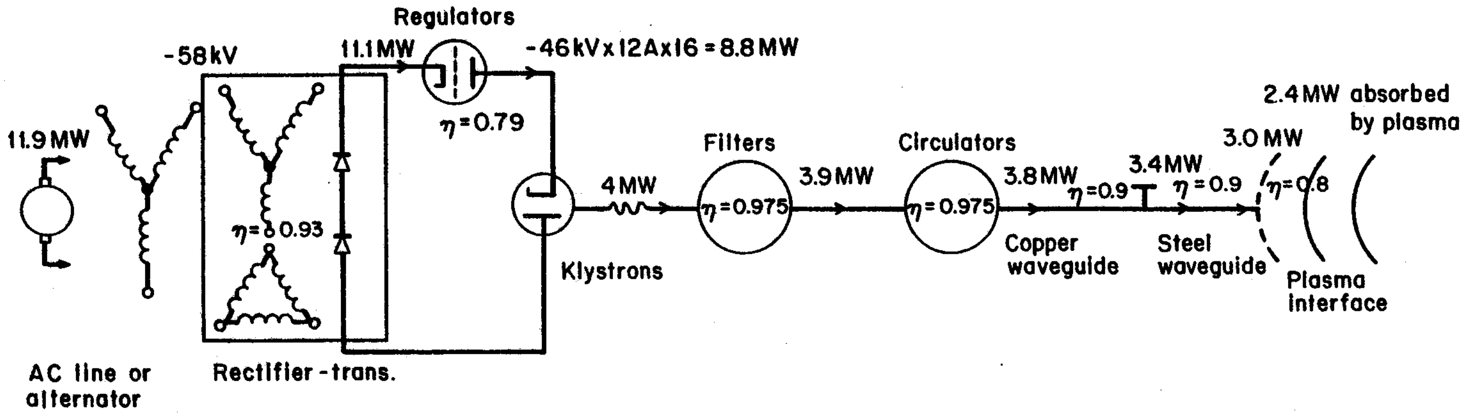

16 KLYSTRON EXPERIMENT

FIGURE 10.1

ASSUMED POWER FLOW/RF EXPERIMENTS

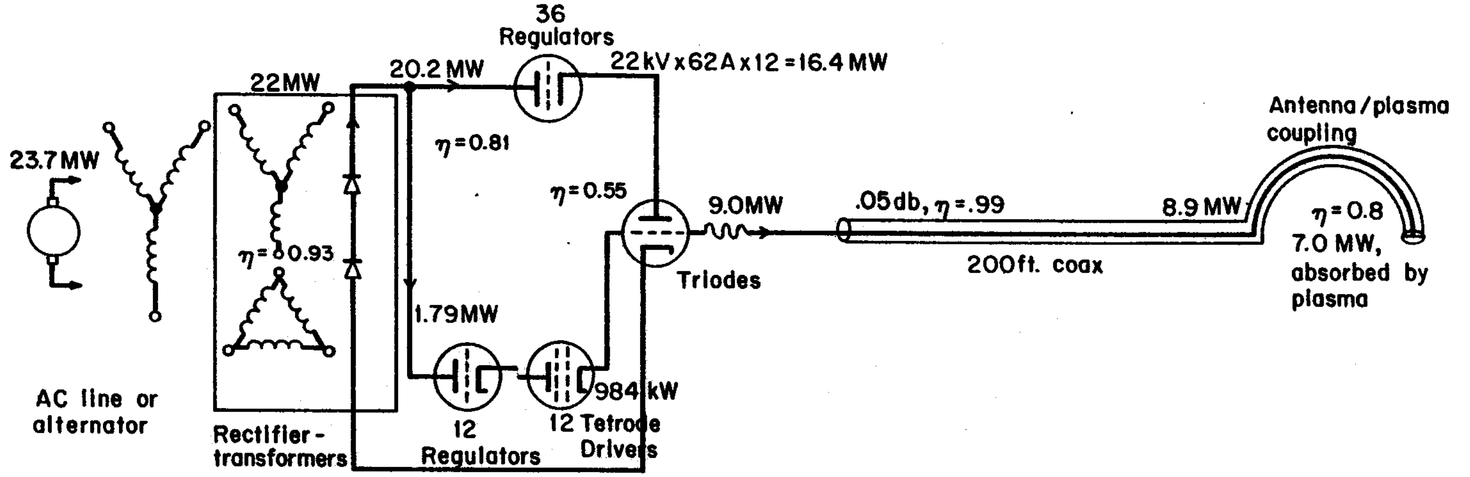

12 TRIODE EXPERIMENT

FIGURE 10.2

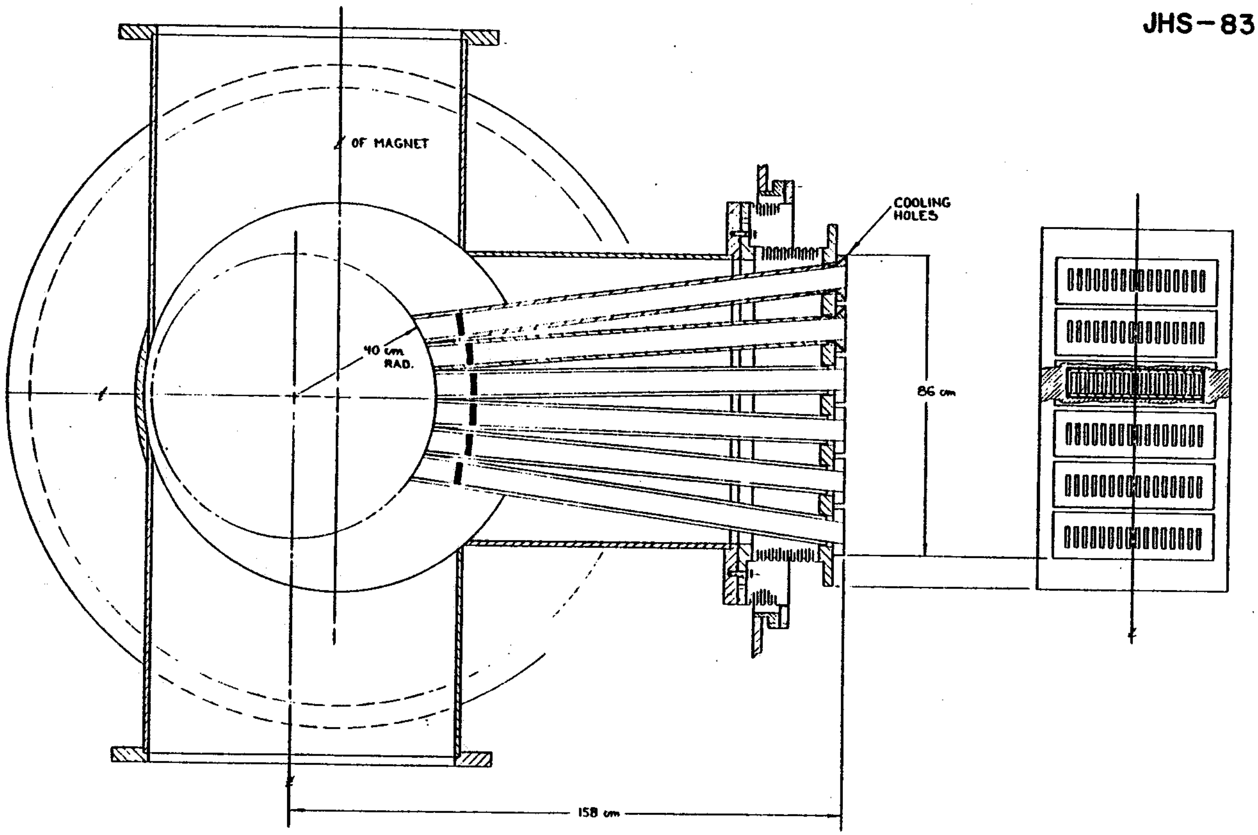

FIGURE 10.3

LOWER HYBRID WAVEGUIDE GRILL SYSTEM.

11.0 Cryogenic Refrigeration System

The cryogenic refrigeration system provides cooling for all of the magnets in the system. This system provides the combination of pulsed and steady-state operation required by a typical four day series of single shift experiments. The specific refrigeration system design is based on the assumption that M.I.T. will acquire the use of the refrigeration system from the cancelled MHD Component and Device Integration Facility (CDIF). This system has a large storage capacity, which will be used to multiply its instantaneous refrigeration capability.

11.1 Cryogenic Refrigeration Requirements

The cryogenic refrigeration system operates both the pool-boiling PF magnets and the internally cabled TF magnets by boiling-off helium in an atmospheric pressure, 4.2 K pool. The loss mechanisms causing helium boil-off include pulsed magnetic field losses due to start-up, shut-down and plasma disruptions, thermal radiation, conduction through cold mass supports and joint losses. The liquefaction requirements are determined by the lead losses in the TF and PF system. Table 11.1.1 lists the individual refrigeration requirements of the system. The basis for these loss estimates is described in chapters 8 and 9.

The entropy generation of the system, and thus the helium and electrical power requirements, are totally dominated by helium flow through the leads. If no measures were taken to reduce this requirement, the 340 l/hr required for the leads would require the same refrigeration capacity from a CTI-2800 helium refrigerator as 1.04 kW of pool-boiling refrigeration at 4.2 K, or twice the size of all other loads. Because the lead losses dominate, the option of discharging the TF coil through only two leads is selected, which also eliminates out-of-plane loads on the coils. If the number of discharge leads were increased to 4, the overall lead helium requirement would be increased by 20 %, while the discharge voltage would be decreased by 1.4.

A promising approach is to develop a disconnectable cryogenic lead, such as those constructed for the Los Alamos METS program [LI75], or to reduce the helium level in a specially designed lead. Both of these concepts could be used in parallel to provide a reliable method for reducing lead losses during idle periods, such as evenings and weekends.

After the current leads, the largest source of entropy generation is the pulsed magnetic field loss in the poloidal field magnets. This is not surprising, since the poloidal field system is wound with the CDIF superconductor, a fairly large monolith. The already fabricated CDIF superconductor was selected because it is the only conductor that provides a basis for conservative mechanical and electrical design within budgetary constraints. Since the poloidal field system of HESTER is a good test bed for intermediate size pulsed magnets, a possible improvement in this source of refrigeration loss would be to replace magnets using CDIF conductor with more advanced superconducting coils as part of United States and/or Japanese technology development programs.

11.1 Resources at M.I.T.

The M.I.T. Plasma Fusion Center and National Magnet Laboratory already have certain cryogenic refrigeration and distribution facilities, that could be utilized in support of the HESTER experiment. In particular, the Fusion Center has requested a CTI-2800 refrigerator from the canceled MHD Component Development and Integration Facility (CDIF), The CDIF refrigeration equipment on-site also includes a 4,000 liter liquid helium dewar, a 30,000 gallon warm gas storage tank and an 11,000 gallon liquid nitrogen dewar. Another CTI-2800 at the M.I.T. Low Temperature Laboratory, is being used for the EPRI 5 MVA superconducting generator program, whose cancellation is a possibility, and whose planned life would end before that of HESTER.

11.2 Refrigerator Design Concept

The refrigeration system design attempts to utilize the inherent downtime of typical experimental tokamak operation (single shift operation and no runs on weekends), along with the assumed availability of all of the CDIF equipment, in order to achieve significant cost savings. The design described below permits 600 W of cryogenic losses during each of four daily 8 hour experiments, with 80 discharges a day. It does not require the purchase of an additional CTI-2800, but instead allows the 200 W refrigerator to provide 600 W of refrigeration by purchasing an additional heat exchanger and cold turboexpander that permit stored helium to be utilized effectively. An additional benefit of the expander is that subcooling of the magnet baths can also be provided. The subcooling option then becomes a lower duty cycle capability of the base machine and does not require additional funding for an upgrade. An important caveat is that the refrigerator design has assumed that it will be possible to thermally disconnect power leads during the 136 hours a week that the machine is not in operation.

The refrigerator block diagram is shown in Figure 11.1.1. The basic CTI-2800 refrigerator with an additional compressor is run continuously as a liquefier, with a capability of generating 15,000 liters of helium per week or of filling the available 8,000 liters of helium storage capacity in 3 $\frac{1}{2}$ days. During operation of the tokamak, the helium level of the storage dewar is drawn down. If no additional refrigeration were available, it would be necessary to only operate the tokamak every second day. In order to avoid such a severe inconvenience, a simple second refrigerator is constructed of a room temperature, 20 atmosphere screw compressor (60 g/s , 1 atmospheres inlet or 30 g/s, $\frac{1}{2}$ atmosphere inlet), available from Mycom or Sullair, a 600 W heat exchanger such as those built by Meyer Tool for the Fermi National Accelerator Laboratory, and a cold expansion engine, available from Koch. A second 4,000 l storage dewar is added to the 4,000 l already available from the CDIF program. A small third compressor is also added to the two which are standard with a CTI-2800, increasing the liquefaction capacity by 50 % to 3 g/s. The total cost of the additional capacity is somewhat more than half the cost of a new CTI-2800 system. Additional costs to the cryogenic system would include cryogenic valves and transfer lines, instrumentation, warm piping, liquid nitrogen piping.

With the additional capacity available from the 600 W heat exchanger, only 32 % of the helium flow to the tokamak has to be made up from stored liquid helium. The 2800 supplies 3 g/s to the liquefier, which in turn supplies 14 g/s to the tokamak. Thus in an 8 hour run, the storage dewar is drawn down by 2,640 liters. Over a 24 hour period, the storage dewar has been drawn down by 1,200 liters and 6,240 liters immediately after the fourth consecutive days of runs with no down time. This level is then replenished in 69 hours over the weekend.

Acknowledgments

The selection and costing of components for the refrigeration system was made by Paul Brindza.

References

[LI75] J.D.G. Lindsay and D.J. Blevins, "10 kA low resistance superconducting switch," Proc 6th Symp Eng Prob Fus Research, San Diego, CA, Nov 1975

Table 11.1.1

Cryogenic Loss Inventory

Pulsed Losses	Loss/Cycle (kJ)	Average Load (W)
PF Losses	235	392
TF Losses	5.4	9.0
Disruption Pulsed Losses		
PF Loss/Disruption	450	–
TF Loss/Disruption	206	–
Lead losses, PF	47 (l)	280(l/hr)
Lead losses, TF	10	62 (l/hr)
Joint losses, TF	49	150
Joint losses, PF	2.3	3.8
Cold mass support	9	15
Radiation	70	117

Steady-state load, no pulse (without lead disconnect)	282 W, refrigeration	342 l/hr, liquefaction
Average loading, pulsed operation	687 W,refrigeration	342 l/hr, liquefaction
Maximum inventory loss/pulse	1,027 kJ (500 l, boil-off)	86 kJ, lead loss 57.6 l, helium to leads

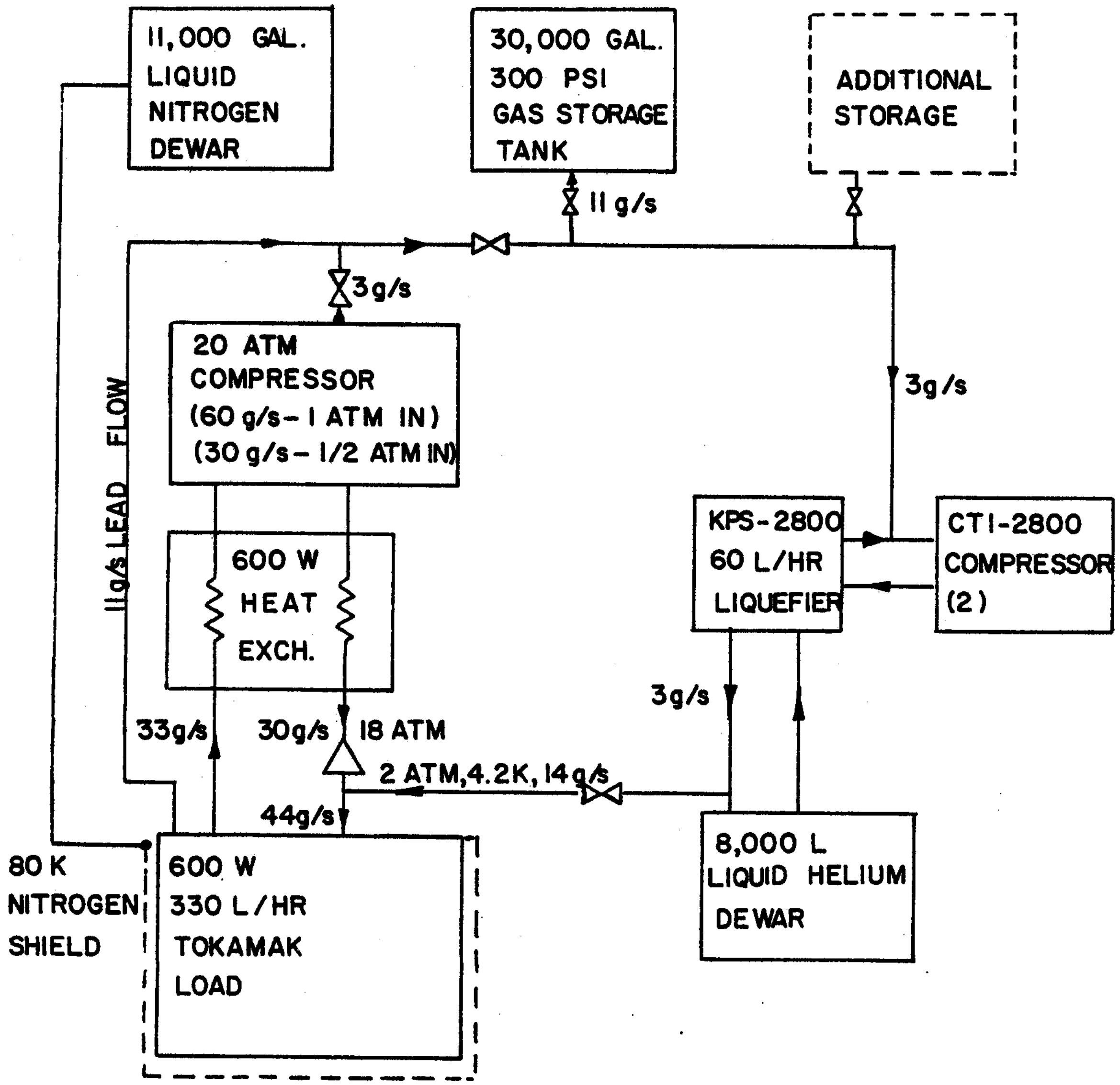

TABLE II.1.1

BLOCK DIAGRAM OF CRYOGENIC REFRIGERATION SYSTEM HELIUM FLOW DURING TOKAMAK OPERATION.

12.0 Vacuum System Requirements

The HESTER vacuum system must be capable of pumping down the vacuum chamber to an initial pressure of $1.3 \times 10^{-6} Pa$ (10^{-8} torr) in 25,000 s, and to be able to hold this vacuum against outgassing from a system with an internal surface area of 100 m^2. The vacuum pumping system must also be adequate to pump back down to the initial conditions in 100 s after a plasma discharge, and to be adequate for limiter pump and ash removal experiments. However, since there is no natural ash generation during the pure hydrogen pulses planned for HESTER , the most limiting case is steady-state removal of outgassed oxygen and water vapor and inleakage of air through the double sealed, butyl rubber seals in the vacuum vessel. System specifications are summarized in Table 12.1-I.

The conservative assumption used in the design against outgassing was that only 60 % of the internal surface should be considered to be bakeable, with the rest unbaked. This gives a total outgassing rate of 10^{-5} Pa-m^3/s, corresponding to a speed of 15.3 m^3/s. The butyl rubber seals are differentially pumped at 10^{-3} Pa, the same pressure as the Leybold-Heraus DK-200 rotary piston pumps, used to rough the main turbomolecular pumps. The air inleakage rate with 40 % compression of the butyl rubber seals is 5.9×10^{-6} Pa-m^3/s, giving a total system pumping speed requirement of 16 (m^3/s). Overall vacuum system requirements for pumpdown are summarized in Table 12.1.-II.

The high system pumping speed and the availability of a 4,000 l helium dewar, described in section 11, suggests that cryopanels, attached to the main system cryogenic system, may be the most economical method of pumping. This option has not yet been costed. The option of using 2500 l/s turbomolecular pumps can be sized and costed, using only catalog items. Using 7 vacuum ports, with 16 inch VAT 104-24pu gate valves, an elbow and TMP-3500 turbomolecular pumps, an undiscounted vacuum system would cost $392,000.

Table 12.1-I

PERFORMANCE SPECIFICATIONS - MAIN VACUUM SYSTEM

p_{base}	steady-state baseline pressure capability of the vacuum system	0.7 μPa
p_{init}	desired ambient pressure before initiation	1.3 μPa
p_{Of}	assumed oxygen pressure in the vacuum chamber at the end of a discharge	7 μ Pa
p_{Oi}	initial pressure of oxygen in the plasma before initiation	0.7 μ Pa
t_{down}	desired down time between plasma pulses	100 s
t_{pd}	desired pumpdown time of the system from stp to initial conditions	25,000 s
N_{seals}	number of mechanical vacuum seals in the system	4
$p_{intermed}$	intermediate pressure in a double sealed system	1 kPa
f_{baked}	fraction of the internal vacuum chamber that is baked out	0.6

Table 12.1-II

VACUUM SYSTEM FOR PUMPDOWN FROM STP AND BETWEEN PULSES

R_{nobake}	specific outgassing rate of stainless steel, no bakeout	0.132 μPa-m/s
R_{bake}	specific outgassing rate of steel after bakeout	2.64 nPa-m/s
R_{outgas}	total outgassing rate of the wall	9.89 μPa-m^3/s
p_{base}	steady-state base line pressure of the vacuum vessel	0.7 μPa
R_{leak}	leak rate through butyl rubber at 40 % squeeze	61.5 μPa-m^3/s
R_{2leak}	leak rate through the second seal	0.615 μPa-m^3/s
S_{stpi}	speed needed to pump down from STP to initial operating conditions	16.7 m^3/s
S_{o2fi}	oxygen pumping speed needed to remove oxygen between pulses	0.384 m^3/s
S_{outgas}	system pumping speed needed to maintain base pressure against outgassing	14.1 m^3/s
S_{leaks}	system pumping speed needed to maintain base pressure against leaks	0.879 (m^3/s)
S_{ss}	total system pumping speed needed to maintain base pressure	15 m^3/s
$S_{vacsystem}$	total system vacuum pumping speed	16 m^3/s

Table 12.1-III

COST AND POWER REQUIREMENTS OF VACUUM SYSTEM

S_{valve}	speed of a VAT 104-24pu 16 inch gate valve	30 m^3/s
S_{turbo}	speed of a Leybold-Heraeus TMP-3500 turbomolecular pump	3.5 m^3/s
S_{port}	speed of a vacuum vessel port for air	18.2 m^3/s
S_{elbow}	speed of the elbow for air	24.1 m^3/s
S_{pump}	effective pumping speed of a single pump	2.41 m^3/s
N_{turbo}	number of Leybold-Heraeus TMP-3500 turbomolecular pumps required	7
C_{turbo}	cost of turbomolecular pumps	229 k$
P_{turbo}	power required by turbomolecular pumps	6.02 kW
C_{valves}	cost of VAT 104-24pu 16 inch gate valves	70 k$
C_{tees}	cost of port to 16 inch tees	35 k$
C_{rough}	cost of Leybold-Hereaus DK-200 rotary piston roughing pumps	52.5 k$
C_{misc}	cost of miscellaneous vacuum hardware	6.07 k$
$C_{turbosyst}$	total cost of a vacuum system, based on turbopumps	392 k$

13.0 System Summary

All the parameters of the HESTER system are listed in an output listing of of the TOKSYC tokamak system code. While there is not total agreement between the outputs of the system code and the parameters in the design drawings and independent costing, neither are there any significant discrepancies.

The system description includes a listing of the installed capacity at the M.I.T. Plasma Fusion Center and the Francis Bitter National Magnet Laboratory. The available resources and the limitations of this site were a large determining factor in the formulation of this particular design solution to the problem of creating a new, low cost machine to address important needs of the tokamak program. The resources that were fully taken advantage of included the 9 MW long-pulse VHF supplies, the 4.0 MW long-pulse C-band power supplies, 30 km of 8,000 A superconductor, 1 or 2 CTI-2800 helium refrigerators along with the CDIF cryogenic storage facilities, an empty garage in an existing building with adequate space for auxiliary equipment, a 200 MJ pulsed motor-generator set, and 250 MW of solid-state rectifier power supplies. This equipment, if purchased new, is estimated to have added about $40 M to the cost of HESTER .

The principal limitation of the M.I.T. Plasma Fusion Center site is the relatively small amount of prime power available for a major fusion experiment. The installed capacity of the M.I.T. Plasma Fusion Center and the Francis Bitter National Magnet Laboratory, used in the Alcator C and Tara experimental programs, is listed in Table 13-1. The available steady-state and pulsed power for a new experiment are somewhat speculative, based on recent discussions with Cambridge Electric and M.I.T. Physical Plant. The availability of 10 MW steady-state appears to be relatively firm, while the availability of 20 MW pulsed for 10 s remains to be negotiated. 25 MW for 10 s has been rejected by the utility as physically damaging to the cable. The availability of 20 MW pulsed power would mean 20 MW on top of the steady-state draw, probably about 2 MW for cryogenic refrigeration, poloidal field coil supplies and motor-generator recharging. Thus, only 21-22 MW peak would be available from the utility, not 30 MW.

The Alcator C and Tara experiments, along with the National Magnet Laboratory, draw power from a single cable. The present negotiated permissible power for Alcator C is the combination of 18 MVA for a 1 second triangular ramp every 5 minutes, an 0.5 second 5 MVA square pulse every 5 minutes and 2 MVA for one hour to accelerate the generator. The cable also provides 10 MW of continuous power to the National Magnet Laboratory and 18 MVA for a 1 second flat-top and 2-4 MVA ramps to TARA with a duty cycle of

0.03 %. The current motor-generator set can deliver 200 MJ to a transformer. Thus, the use of Bitter plate toroidal field magnets with a recirculating power of 15 MW for comparable performance (and significantly higher operating costs due to high liquid nitrogen usage) would probably either use up all the available pulsed power over a 10 second pulse or all of the steady-state power from the cable. Overspeeding of the generator 1.1 pu has been discussed and would increase the available pulsed power by 50 %. Other alternatives include purchase of a low cost diesel generator or purchase of a new dedicated cable.

While the power and energy limitations at M.I.T. preclude a new experiment with copper magnets, they also reinforce previous perceptions of the importance of reducing recirculating power in any real life experiment with power and operating expense limitations. Whatever the power limitations, a 15 MW magnet system will reduce the possible auxiliary power, referred to the line, in any specific discharge scenario, by 15 MW and increase operating costs by several million dollars per year. The superconducting magnet system of HESTER solves the same problem for its experimental program that superconducting magnets are supposed to solve for commercial tokamak reactors.

A summary of machine parameters is given in Tables 13-2 through 13-23, with a certain amount of redundancy from previous chapters.

Table 13-1

NML INSTALLED CAPACITY

P_{line}	steady-state power from the utility	10 MW
P_{pulsed}	available pulsed power, 10 s	20 MW
P_{rect}	rectified 750 V power	187.5 MW
P_{ohrect}	rectified 1200 V power	60 MW
P_{efrect}	rectified 3000 V power	15 MW
W_{mgf}	available rotational stored energy	200 MW
P_{hvdc}	high voltage, regulated power supply capacity	3.52 MW
P_{vhfcw}	available cw vhf power	400 kW
$LCDIF$	available length of superconductor from CDIF	30.5 km

Table 13-2

MAJOR MACHINE DIMENSIONS

R_{oohm}	plasma major radius on axis during ohmic discharges	2.091 m
$a_{minorohm}$	plasma minor radius during ohmic discharges	312.3 mm
$a_{minorheat}$	plasma minor radius during auxiliary heating	240.9 mm
$a_{minorIdrive}$	plasma minor radius during current drive	240.9 mm
B_{tohm}	toroidal flux density on axis during ohmic discharges	6.695 T
W_{msyst}	stored magnetic energy in the reactor system	695.6 MJ

Table 13-3

SYSTEM POWER INVENTORY

P_{ss}	peak electrical power requirement of the system	42.67 MW
E_{pulse}	total energy required per pulse	402.2 MW
E_{avail}	available energy from the utility line and GE generator, during a pulse	180.0 MJ
$E_{storenew}$	new deliverable energy storage required, if pulsed	222.2 MJ
$I_{2Rmaxtf}$	maximum joule heating in the TF magnet supplies	75 kW
I_{2Ref}	maximum joule heating in the EF magnet supplies	300 kW
$P_{lineref}$	line power required by the cryogenic refrigerator	565.1 kW
$P_{lineaux}$	line power required for auxiliary heating	18.21 MW
$P_{lineIdrive}$	line power required for current drive	23.89 MW
P_{ss}	total steady state line power requirement	42.67 MW

Table 13-4

OVERALL MACHINE SPECIFICATIONS

R_{mintf}	smallest major radius of the TF magnet, including its warm case,	1.385 m
t_{shield}	neutron and gamma shield thickness	0.0 m
RB	major radius - flux density product in the TF magnet bore	14 m-T
R_{iooh}	ratio of the inner to the outer radius of the central solenoid	0.700
f_{vvohm}	fraction of the vacuum vessel used by the plasma for ohmic discharges	0.709
f_{vvheat}	fraction of the vacuum vessel used by the plasma for auxiliary heating	0.570
$f_{vvIdrive}$	fraction of the vacuum vessel used by the plasma for current drive	0.570
$f_{maxplasvport}$	fraction of the largest plasma observed by a vertical port	0.700
t_{rise}	plasma current rise time	1.500 s
$t_{shutdown}$	plasma current shutdown time	30 s
$t_{flatohm}$	maximum flattop of an ohmic discharge	8.500 s
t_{cycle}	minimum discharge/recharge time of the system	600.0 s
n_{ports}	number of ports in the tokamak	18
L_{wg}	total length of a waveguide run from tube to tokamak	30 m
n_{year}	maximum number of plasma discharges per year	4000.
n_{week}	maximum number of plasma discharges per week	200.0
n_{day}	maximum number of plasma discharges per day	50
$burnyears$	number of D-T burn years	0.0
P_w	maximum neutron wall loading or 4 times thermal	20 MW/m^2

Table 13-5

OHMIC FLUX AND VOLTAGE REQUIREMENTS

R_o	plasma major radius	2.091 m
a_{minor}	plasma minor radius	312.3 mm
V_r	flattop resistive voltage	1.835 V
ψ_p	plasma inductive volt-second requirements	8.474 V-s
t_{flat}	flattop time	8.500 s
V_i	loop voltage required for initiation	105.1 V
Φ_{rsu}	resistive volt-seconds during start-up	3.390 V-s
Φ_{rflat}	resistive volt-seconds during flat-top	15.60 V-s
Φ_r	total resistive volt-second requirement of the plasma	18.99 V-s
Φ_{tsu}	total volt-second requirement of ohmic start-up	11.86 V-s
Φ_{total}	total volt-second requirement of the plasma	27.46 V-s

Table 13-6

CURRENTS AND POSITIONS OF THE OH COILS

i	OH coil number	1
R_{1oh}	inner major radius	955 mm
R_{2oh}	outer major radius	1.240 m
Z_{1oh}	lower height	595.0 mm
Z_{2oh}	upper height	991.6 mm
I_{oh}	ampere-turns in the i-th OH coil	1.47 MAT
i	OH coil number	2
R_{1oh}	inner major radius	955 mm
R_{2oh}	outer major radius	1.240 m
Z_{1oh}	lower height	198.3 mm
Z_{2oh}	upper height	595.0 mm
I_{oh}	ampere-turns in the i-th OH coil	1.47 MAT
i	OH coil number	3
R_{1oh}	inner major radius	955 mm
R_{2oh}	outer major radius	1.240 m
Z_{1oh}	lower height	-198.3 mm
Z_{2oh}	upper height	198.3 mm
I_{oh}	ampere-turns in the i-th OH coil	1.47 MAT
i	OH coil number	4
R_{1oh}	inner major radius	955 mm
R_{2oh}	outer major radius	1.240 m
Z_{1oh}	lower height	-595.0 mm
Z_{2oh}	upper height	-198.3 mm
I_{oh}	ampere-turns in the i-th OH coil	1.47 MAT
i	OH coil number	5
R_{1oh}	inner major radius	955 mm
R_{2oh}	outer major radius	1.240 m
Z_{1oh}	lower height	-991.6 mm
Z_{2oh}	upper height	-595.0 mm
I_{oh}	ampere-turns in the i-th OH coil	1.47 MAT
λ_{joh}	overall current-density in the i-th OH coil	13 MA/m^2

Table 13-6 - continued

CURRENTS AND POSITIONS OF THE OH COILS - CONTINUED

i	OH coil number	6
R_{1oh}	inner major radius	1.527 m
R_{2oh}	outer major radius	1.738 m
Z_{1oh}	lower height	839.2 mm
Z_{2oh}	upper height	1.051 m
I_{oh}	ampere-turns in the i-th OH coil	1.341 MA-T
i	OH coil number	7
R_{1oh}	inner major radius	1.527 m
R_{2oh}	outer major radius	1.738 m
Z_{1oh}	lower height	-1.051 m
Z_{2oh}	upper height	-839.2 mm
I_{oh}	ampere-turns in the i-th OH coil	1.341 MA-T
i	OH coil number	8
R_{1oh}	inner major radius	2.852 m
R_{2oh}	outer major radius	2.979 m
Z_{1oh}	lower height	773.8 mm
Z_{2oh}	upper height	900.5 mm
I_{oh}	ampere-turns in the i-th OH coil	482.1 kA-T
i	OH coil number	9
R_{1oh}	inner major radius	2.852 m
R_{2oh}	outer major radius	2.979 m
Z_{1oh}	lower height	-900.5 mm
Z_{2oh}	upper height	-773.8 mm
I_{oh}	ampere-turns in the i-th OH coil	482.1 kA-T
$NI_{ohtotal}$	number of ampere-turns in the OH system	7.364 MA-T
$NI_{mohtotal}$	number of ampere-meters in the OH system	46.27 MA-m

Table 13-7

CURRENTS AND POSITIONS OF EF COILS

R_{ef1}	major radius of the first EF coil	2.915 m
Z_{ef1}	height of the first EF coil	715.0 mm
I_{ef11}	total number of ampere-turns in the first EF coil on discharge 1	-354.7 kA-T
I_{ef12}	total number of ampere-turns in the first EF coil on discharge 2	-413.7 kA-T

R_{ef2}	major radius of the second EF coil	1.495 m
Z_{ef2}	height of the second EF coil	700.0 mm
I_{ef21}	total number of ampere-turns in the first EF coil on discharge 1,	630.0 kA-T
I_{ef22}	total number of ampere-turns in the second EF coil on discharge 2,	731.0 kA-T

R_{o1}	plasma major radius for discharge 1	2.033 m
R_{o2}	plasma major radius for discharge 2	2.082 m
I_{p1}	plasma current for discharge 1	817.0 kA
I_{p2}	plasma current for discharge 2	1.190 MA

ϕ_{11}	flux linkage between EF1 and the first plasma	-1.023 V-s
ϕ_{12}	flux linkage between EF1 and the second plasma	-1.257 V-s
ϕ_{ef21}	flux linkage between the second EF coil and the first plasma discharge	1.208 V-s
ϕ_{ef22}	flux linkage between the second EF coil and the second plasma discharge	1.388 V-s
ϕ_{ef}	EF system contribution to the plasma inductive volt-seconds for an ohmic discharge	368.3 mV-s
ϕ_{efbeta}	EF system contribution to the plasma inductive volt-seconds for a high beta discharge	262.2 mV-s

NI_{mef}	number of ampere-meters in the EF system	28.89 MA-m
NI_{ef}	total number of ampere-turns in the EF system	2.289 MA-T

Table 13-8

DESIGN SPECIFICATIONS: SUPERCONDUCTING TF MAGNET SYSTEM

NI_{tf}	number of ampere-turns in the toroidal field system	70 MA-T
N_{tf}	number of toroidal field coils	36
NI_{magnet}	number of ampere-turns in one toroidal field magnet	1.944 MA-T
$sctype$	superconductor material	Nb_3Sn ()
$condtype$	type of superconductor	Airco LCP
V_{max}	maximum design value of final voltage on quench	3.20 kV
T_b	helium bath temperature	4.200 K
T_f	maximum final temperature in the conductor on quench	200.0 K
p_{hein}	magnet inlet pressure of the helium coolant	240.0 kPa
α	ratio of operating to critical current	0.7
f_{He}	helium or void fraction of a conductor envelope or cable space	0.400
$R_{inboretf}$	inside bore radius of a toroidal field magnet winding pack	520.0 mm
RB	desired major radius - flux density product in the TF bore	14 m-T
$w_{intherm}$	width of cold to warm thermal isolation, inside case wall	20 mm
$w_{outtherm}$	width of cold to warm thermal isolation, outside case wall	20 mm
$w_{intherm}$	width of cold to warm thermal isolation, inside case wall	0.0 m
$t_{minwedge}$	minimum intercase wedge thickness	11.67 mm

Table 13-9

INTERNALLY COOLED CABLED SUPERCONDUCTOR SPECIFICATIONS

$sctype$	superconductor type	Nb_3Sn ()
f_{He}	helium fraction of the inside cross-section	0.400
$Cu - noncu$	copper/noncopper ratio of a superconducting composite strand	1.700
$A_{noncucond}$	noncopper area of the cable	67.33 mm^2
A_{sccond}	cross-section area of superconductor in a cable	15.49 mm^2
A_{in}	inside cross-section, available for helium and conductor	282.7 mm^2
t_{jack}	jacket thickness	1.730 mm
w_{ojack}	outside jacket width	20.80 mm
D_o	strand diameter	700.0 μm
D_{br}	bronze diameter	420.0 μm
L_{pf}	filament twist pitch length	25.40 mm
L_{pcable}	cable twist pitch length	305.0 mm
n_{fil}	number of filaments in a strand	2869
N_{stran}	number of strands	486
P_w	wetted perimeter of the cable and conduit	1.137 m
ρ_{jak}	jacket resistivity	500.0 n$\Omega - m$
ρ_{noncu}	resistivity of the noncopper/nonsuperconductor	50 nΩ-m
R_{stran}	radius of a strand	350.0 μm
RRR	residual resistivity ratio of the matrix	75

Table 13-10

MASS AND VOLUME INVENTORY: TF MAGNET SYSTEM

L_{cond}	total length of conductor	13.22 km
V_{sccoil}	volume of superconductor in a coil	0.01856 m^3
V_{sscoil}	volume of steel in a coil	0.1037 m^3
V_{cucoil}	volume of copper in a coil	0.1247 m^3
$V_{inscoil}$	volume insulation in a coil	0.02256 m^3
V_{sctf}	volume of superconductor in the TF system	0.6683 m^3
V_{sstf}	volume of stainless steel in the TF system	3.733 m^3
V_{cutf}	volume of copper in the TF system	4.489 m^3
V_{instf}	volume of insulation in the TF system	0.8123 m^3
M_{cutf}	mass of copper in the TF system	40.04 tonne
M_{sstf}	mass of stainless steel in the TF system	29.11 tonne
M_{nbtf}	mass of niobium in the TF system	3.743 tonne
M_{instf}	mass of insulation in the TF system	1.097 tonne
M_{cold}	cold mass of the TF system	73.99 tonne
M_{vv}	mass of the vacuum vessel	16.54 tonne

Table 13-11

DIMENSIONS OF THE SUPERCONDUCTING TF MAGNET SYSTEM

R_{mintf}	minimum major radius of the TF magnet, including warm case	1.385 m
B_{maxtf}	maximum flux density at the toroidal field coils	9.021 T
$w_{indbuild}$	radial build of the conductor winding pack	245.1 mm
$w_{intherm}$	total width of cold to warm thermal isolation, inside leg	20 mm
$w_{outtherm}$	total width of cold to warm thermal isolation, outside case wall	20 mm
t_{incase}	thickness of the inner case winding bobbin	14.55 mm
$t_{outcase}$	thickness of the outer case closure ring	29.10 mm
$t_{sidecase}$	thickness of the case side walls	29.10 mm
w_{wind}	width of the winding pack	184.1 mm
$t_{weldgap}$	weld gap between the winding pack and the outer closure ring	0.0 m
$r_{wpboreav}$	average bore radius of the winding pack	664.4 mm
$r_{inwpboretf}$	inner clear bore of the winding pack	520.0 mm
$r_{inmagnet}$	inner clear bore of the magnet can or dewar	500.0 mm
$r_{outcasebore}$	outer bore of the structural case	808.7 mm
δr_{casein}	inside radial build of the structural case	245.1 mm
δR_{case}	radial build of the structural case	288.7 mm
$R_{tfmagbore}$	major radius of the axis of the TF magnet bore	2.199 m
R_{minwp}	smallest major radius of the conductor winding pack	1.434 m
R_{bmaxtf}	maximum field radius of the magnet	1.679 m
R_{1dewar}	major radius of the high field side of the can or dewar	1.714 m
R_{2dewar}	major radius of inside of outer leg of can or dewar	2.714 m

Table 13-12

DIMENSIONS OF THE SUPERCONDUCTING TF MAGNET SYSTEM (continued)

A_{sc}	area of superconductor required in a coil	0.0044 m^2
A_{cu}	area of copper required in a coil	0.02987 m^2
A_{ins}	area of insulation required in a coil	0.0054 m^2
A_{case}	area of the structural case	0.02484 m^2
A_{coil}	total area of the winding pack and structural case	0.070 m^2
A_{heins}	area of helium and insulation required in a coil	0.0108 m^2
A_{wp}	total area of the winding pack, including ground insulation	0.0451 m^2
J_c	noncopper critical current density	56.02 kA/cm^2
A_{cucond}	copper area of a conductor	1.197 cm^2
$A_{noncucon}$	noncoppper area of a conductor	0.673 cm^2
t_{gaptf}	clearance gap between TF coils at the equator	231.6 mm
D_{port}	maximum inside diameter of port between the TF coils at the equator	180 mm
V_{vac}	volume evacuated by the main vacuum pumps	17.46 m^3
A_{outgas}	area of steel outgassing into the plasma	191.5 m^2
I_{cond}	conductor current	22.28 kA
$n_{dpancakes}$	number of double pancakes in a winding	40
n_{layers}	number of layers in a pancake	11
n_{turns}	number of turns in a winding	88
L_{scnew}	total length of new superconductor in the TF system	13.22 km
L_{sctf}	total length of superconductor in the TF system	13.22 km
NI_{mtf}	total number of ampere-meters in the TF system	294.6 MA-m

Table 13-13

CIRCULAR SUPERCONDUCTING TF MAGNET SYSTEM

N_{par}	actual number of parallel discharge circuits	20
N_{leads}	number of discharge leads	4
N_{series}	total number of series magnets, during discharge,	18
W_{mtf}	magnetic stored energy of the toroidal magnet system	369.0 MJ
F_z	total vertical force on the upper half of the magnet system	329.7 MN
F_r	total centering force on the toroidal magnet system	-177.8 MN
F_z	total vertical force on a magnet	9.159 MN
F_r	total radial force on a magnet	-4.940 MN

Table 13-14

ENERGY BALANCE TERMS: TF SUPERCONDUCTOR

$sctype$	superconductor material type	Nb_3Sn ()
A_{noncu}	superconductor noncopper area	67.3 mm^2
A_{cu}	copper area of the conductor	119.7 mm^2
B_t	magnetic flux density	9.021 T
T_b	bath temperature	4.200 K
T_{cN_3Sn}	zero-current critical temperature of Nb_3Sn	10.01 K
T_{cNb_3Sn}	current sharing temperature in Nb_3Sn	5.943 K
ρ_{cu}	resistivity of copper at the specified field	933.7 pOhm-m
P_{lTc}	power dissipation per unit length at the critical temperature	115.7 kW/m
Q_{pp}	heat flux per unit area into the helium on quench	101.8 kW/m^2
k_{cuBT}	thermal conductivity of copper at design temperature and field	110.2 W/m-K
R_g	radius of the minimum propagating zone	8.509 mm
$v_{adiabatic}$	adiabiatic longitudinal propagating velocity of a quench	10.89 m/s
v_{qlong}	longitudinal propagation velocity of a quench, with cooling,	4.700 m/s
q	total heat transferred by nucleate boiling during film establishment	8.640 J/m
t_{adiacs}	metal enthalpy to current sharing divided by power/length	2.965 μs
t_{adiac}	metal enthalpy to critical temperature divided by power/length	26.59 μs
t_{isocs}	bath enthalpy to current sharing divided by the power per length	2.500 ms
t_{heatTf}	characteristic time to heat the copper to final temperature	3.035 s

Table 13-15

SUPERCONDUCTOR ENTHALPY MARGINS: TF MAGNETS

ΔH_{cubcsl}	bath to current sharing copper energy/length	288.3 mJ/m
ΔH_{nonbcs}	bath to current sharing change in enthalpy in noncopper	631.8 mJ/kg
$\Delta H_{nonbcsl}$	bath to current sharing energy/length absorbed by noncopper	54.80 mJ/m
$\Delta H_{metalbcsl}$	total bath to current sharing energy/length absorbed by metal	343.1 mJ/m
ΔH_{hebcsl}	bath to current sharing change in enthalpy/length in helium	76.03 J/m
ΔH_{bcsl}	enthalpy/length to raise entire conductor to current sharing temperature	76.37 J/m
$\Delta H_{metalbcsv}$	total bath to current sharing energy/volume of metal absorbed by metal	2.538 mJ/cm^3
ΔH_{bcsv}	total bath to current sharing energy/volume of metal	564.9 mJ/cm^3
ΔH_{cu}	change in copper enthalpy between bath and critical temperature	2.266 J/kg
ΔH_{cul}	enthalpy/length to raise the copper to the critical temperature	2.414 J/m
ΔH_{nonbc}	bath to critical change in enthalpy in the noncopper	7.650 J/kg
ΔH_{nonbcl}	bath to critical energy/length absorbed by the noncopper	663.4 mJ/m
ΔH_{hebc}	bath to critical change in enthalpy in the helium	35.14 kJ/kg
ΔH_{hebcl}	bath to critical change in enthalpy/length in the helium	286.3 J/m
ΔH_{bcl}	enthalpy/length to raise the entire conductor to the critical temperature	289.4 J/m
$\Delta H_{metalbcv}$	total bath to current sharing energy/volume of metal absorbed by metal	22.77 mJ/cm^3
ΔH_{bcv}	total bath to current sharing energy/volume of metal	2.141 J/cm^3
ΔH_{10bo}	10 % helium boil off energy/volume of metal	120.5 mJ/cm^3

Table 13-16

OUTER VACUUM CAN DIMENSIONS

R_{mintf}	minimum major radius of the toroidal magnet system	1.385 m
t_{vv}	thickness of the outer vacuum can wall	30 mm
ΔR_{vaccan}	total radial build of the outer vacuum can at the inside	125.0 mm
R_{mincan}	minimum major radius of the outer vacuum can	1.260 m

Table 13-17

INNER VACUUM VESSEL DIMENSIONS

f_{thick}	fraction of the vacuum vessel that is thick walled	0.700
$f_{bellows}$	fraction of the vacuum vessel that is thin walled bellows	0.300
R_{in1vv}	inner [greater] major radius of the vacuum vessel inside leg	1.739 m
R_{in2vv}	inner [lesser] major radius of the vacuum vessel outside leg	2.660 m
r_{invv}	inside minor radius of the vacuum vessel	460.5 mm
L_{vv}	inductance of the inner vacuum vessel	4.541 μH
R_{vv}	resistance of the inner vacuum vessel	42.16 mΩ
$t_{disrupt}$	fall time outside the vacuum vessel, due to an internal disruption	107.7 μs
M_{vv}	mass of the inner vacuum vessel	1,260 kg

Table 13-18

SIZE OF VACUUM VESSEL INTERNAL COMPONENTS

R_{1invv}	inner (greater) major radius of inside leg of inner vacuum vessel	1.739 m
r_{invv}	inside minor radius of the vacuum vessel	460.5 mm
R_{2invv}	inner (lesser) major radius of the outside leg of the inner vacuum vessel	2.660 m
t_{rails}	thickness of the rails	20 mm
$t_{inlimiter}$	thickness of the limiters on the inside	0.0 m
$t_{outlimiter}$	thickness of the limiters on the outside	60 mm
$t_{inantenna}$	thickness of the antenna on the inside	40 mm
$t_{outantenna}$	thickness of the antenna on the outside	40 mm
$R_{inplasma}$	innermost possible major radius of the plasma edge	1.779 m
$R_{outplasma}$	outermost possible major radius of the plasma edge	2.600 m
$r_{maxplas}$	maximum physically possible plasma minor radius	410.5 mm

Table 13-19

DIMENSIONS OF PLASMA DISCHARGES

$a_{minorohm}$	plasma minor radius for ohmic discharges	312.3 mm
R_{oohm}	plasma major radius for ohmic discharges	2.091 m
$a_{minorheat}$	plasma minor radius for auxiliary heating discharges	240.9 mm
R_{oheat}	plasma major radius for auxiliary heating discharges	2.020 m
$a_{minorIdrive}$	plasma minor radius for current drive discharges	240.9 mm
$R_{oIdrive}$	plasma major radius for current drive discharges	2.020 m
B_{tohm}	flux density on axis for ohmic discharges	6.695 m
B_{theat}	flux density on axis for auxiliary heating discharges	6.932 m
$B_{tIdrive}$	flux density on axis for current drive discharges	6.932 T

Table 13-20

SIZING OF VERTICAL DIAGNOSTIC PORTS

R_o	plasma major radius used for port location	2.091 m
a_{minor}	plasma minor radius used for port location	312.3 mm
f_{vport}	fraction of the plasma minor diameter viewed by the port	0.700
R_{1vport}	inner major radius of the vertical port	1.935 m
R_{2vport}	outer major radius of the vertical port	2.403 m

Table 13-21

HORIZONTAL PORT SIZE

n_{ports}	number of ports	18 ()
H_{port}	height above the equator of the port	369.2 mm
w_{port}	width at the equator of the port	180 mm
A_{port}	maximum port area	0.133 m^2

Table 13-22

LOWER HYBRID CURRENT DRIVE MICROWAVE POWER DELIVERY SYSTEM

n_{ports}	number of heating ports	3
n_{grill}	number of wave guides in a grid	16
n_{port}	number of wave guides in a port	96
n_{stack}	number of stacked grids in a port	6
n_{wg}	total number of wave guides in the heating system	288
L_{wg}	total length of a waveguide run	30 m
L_{vmax}	maximum port space in the vertical direction	361.4 mm
t_{vcool}	thickness of the vertical coolant passage between guides	800.0 μm
h_{wg}	height of the wave guide, long dimension	57.50 mm
w_{wg}	width of the wave guide, short dimension	80 mm
t_{septum}	thickness of the interwaveguide septum	20 mm
t_{hcool}	thickness of the horizontal coolant passage between grills	11.50 mm
A_{port}	area required by one port	0.18 m^2
a_{wg}	area of the wave guide	460.0 mm^2
ω	rf frequency of the launched wave	28.90 Gradians/s
f	rf frequency of the launched wave	4.600 GHz
η_{launch}	efficiency of heat deposition from the grid into the plasma	0.800
η_{reg}	efficiency of a high-voltage series regulator	0.800
η_{kly}	efficiency of a klystron	0.500
s_{fwgcut}	safety factor of the wave guide dimensions vs. cutoff	1.100
E_{rfmax}	maximum permissible rf electric field	220.0 kV/m

Table 13-23 POWER INVENTORY LH DELIVERY SYSTEM

P_{load}	power delivered to the load	5 MW
P_{tube}	rf power needed to feed one waveguide	31 kW
P_{tubes}	output rf power required from the tubes	13.89 MW
P_{line}	power drawn from the line by the rf system	23.89 MW
P_{bd}	maximum possible power transmission through a waveguide	12.16 kW
P_{anode}	dc anode power required by the microwave tube	19.29 MW
P_{rect}	unregulated power supplied by a high-voltage rectifier	22.70 MW
P_{dmax}	maximum permitted power density in the grid	25 MW/m^2
N_{pwg}	total attenuation of the TE01 mode in the waveguides	3.227 db
P_{dwg}	power dissipated in the waveguides	5.510 MW
$P_{wginport}$	power dissipated in the waveguides, inside the port	4.286 MW
P_{wwg}	wall loading on the waveguide, inside the port	146.1 kW/m^2
a_{circ}	attenuation in the circulator	230.0 mdb
a_{wind}	attenuation in the waveguide window	10 mdb
N_{ptot}	total attenuation of the rf system	4.437 db
a_{launch}	"attenuation" of launching into the plasma	970.7 mdb
a_{TE10cu}	attenuation of the TE01 mode in copper guide	107.6 mdb/m
λ_{cTE01}	cutoff wavelength for the TE01 mode	16 mm
λ_{cTE11}	cutoff wavelength for the TE11 mode	15.85 mm
λ_{cTE10}	cutoff wavelength for the TE10 mode	115.0 mm
λ	free-space wave length at the launching frequency	65.22 mm
λ_{wg}	waveguide wavelength of the T mode	79.19 mm
P_{wg}	maximum power transmitted through one waveguide	11.50 kW